

**Best  
Available  
Copy**

**REPORT DOCUMENTA**

Public reporting burden for this collection of information is estimated to average 1 hour per response, including the time for reviewing existing data sources, gathering and maintaining the data needed, and completing and reviewing the collection of information. Send comments regarding this burden estimate or any other aspect of this collection of information, including suggestions for reducing the burden to Washington Headquarters Service, Paperwork Project Director, Washington, DC 20503-2970, and the Office of Management and Budget, Paperwork Project Director (0304-0188), Washington, DC 20503-2970.

**AD-A275 023**

OMB No. 0704-0188

here, searching existing data sources, gathering and  
any other aspect of this collection of information,  
Jefferson Davis Highway, Suite 1204, Arlington,  
Virginia 22202-4302, and the Office of Management and Budget,

**1. AGENCY USE ONLY****2. REPORT DATE**

27-Sep-93

**3. REPORT TYPE AND DATES COVERED**

Final Technical Rpt

15-Jan-92 Thru 14-Jul-93

**4. TITLE AND SUBTITLE**

Spatial Light Modulators with Arbitrary Quantum Well Profiles

**5. FUNDING NUMBERS**

AFOSR-90-0118 DEF

**6. AUTHOR(S)**

Dr. George N. Maracas

Dr. Krishan K. Bajaj

AFOSR-TR-

94 0019

**7. PERFORMING ORGANIZATION NAME(S) AND ADDRESS(ES)**

Arizona State University  
Electrical Engineering Department  
Box: 875706  
Tempe, AZ 85287-5706

**8. PERFORMING ORGANIZATION  
REPORT NUMBER**

DWA 1764

**9. SPONSORING/MONITORING AGENCY NAME(S) AND ADDRESS(ES)**

AFOSR/NE  
Building 410  
Bolling AFB, DC 20332-6448

**DTIC**  
**ELECTE**  
**JAN 27 1994**  
**S A**

**10. SPONSORING/MONITORING  
AGENCY REPORT NUMBER**

348483

**11. SUPPLEMENTARY NOTES****12a. DISTRIBUTION/AVAILABILITY STATEMENT**

Approved for public release; distribution unlimited

**12b. DISTRIBUTION CODE****13. ABSTRACT (Maximum 200 words)**

This is the final technical report for University Research Initiative (URI) program "Spatial Light Modulators with Arbitrary Quantum Well Profiles." This program explored the use of quantum wells having arbitrary shapes for optical modulators and lasers. This comprehensive effort addressed MBE growth of compositionally graded wells and dielectric mirrors, accurate measurements of absorption coefficient in free-standing membranes, comparison of different active region optical properties, device fabrication and theory of excitons in the presence of applied electric and magnetic fields.

**94-02634****14. SUBJECT TERMS**

Spatial light Modulators with Arbitrary Quantum Well Profiles

**15. NUMBER OF PAGES**

68

**16. PRICE CODE**

**17. SECURITY CLASSIF-  
ICATION OF REPORT**  
Unclassified

**18. SECURITY CLASSIF-  
ICATION**  
Unclassified

**19. SECURITY CLASSIF-  
ICATION OF ABSTRACT**  
Unclassified

**20. LIMITATION OF ABSTRACT**  
UL

**94 1 26 070**

# Spatial Light Modulators with Arbitrary Quantum Well Profiles

University Research Initiative Program  
AFOSR-90-0118 DEF

George N. Maracas  
Arizona State University  
Electrical Engineering Department  
Tempe, AZ

Krishan K. Bajaj  
Emory University  
Physics Department  
Atlanta, GA

Accession For		
NTIS	CRA&I	<input checked="" type="checkbox"/>
DTIC	TAB	<input type="checkbox"/>
Unannounced		<input type="checkbox"/>
Justification		
By		
Distribution /		
Availability Codes		
Dist	Avail and/or Special	
A-1		

DTIC QUALITY INSPECTED 8

## **ABSTRACT**

This is final technical report for University Research Initiative (URI) program "Spatial Light Modulators with Arbitrary Quantum Well Profiles." This program explored the use of quantum wells having arbitrary shapes for optical modulators and lasers. This comprehensive effort addressed MBE growth of compositionally graded wells and dielectric mirrors, accurate measurements of absorption coefficient in free-standing membranes, comparison of different active region optical properties, device fabrication and theory of excitons in the presence of applied electric and magnetic fields.

A. Statement of work .....	1
A.1. Experiment .....	1
A.2. Theory .....	2
B. Status of the research effort: A substantive statement of significant accomplishments and progress toward achieving the research objectives.....	3
1. Experimental realization of nonrectangular quantum well modulators - ASU .....	3
1.1. Arbitrary shaped quantum wells.....	3
1.1.1. ATQW structural and optical property correlation .....	3
1.1.2. Technique for accurately measuring absorption coefficients of quantum wells .....	7
1.1.3. Comparison of absorption coefficients in ATQW and RQW ....	12
1.1.4. Coupled Double Quantum Wells (CDQW) .....	15
1.1.5. InGaAs/GaAs and InGaAs/AlGaAs ATQW.....	16
1.2. Distributed Bragg Reflectors (DBR).....	18
1.2.1. In situ Measurements of AlGaAs/GaAs Bragg Reflectors by Spectroscopic Ellipsometry.....	18
1.3. Spatial Light Modulators .....	21
1.3.1. Fabrication of Spatial Light Modulators.....	21
1.3.2. Spatial Light Modulator Performance .....	22
1.3.2.1. Coupled Quantum Well Fabry-Perot Modulator .....	22
1.3.2.2. High Contrast Ratio, Asymmetric FP Modulator.....	25
1.3.2.3. Novel Bistable MQW Electro-optic Phase Modulator. ....	28
1.4. Lasers .....	30
1.4.1. ATQW Vertical Cavity Surface Emitting Laser (VCSEL).....	30
1.4.2. InGaAs/GaAs/AlGaAs ATQW Lasers .....	31
1.5. References .....	34
2. Theoretical treatment of confined excitons in applied fields.....	38
2.1. A New Method For Calculating Excitonic Properties In Quantum-Confined Semiconductor Structures With Arbitrary Potential Profiles In The Presence Of Applied Fields .....	38
2.2. Effects Of Parallel Electric And Magnetic Fields On Confined Donor States In A Coupled Double Quantum Well .....	43
2.3. Confined Donor States In Cross Electric And Magnetic Fields In A Coupled Double Quantum Well .....	45
2.4. Effects Of Electric And Magnetic Fields On Confined Donor And Exciton States In A Dielectric Quantum Well.....	47
2.5. Hydrogenic Impurities In Quantum Wires In The Presence Of A Magnetic Field. ....	49
2.6. Exciton Binding Energies In A Quantum Wire In The Presence Of A Magnetic Field .....	50
2.7. Hydrogenic Donor States In Quantum Dots In The Presence Of A Magnetic Field .....	52
2.8. A Quantum Statistical Theory Of Excitonic Linewidth Due To Compositional Disorder In Semiconductor Alloys And Quantum Well Structures.....	55
2.9. Summary .....	61
2.10. References .....	61
C. Publications in technical journals. ....	62
D. Professional personnel associated with the research effort.....	63
E. Interactions: .....	63
E.1. Papers presented at meetings, conferences, seminars, etc. ....	64
E.2. Consultative and advisory functions to other laboratories and agencies.....	65
F. New discoveries, inventions, or patent disclosures and specific applications stemming from the research effort. ....	65
G. Other statements. ....	65

## A. Statement of work

The experimental work on this project is performed at Arizona State University under the supervision of Prof. G. N. Maracas. The theoretical effort is under the supervision of Prof. K. K. Bajaj at Emory University.

### **A.1. Experiment**

The accomplishments during the course of this three year research program are briefly described here. Details on many of these can be found in the following sections.

#### \* Developed and Implemented Poisson-Schrödinger Solver

A new approach to solving for energy levels and wave functions in a quantum well modulator active region has been developed and implemented. A spectral solution of Schrödinger's equation couples with a self-consistent solution of Poisson's equation has predicted the performance of optical modulators and vertical cavity surface emitting lasers.

#### \* Correlated TEM micrograph with PL data from ATOW

Transmission electron microscopy (TEM) has been used to determine the potential profile in asymmetric triangular quantum wells (ATQW). The experimentally determined profiles are used as input into the Schrödinger solver. Calculated bound energy levels corresponded to within 1 meV of the bound energy levels measured by optical techniques (both  $n=1$  and  $n=2$  light hole and heavy hole).

#### \* Realization of highest quality GaAs/AlGaAs and InGaAs/GaAs ATOWs

Photoluminescence linewidth was used as an optimization parameter in growing high quality ATQWs. A GaAs/AlGaAs ATQW has exhibited a record narrow line width (2.1 meV) at 2K. The linewidth for a single 50Å  $\text{In}_{0.13}\text{Ga}_{0.87}\text{As}/\text{GaAs}$  QW was measured to be 0.7 meV. These are both record narrow linewidths. A narrow linewidth is required for a high on/off ratio of a quantum confined Stark effect (QCSE) modulator. Experimental results show excellent agreement with theoretical predictions.

#### \* Analyzed a variety of quantum well active area designs

The growth and characterization of the active region for quantum well modulators has been studied. Asymmetric coupled double quantum wells (ACDQW), symmetric coupled double quantum wells (SCDQW), ATQW, and rectangular quantum wells (RQW) have been explored for use in high on/off ratio optical modulators. Experimental results from these optical structures agree well with theoretical results.

#### \* Reported first InGaAs/GaAs ATOW PL

The first coherently strained InGaAs/GaAs ATQWs have been realized. These quantum wells exhibited higher luminescence (factor of five greater) than the equivalent energy rectangular quantum well. Record narrow 2K PL linewidths of 0.6 meV were obtained under optimized growth conditions.

#### \* Measured first *in situ* AlGaAs/GaAs Bragg reflectors by spectroscopic ellipsometry

*In situ* spectroscopic ellipsometry has been successfully used to determine the normal incident reflectance of a Bragg reflector. The ability to control the growth of such complicated structures will allow them to be grown reproducibly.

#### \* Record low InGaAs/GaAs VCSEL threshold current density

The fabrication of vertical cavity surface emitting lasers (VCSELs) has been refined and improved. An InGaAs/GaAs VCSEL with record threshold current densities as low as 487 A/cm<sup>2</sup> has been realized.

#### \* First realization of a novel bistable MOW electro-optic phase modulator

The electrical bistability of a SEED was integrated with a phase modulator to produce optical bistability in an all-optical switch. A control wavelength of  $\sim 850\text{nm}$  incident on the spatial light modulator thus is used to switch light at  $\lambda \sim 1.1\mu\text{m}$  which is propagating in a direction perpendicular to the control signal.

\* Record high ON/OFF ratio of a MOW spatial light modulator

A major goal of this project was to realize spatial light modulators (SLMs) that are optimized for ON/OFF ratio. We have succeeded in obtaining world record ON/OFF ratios of over 1000 which is a factor of three higher than previously reported results.

\* Compared absorption coefficients in free-standing quantum wells having several different shapes.

A sensitive and accurate reflectance/absorption measurement system has been constructed which can measure to one part in  $10^4$ . This has been used to measure absolute absorption coefficients versus wavelength for multiple quantum wells having rectangular, triangular and parabolic composition gradients.

\* Realization of the first asymmetric triangular quantum well (ATQW) laser

Strained InGaAs/GaAs/AlGaAs edge-emitting ATQW lasers were constructed and characterized as a function of well width. Performance of these lasers was compared with lasers having rectangular quantum wells (RQW). It was observed that these lasers had threshold currents equivalent to those of RQW lasers.

## A.2. Theory

\* Developed a new method for calculating excitonic properties in quantum-confined semiconductor structures with arbitrary potential profiles in the presence of applied fields

A simple but highly efficient, accurate and versatile method to calculate the exciton binding energies, transition energies, oscillator strengths, and absorption coefficients in quantum wells with arbitrary potential profiles in the presence of electric and magnetic fields applied along the growth direction has been developed.

\* Effects Of parallel and perpendicular electric and magnetic fields on confined donor states in a coupled double quantum well

In a perpendicular configuration ( $B \perp E$ ), the magnetic field provides a confinement in both the growth direction and in the quantum well planes, directly competing with the electric field in affecting how wave functions will adjust in the external fields. In addition, components of the angular momentum are no longer conserved, which leads to mixing of the eigenstates of the angular momentum.

\* Effects of electric and magnetic fields on confined donor and exciton states in a dielectric quantum well

Analyses have been extended to study the properties of quantum wells having barrier and well materials with significantly different dielectric constants (such as GaAs-ZnSe). The interfacial image charge due to such a mismatch is modeled.

\* Hydrogenic impurities and exciton binding energies in quantum wires in the presence of a magnetic field.

We have calculated the binding energies of donors and both the heavy-hole and the light-hole excitons in a quantum wire (QW) with an infinite potential barrier, in the presence of a uniform magnetic field, as a function of the width of the quantum wire. The binding energy continues to increase as the radius of the wire decreases, while in the presence of magnetic field, additional increases for the binding energy are reported, especially for larger wire radii.

\* Hydrogenic donor states in quantum dots in the presence of a magnetic field

We have calculated the binding energy of a hydrogenic impurity in a quantum dot (assumed to be in the form of disc of radius  $R$  and length  $L$ ) with infinite potential barriers at all surfaces in the presence of a

uniform magnetic field applied parallel to the disk axis, for the case of an impurity ion located on the axis of the disk.

**\* A quantum statistical theory of excitonic linewidth due to compositional disordering in semiconductor alloys and quantum well structures**

We have developed a very general and a powerful quantum statistical formalism for calculating the excitonic luminescence linewidths and lineshapes in semiconductor alloys due to bandgap fluctuations caused by the random distribution of the alloy components in applied electric and magnetic fields. We apply this formalism to calculate the linewidths and lineshapes associated with the ground-state excitonic transition as a function of alloy composition and magnetic field strength in  $\text{Al}_x\text{Ga}_{1-x}\text{As}$  and  $\text{In}_x\text{Ga}_{1-x}\text{P}$  alloys.

**B. Status of the research effort: A substantive statement of significant accomplishments and progress toward achieving the research objectives.**

**1. Experimental realization of nonrectangular quantum well modulators - ASU**

**1.1. Arbitrary shaped quantum wells**

A major goal of this project was to investigate the use of quantum wells that have nonrectangular potential profiles as potential active regions in electro-absorptive modulators. This work concentrates on triangular quantum wells and compares their electrical and optical properties with rectangular quantum wells (RQWs) and coupled rectangular quantum wells. The scope of the project was expanded to include light emitting devices such as edge-emitting lasers and vertical cavity surface emitting lasers (VCSELs). Discussed in this section is the experimental portion of the program which included

- a) refinement of MBE growth of compositional graded quantum wells by the digital alloy approximation
- b) development of characterization tools for measuring intrinsic optical properties of quantum wells and devices fabricated from them
- c) fabrication of spatial light modulators, waveguide modulators, edge-emitting lasers and vertical cavity surface emitting lasers
- d) integration of two types of modulators to obtain novel operating characteristics.

Several of the major accomplishments have been listed in the previous section. Described here are some details of the experimental progress.

**1.1.1. ATOW structural and optical property correlation**

Accurate compositional grading in distances on the order of hundreds of angstroms are required to realize high quality quantum wells having arbitrary shapes. One problem in developing the compositional grading technique is that of characterizing the composition profile and QW thickness. This section describes a technique [1] that we use to measure the approximate composition by high resolution transmission electron microscopy (HREM) and calculate the quantum well energy levels using the measured profile. Briefly described is also a new Fourier solution [2] to Schrödinger's equation.

Rectangular quantum wells have been extensively used as active regions of opto-electronic devices. These rectangular symmetrical quantum wells have an overlap integral between the conduction ( $n=1$ ) and heavy hole ( $n=1$ ) wave functions that are very close to unity when no electric field is applied. However, in most opto-electronic devices the quantum well is subject to internal and external electric fields from the device. These fields cause a spatial separation of electron and hole wave functions that decreases the overlap integral between the conduction band and valence band wave functions. A reduction in the overlap integral implies a reduction in the emission or absorption process.



Asymmetric triangular quantum wells (ATQWs) were grown by molecular beam epitaxy (MBE) using a digital alloy method to study the material growth process. The digital alloy method divides the triangular well into a series of equally spaced alloy cells. The average aluminum composition in the alloy cell (typically 25 Å) is then approximated by shuttering the aluminum effusion cell such that the thickness of a layer of AlGaAs centered in the alloy cell provides enough Al to equal the required average Al composition. The ATQWs were then characterized by a new process involving high resolution transmission microscopy, computer simulation, and room temperature photoluminescence.

Room temperature photoluminescence measurements were taken with standard photon counting techniques. The resulting luminescence spectra, as seen in Figure 1, shows three features which have been associated with the  $E_{11h}$ ,  $E_{11l}$ , and  $E_{22l}$  transitions. The identification of these transitions is based on their energy separation. Further evidence to support the identification of the spectral features was obtained from the temperature dependent photoluminescence. At temperatures below about 77K the photoluminescence did not indicate a light hole transition ( $E_{11l}$  or  $E_{22l}$ ). As the sample temperature was increased, Fermi-Dirac statistics allow the light hole transitions to become more prominent due to thermal population of the higher energy states. The light hole transitions are clearly visible in the room temperature photoluminescence (figure 1).

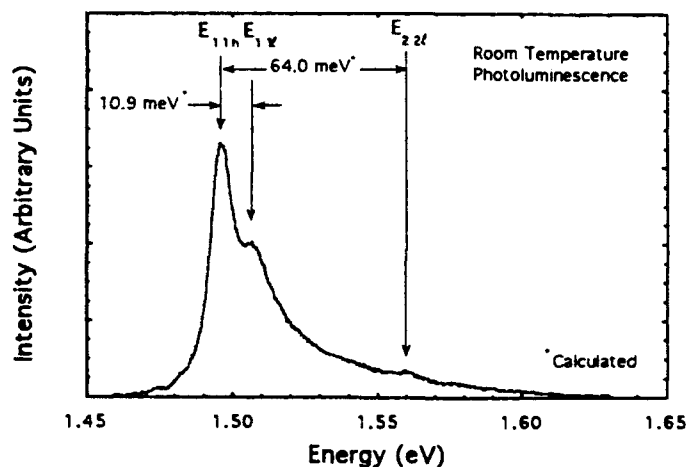


Figure 1 The room temperature photoluminescence spectrum of a GaAs/AlGaAs ATQW. The energy separation between the labeled spectral transitions was calculated using a Fourier series method and the HREM intensity profile.

To verify the well profile, a sample adjacent to the photoluminescence sample was chosen for HREM. Cross sectional specimens were prepared within the  $\langle 100 \rangle$  projection, i.e., with the electron beam parallel to this direction. This allows for structure-factor-difference (002) beams to contribute to the image and shows the layers within the well more clearly than the  $\langle 110 \rangle$  projection.

While high-resolution TEM is capable of resolving structural information about solids with atomic resolution, its chemical sensitivity is quite limited. In particular, the contrast of a micrograph usually does not reflect the chemistry of the constituent species. The intensity of any particular feature in a high-resolution micrograph is a complicated function of the atomic potential, crystalline orientation, thickness and defocus. For this work, both the well width and the Al concentration within the layers needed to be determined. The well width was obtained from high-resolution lattice images. To determine the chemical composition of the structure, advantage was taken of the nearly linear relationship between the (000) beam intensity and aluminum concentration for a certain range of thicknesses. Simulations show that for a specimen with a thickness in the range of 15 to 23 nm, the contrast between the layers is not only large,

but also directly proportional to the Al concentration. It is this linearity that allows the well profile to be determined.

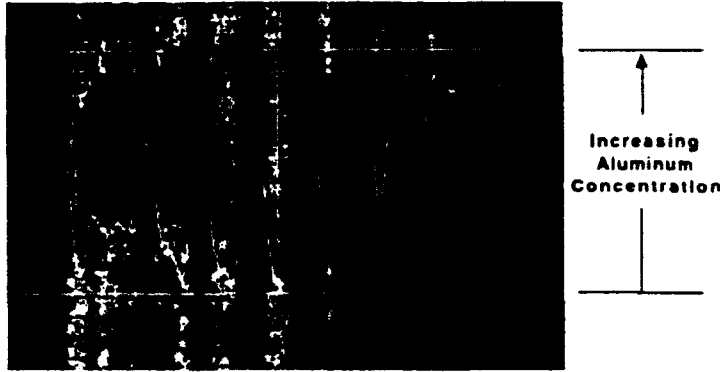


Figure 2 Micrograph from a cross sectional specimen. The HREM specimen was prepared within the  $\langle 100 \rangle$  projection. Superimposed on the micrograph is an intensity trace that has been averaged over the height of the image ( $\sim 300\text{\AA}$ ). The darker regions correspond to higher aluminum composition.

Figure 2 shows an image from the ATQW recorded at a magnification of 250kX using an objective aperture to exclude diffracted beams at a thickness estimated to be  $19 \pm 3$  nm. The indicated region of figure 2 was averaged perpendicular to the well to give the line scan which is superimposed on figure 2. At this thickness, a linear relationship between contrast intensity and Al concentration was assumed. Random contrast fluctuations due to sample preparation were ignored.

The transition energies of the HREM profile were calculated using the one dimensional form of the BenDaniel-Duke Hamiltonian [3], as given by

$$-\frac{\hbar^2}{2} \frac{\partial}{\partial z} \frac{1}{m^*(z)} \frac{\partial}{\partial z} \psi(z) + V(z)\psi(z) = E_n \psi(z), \quad (1)$$

and is used to solve for the envelope functions within the effective-mass approximation. By implementing the BenDaniel-Duke Hamiltonian, spatial changes in the effective mass are accounted for.

The envelope function,  $\psi(z)$ , can be expanded into a truncated Fourier series,

$$\psi(z) = \sum_{i=-N/2}^{N/2-1} c_i e^{-j2\pi iz/L} \quad (2)$$

where  $j = \sqrt{-1}$  and  $L$  is the total length obtained by combining the lengths of the quantum well and barriers. Likewise, the potential ( $V$ ) and the spatial dependence of the effective mass ( $m^*$ ) can be modeled by a Fourier series as

$$V(z) = \sum_{\ell=-N/2}^{N/2-1} d_{\ell} e^{-j2\pi \ell z/L}, \quad (3)$$

and

$$\frac{1}{m^*(z)} = \sum_{p=-N/2}^{N/2-1} f_p e^{-j2\pi pz/L}. \quad (4)$$

The Fourier series expressions of the envelope function, potential, and effective mass are then substituted into the Hamiltonian. Using the orthogonality of the Fourier series, the Hamiltonian reduces to

$$\frac{\hbar^2}{2L^2} \sum_{i=-N/2}^{N/2-1} f_{k-i} c_i ik + \sum_{i=-N/2}^{N/2-1} d_{k-i} c_i = E_n c_k \quad (5)$$

where  $E_n$  represents the eigen energies of the quantum well and  $c_i$  correspond to the Fourier coefficients of the corresponding envelope functions.

Aluminum Profile	$E_{11h} - E_{11l}$	$E_{11h} - E_{22l}$
Linear Grade	17.1 meV	96.9 meV
Digital Alloy	20.6 meV	94.2 meV
HREM Composition	10.8 meV	64.0 meV
Average Composition	7.1 meV	52.3 meV

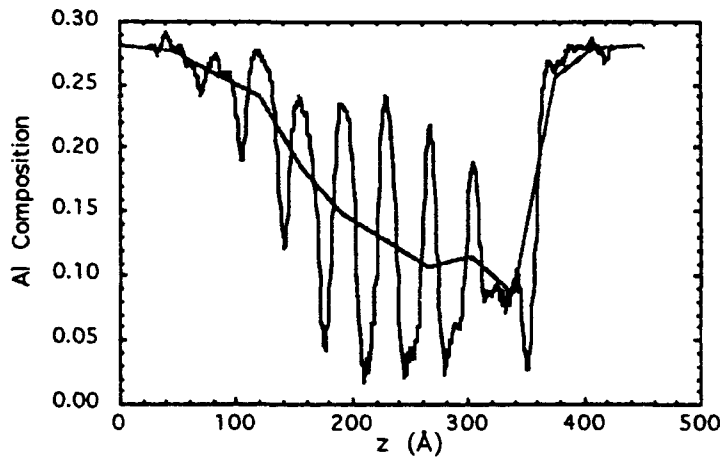


Figure 3 The Al composition profile as determined self consistently by HREM, simulation, and photoluminescence. The average Al composition is indicated by the bold line and indicates a rounding at the bottom of the ATQW.

Energy differences for the desired linear graded well and the digital alloy well were calculated (Table 1). Although these two wells compare quite favorably with each other, they differ from the measured separations. This indicates that the exact compositional profile is important to determine the optical properties of the quantum well. Subsequent work on ATQWs suggest that the rounding at the bottom of the well has been eliminated. The shape of the ATQWs is based on reflection high energy electron diffraction (RHEED) intensity oscillations taken during the growth of digital alloy wells and on the narrow full width at half maximum (FWHM) of the spectral features seen in 2K photoluminescence [4]. The transition energies in 2K photoluminescence has also shown agreement with theoretical values for a linearly graded well [5].

Table 1 Computed values of the  $E_{111} - E_{11h}$  and  $E_{221} - E_{11h}$  energy differences. Room temperature photoluminescence (figure 1) was used to measure the actual energy differences of 11 and 64 meV. See figure 2 for definition of the aluminum composition profiles.

### 1.1.2. Technique for accurately measuring absorption coefficients of quantum wells

To properly assess the electroabsorption performance of these materials and provide data which can be used in designing modulator devices, it is important to have accurate measurements of the absorption coefficient as a function of wavelength and electric field. This data can also be used for modulators operating primarily on electrorefraction effects, since the absorption spectra can be used to calculate the real part of the refractive index through the Kramers-Kronig relations [6]. Described here is a method that we developed specifically to aid in the design of quantum well based modulators [7].

There are a number of possible ways in which the absorption coefficient can be measured. Ellipsometry has been used to extract the real and imaginary parts of the refractive index of bulk semiconductors [8]. In the multilayered structures mentioned above, however, the refractive index is sensitive to the polarization of the light with respect to the plane of the layers and it is not clear how the index extracted from the delta and psi data, derived from the ratio of parallel to perpendicular polarization signals, should be interpreted. If a p-i-n diode structure is used, the absorption coefficient can be extracted from the photocurrent generated by the optical probe [9]. The accuracy of this depends on measurement of the optical power incident upon the device and on knowledge of the internal quantum efficiency of the absorbing material. Background doping in the "intrinsic" absorbing region of the device used for these measurements affects the generated photocurrent through incomplete depletion, adding uncertainty to the extracted absorption coefficient at low electric fields. If the diodes are leaky or need to be forward biased to reduce the built-in electric field, then the photogenerated current may be small compared to the total current measured, which reduces the accuracy of the measurement.

Normal incidence reflection and transmission measurements have also been used to extract the absorption coefficient of both bulk [10], [11] and layered structures [12], [13]. Typically, a simple analytical model which ignores interference effects within the test structure due to reflections at the air/semiconductor interfaces on either side is employed in order to simplify extraction of the absorption coefficient. Since interference effects are not accounted for, the Fabry-Perot oscillations which are normally present in the reflectance and transmittance spectra must be eliminated or large inaccuracies in the extracted absorption coefficient would result. Several methods have been used to eliminate interference effects. Two of these are the deposition of an antireflection coating (typically a single layer of dielectric) [14] or roughening of one interface with an etch [15]. Single-layer antireflection coatings are only effective over a narrow range of wavelengths, however. Errors in the thickness or refractive index of the coating will also make it imperfect which allows a reflected wave from the interface to cause some degree of interference and errors in the extracted absorption coefficient. Roughening one of the surfaces may cause some light transmitted through the structure to be scattered out of the view of the detector, which artificially increases the measured absorption coefficient. It may also be difficult to control the roughening process in a reproducible manner. A third technique is to make the absorbing layer thick enough that there is minimal feedback from the bottom interface of the structure [10]. For the epitaxial materials being considered for devices, however, it is generally not practical to grow such layers thicker than one to three micrometers.

We have developed [7] an approximate model is presented for the reflectance and transmittance of an epitaxial membrane which takes into account reflections at the air/semiconductor interfaces and the resulting wave interference effects. Using the model, the absorption coefficient,  $\alpha$ , can be solved for analytically with measured reflectance and transmittance as the inputs. This method allows many of the unknowns in the test structure and measurement to be removed which increases accuracy in the values of  $\alpha$ . This section describes the model for the type of test structure typically employed followed by an analysis of the errors in extracted absorption coefficient relating to the approximations in the model itself and to errors in the reflectance and transmittance values. A comparison is then made between the absorption spectra of bulk GaAs and of a 10nm GaAs/10nm  $Al_{0.3}Ga_{0.7}As$  multiple quantum well with measurements made using other techniques.

## II. The Approximate Model

A cross-section of the three-layer sample structure typically employed for electroabsorption measurements is shown in figure 4.

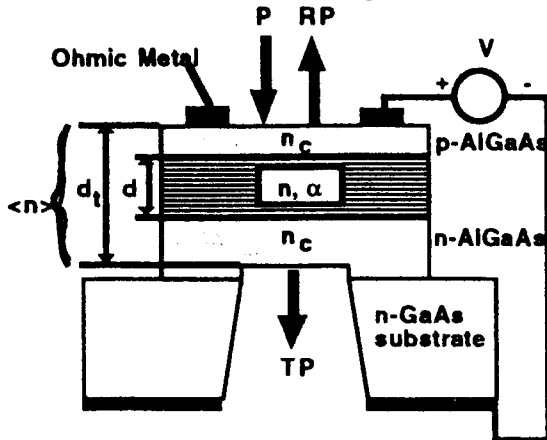


Figure 4. Schematic cross-section of the three-layer epitaxial p-i-n diode test structure used to measure the electroabsorption properties of MQW materials. The case for AlGaAs cladding layers on a GaAs substrate is shown and the parameters of the approximate model are indicated.

The top and bottom layer compositions are chosen to be transparent to light in the wavelength range of interest and are usually doped heavily p- and n-type, forming a p-i-n diode which is reverse biased to vary the electric field in the unintentionally doped middle absorbing layer. If the substrate is not transparent in the wavelength region of interest, a hole must be etched through it and stopped at the bottom cladding layer, leaving a membrane of the epitaxial structure intact over the hole. For materials grown on GaAs substrates, AlGaAs cladding layers are convenient since the composition can be adjusted for transparency and selective etches, which facilitate the processing, are available [16], [17]. When employing these etches, it is important to leave a very smooth surface at the etch stop layer since the model to be described assumes ideal air/semiconductor interfaces with no scattering loss.

In the model, it is assumed that the reflectance of the two air/cladding layer interfaces at normal incidence can be calculated from the refractive index of the cladding layer material,  $n_c$ , by

$$R_0 = \frac{(n_c - 1)^2}{(n_c + 1)^2} \quad (1)$$

Reflections at the two internal interfaces in the three-layer structure, between the cladding layers and absorbing layer, are ignored, however. This is the principal approximation in the model and it allows the three-layer structure to be treated as a single layer with average refractive index,  $\langle n \rangle$ , and total thickness,  $d_t$ . The refractive index difference between the absorbing and cladding layers is usually quite small. Thus, the error caused by this approximation is also small, as will be seen later. The absorbing layer has thickness,  $d$ , and an absorption coefficient,  $a$ , which is the parameter to be extracted from the measured reflectance and transmittance. The normal incidence reflectance,  $R$ , and transmittance,  $T$ , can be written as

$$R = \frac{R_0 (1 - e^{-ad})^2 + 4 R_0 e^{-ad} \sin^2(q)}{(1 - R_0 e^{-ad})^2 + 4 R_0 e^{-ad} \sin^2(q)} \quad (2)$$

$$T = \frac{(1 - R_0)^2 e^{-ad}}{(1 - R_0 e^{-ad})^2 + 4 R_0 e^{-ad} \sin^2(q)} \quad (3)$$

where,

$$q = \frac{4\pi \langle n \rangle d_t}{\lambda} \quad (4)$$

It is assumed that  $d$  is known from an independent measurement. The bottom cladding layer thickness is usually not known accurately since the selective etch may reduce its thickness by some unknown amount

before being terminated. This leaves the value of  $d_1$  (and thus  $q$ ) as an unknown. The terms involving  $q$  can be eliminated by solving (3) for  $4R_0 e^{-\alpha d} \sin^2(q)$  and substituting into (2). The resulting expression can be solved for  $a$  to give

$$a = -\frac{1}{d} \ln \left[ \frac{-(1-R)(1-R_0) + \sqrt{(1-R)^2(1-R_0)^2 + 4R_0T^2}}{2R_0T} \right] \quad (5)$$

The above relation allows a simple calculation of absorption coefficient from measured reflectance and transmittance data. Exact equations which include the complex refractive indices and thicknesses of all three layers could be solved numerically for the real and imaginary parts of the refractive index of the absorbing layer, but the layer thicknesses, particularly of the cladding layers, generally cannot be known with sufficient accuracy to produce reliable results.

A measurement error analysis study was made to determine the accuracy and sensitivity of the approximate model. The error tests were performed for the GaAs/AlGaAs system for which refractive index data is readily available [18], [19], [20] and has been included in a look-up table in the program for the exact calculations. The error due to the approximations in the model was examined as a function of both wavelength and absorption coefficient in the middle layer. The error is greatest for low values of  $a$  since, in this case, the middle layer is most transparent and interference effects from the internal interfaces are more pronounced.

The simulated structure has top and bottom cladding layers of  $0.5 \mu\text{m}$  and  $1 \mu\text{m}$  of  $\text{Al}_{0.3}\text{Ga}_{0.7}\text{As}$ , respectively. The absorbing middle layer is taken to be  $1 \mu\text{m}$  of a hypothetical material with the same real refractive index dispersion as GaAs, but an absorption coefficient which is wavelength independent. Except for the constant absorption coefficient, the above parameters are typical of test structures used to measure electroabsorption effects in MQW material. Figure 5 summarizes the results. The maximum value of error saturates at approximately  $\pm 7\%$  as the absorption coefficient is reduced. Error in  $a$  may also be caused by errors in the measured values of reflectance and transmittance. The maximum percent error, occurring at  $851.5 \text{ nm}$ , for values of  $a = 200, 2,000, \text{ and } 20,000 \text{ cm}^{-1}$  is plotted in figure 4(a) for deviations in reflectance and in figure 4(b) for deviations in transmittance.

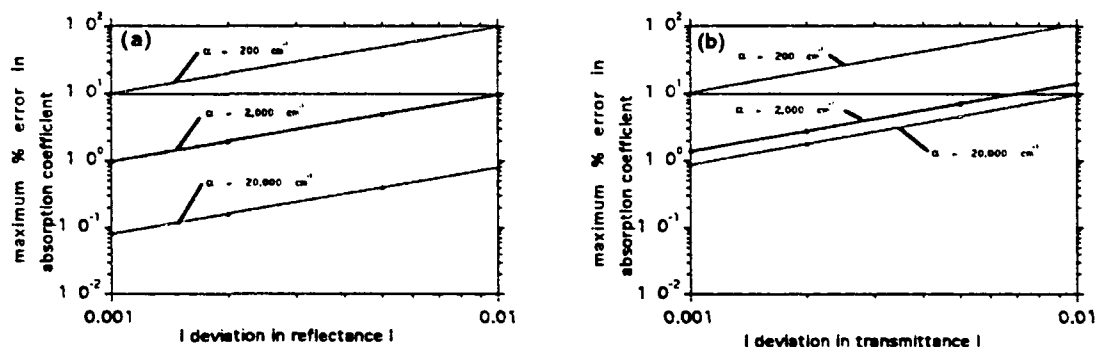


Figure 5 The calculated maximum percent error in extracted absorption coefficient as a function of deviation in measured (a) reflectance and (b) transmittance for various values of  $a$  in the middle absorbing layer.

The maximum error is approximately linearly dependent on  $dR$  and  $dT$  in all cases. Note that for small values of  $a$ , the error is quite large (10 to 100%) even for small deviations in the measured value of  $R$  and  $T$ . Also, as  $a$  increases, the error is much more sensitive to deviations in the measured transmittance than reflectance, as would be expected since the transmitted signal decreases exponentially with increasing absorption. For low values of  $a$ , deviations in the measured values of  $R$  and  $T$  will dominate since the error due to model approximations is less than about 7%. Deviations in  $R$  and  $T$  contribute approximately the same amount to the error. In general, it is difficult to measure low values of absorption coefficient accurately without increasing the thickness of the absorbing layer. In summary, the approximations used

to extract the absorption coefficient from the reflectance and transmittance data generally do not dominate the error in  $\alpha$  and contribute no more than 7% even for very small absorption values.

To test the model, the absorption spectra of two much-studied materials are extracted and compared to measurements made by others using different techniques or approximations.

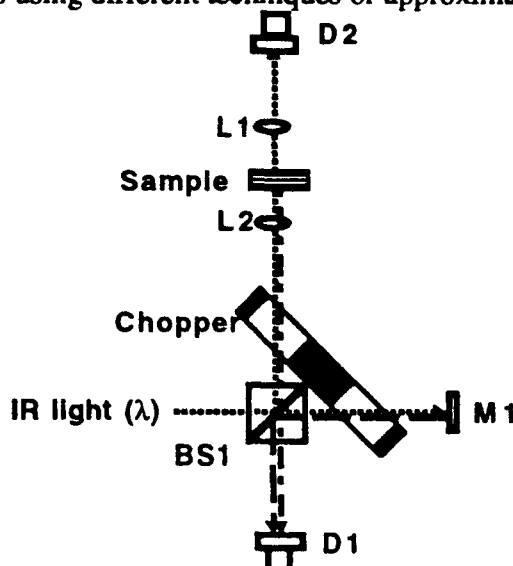


Figure 6. A diagram of a portion of the measurement set up used for simultaneous measurement of reflectance and transmittance at normal incidence. Beam splitter BS1 splits the incoming light into paths going to the sample and reference mirror M1. A two-window chopper time multiplexes the reflected signals from the reference mirror and sample onto detector D1. Lenses L1 and L2 focus the beam onto a device on the sample and detector D2 receives the transmitted beam.

The reflectance and transmittance measurements were made using the apparatus whose diagram is shown in figure 6. A  $\text{Ti:Al}_2\text{O}_3$  tunable laser was used as the light source. The incoming beam is split into two paths by beam splitter BS1, one to reference mirror M1 and one to the sample. The reflected beams from M1 and the sample return through BS1 and are time multiplexed on to detector D1 by a two-window chopper. The beam transmitted through the sample is incident on detector D2. The two detectors are silicon p-i-n photodiodes whose photocurrents are input to two current amplifiers with voltage waveforms digitized by a fast A/D board in a minicomputer. The waveform from D1 contains pulses due to the reflected signals from both M1 and the sample, as well as the background signal when both chopper windows are blocked during part of the cycle. The waveform from D2 contains only the pulse from the beam transmitted through the sample and its background signal when light to the device is blocked during part of the cycle. Noise due to power fluctuations in the laser is reduced by signal averaging. The background signal is subtracted from the reflected and transmitted signals. For values of  $R$  and  $T$  near unity, the noise is typically  $\pm 0.002$ , while for values near zero it is  $\pm 0.00025$ . Also, for values of  $R$  and  $T$  near zero, there can be an error as large as  $\pm 0.0005$  due to quantizing error in the 12-bit A/D conversion. The system is calibrated for transmittance by taking a measurement with no sample in place so that  $T = 1.0000$ . A wavelength-dependent correction factor derived from this is then applied to transmission measurements on the sample. Another reference mirror with a reflectance  $> 0.996$  over the wavelength range is similarly used to calibrate the system for reflectance values. The beam, at normal incidence to the sample, is focused to a  $25\text{-}\mu\text{m}$ -diameter spot by lens L1 with the power adjusted to give an intensity of approximately  $1\text{ W/cm}^2$  over the range of wavelengths used. This is low enough to avoid sample heating and excitonic saturation effects. All measurements were made at room temperature.

Figure 7 shows the extracted absorption spectra of sample 1, bulk GaAs, plotted with several other published measurements made using different techniques.

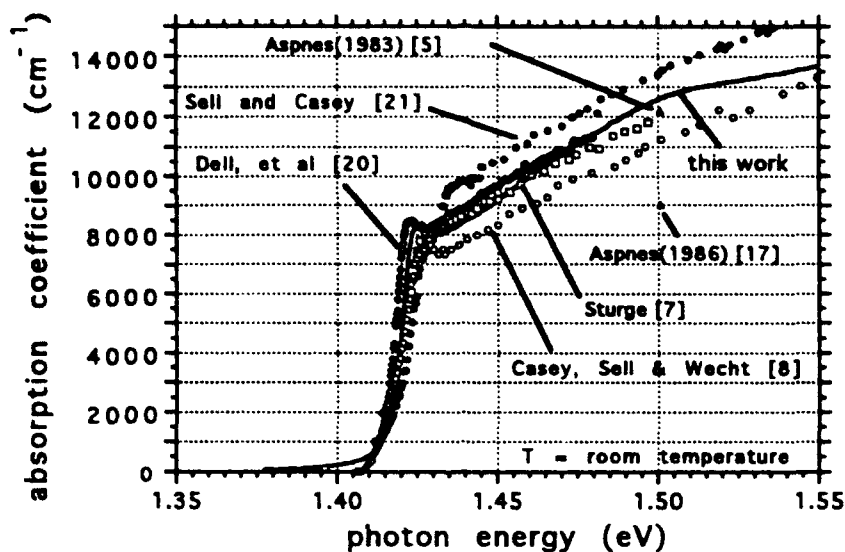


Figure 7. Comparison of the absorption coefficient of GaAs extracted using the model of this work with that measured by several groups, as indicated, using different techniques. All measurements were at room temperature (293 -298 K).

The excitonic peak at the absorption edge, normally seen at room temperature in high purity samples, is clearly visible in the data from this work. The closest agreement is between this work and the results of Dell, et al [23] whose sample was a single layer of MBE-grown GaAs lifted off and bonded to a quartz substrate with optical cement. They solved the exact nonlinear equations numerically for the reflectance and transmittance of two-layers, the GaAs and the optical cement, between infinite media, vacuum and the quartz substrate. Similar to this work, no surface roughening or antireflection coatings were used. There is a slight difference in the absorption edge between the measurements which may be due to small temperature differences between the samples or strain in the GaAs layer. There is also good agreement with the results of Sturge [10], who ground and polished GaAs samples to different thicknesses and extracted the absorption coefficient from transmission measurements alone. Absorption measurements were only made on samples thick enough (optical density greater than 0.5) to avoid Fabry-Perot interference effects, so again, roughening or antireflection coatings were not necessary. There is good agreement with the older results (1983) [8] but poor agreement with the more recent results (1986) [20] of Aspnes which were made by ellipsometry at 1.5 eV on a bulk GaAs sample. It is not clear why there is such a difference in the newer measurement. There is also a substantial difference between the data of Sell and Casey [24], Casey, Sell and Wecht [11] (high purity GaAs sample only) and this work. The data of Sell and Casey was taken on a three-layer structure very similar to that used here. Transmission measurements were made and the absorption coefficient extracted through use of an approximate model which neglects interference effects. The samples were grown by liquid phase epitaxy and the small amount of aluminum dragover from the AlGaAs cladding layers into the GaAs layer, which can occur in this growth technique, may be the reason for the shift in absorption edge to a slightly higher energy. It is possible that the difference in  $\alpha$  for energies above the absorption edge are due to errors in the thickness measurements of the GaAs layer and the neglect of interference effects. The data for high purity GaAs of Casey, Sell and Wecht was obtained from a Kramers-Kronig analysis of reflectance spectra for a  $\geq 1000$   $\text{cm}^{-1}$  with an estimated uncertainty of  $\pm 10\%$ .

Figure 8 shows the extracted absorption spectra of sample 2, a 10 nm GaAs/AlGaAs MQW, plotted with measurements from two other groups for GaAs quantum wells having thicknesses of 9.8 nm and 10.5 nm.



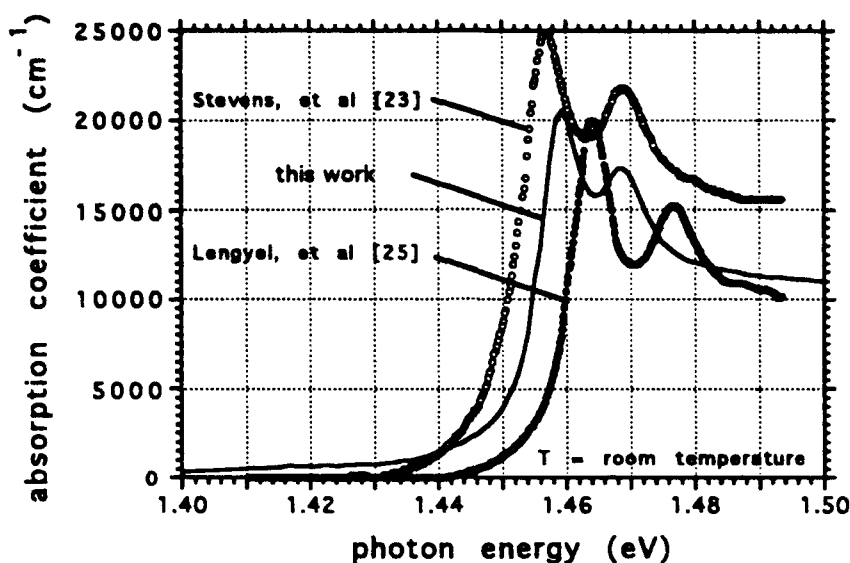


Figure 8. Comparison of the absorption coefficient of a 10 nm GaAs/10 nm  $\text{Al}_{0.3}\text{Ga}_{0.7}\text{As}$  multiple quantum well region extracted using the model of this work with that obtained by Stevens, et al [25], [26], using photocurrent measurements on a 9.8 nm well and Lengyel, et al [27], [28] using transmittance measurements alone on a 10.5 nm well. The absorption coefficient is for the wells alone, excluding the barriers, and all measurements were done near room temperature.

The absorption coefficient at zero applied voltage has been plotted for the quantum wells alone, excluding the barriers. There is considerable spread in the data and it is difficult to determine the reasons for the discrepancies. The data of Stevens, et al [25], [26] was derived from photocurrent measurements and is almost uniformly larger than that of this work by a factor of approximately 1.2. If the intrinsic MQW region of their sample was not fully depleted at zero bias, an artificially lower value of absorption coefficient would be obtained. It is possible that the optical power entering the MQW region was underestimated. The sample of Lengyel, et al [27], [28] had an antireflection coating of  $\text{Si}_3\text{N}_4$  deposited on top of the optical window and a simple equation which ignores interference effects was used to extract the absorption coefficient. The well width was stated to be 105 Å which should have placed the lowest absorption peak at a lower energy than any of the others on the plot, so perhaps there is an error in well width determination. There is good agreement in the absorption coefficient at the heavy hole peak, but a substantial difference at the light hole peak. It is possible that this is due to a variation in the effectiveness of the antireflection coating with wavelength.

In summary, we have developed a simple, accurate measurement system which allows extraction of absorption coefficient from reflectance and transmittance data taken from the common three-layer structure used for electroabsorption measurements has been presented. It takes into account the Fabry-Perot oscillations in the R and T data, eliminating the need to roughen surfaces or employ antireflection coatings which reduce the reliability of the measurement. It also allows absorbing regions of practical thickness to be used. The approximation of ignoring the internal interfaces in the structure contributes only small error to the measurement. In most instances, uncertainty in the thickness of the absorbing region or in the reflectance and transmittance data dominate the error. This measurement has been used to measure the intrinsic absorption coefficients in free standing, arbitrary shaped quantum wells as well as ON/OFF reflectance of spatial light modulators described in subsequent sections.

### 1.1.3. Comparison of absorption coefficients in ATQW and RQW

Presented here is the first detailed experimental comparison of electroabsorption in equivalent rectangular and asymmetric triangular multiple quantum wells [29]. The absorption spectra are extracted

from reflectance and transmittance measurements. To make a valid comparison of the two types of quantum wells, they must both be designed to modulate light at the same operating wavelength [30]. Generally, this means setting the widths of the two wells such that the lowest excitonic absorption peaks lie at the same photon energy for zero applied electric field. Figure 9 shows a plot of the calculated transition energy of the first electron-heavy hole exciton ( $E_{1hh}$ ) as a function of well width at 0 K and zero electric field for both rectangular (RQW) and asymmetric triangular (ATQW) quantum wells [31].

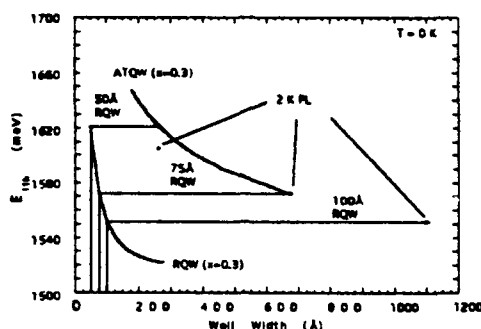


Figure 9. A comparison of the lowest excitonic transition energy as a function of well width in rectangular (RQW) and asymmetric triangular (ATQW) GaAs/ $\text{Al}_{0.3}\text{Ga}_{0.7}\text{As}$  quantum wells at zero applied field and  $T = 0^\circ\text{K}$ . The curves are calculated and the points are from  $T = 2^\circ\text{K}$  photoluminescence measurements.

In both cases, the barriers are  $\text{Al}_{0.3}\text{Ga}_{0.7}\text{As}$ . The wells are of GaAs for the RQW and a linearly-graded alloy of  $\text{Al}_x\text{Ga}_{1-x}\text{As}$  with  $x$  ranging from 0 to 0.3 for the ATQW. Also plotted are values of  $E_{1hh}$  from 2 K photoluminescence measurements on three ATQW samples with well widths of 265 Å, 675 Å, and 1100 Å. It is apparent that the ATQW must be much wider than its RQW equivalent for modulation of light at the same photon energy. For example, a 675 Å ATQW would be needed to place the absorption edge at the same photon energy as that of a 75 Å RQW. In [30], the calculated absorption of a 676 Å ATQW was compared with that of a 75 Å RQW and it was concluded that for an electroabsorption modulator, the ATQW would allow superior performance over the RQW because its much greater width allows a greater fraction of the MQW to be composed of absorbing quantum wells and not the nonabsorbing barriers between the wells. Also, a greater fractional change in absorption at the lowest peak for a given electric field was predicted. However, equation (19) in [30] indicates that the absorption coefficient at an excitonic peak is directly proportional to the oscillator strength of the transition and inversely proportional to the width of the quantum well. The calculated oscillator strengths at zero electric field for the  $E_{1hh}$  transition were reported to be  $26.2 \times 10^{-5} \text{ Å}^{-2}$  for the 75 Å RQW and  $25.3 \times 10^{-5} \text{ Å}^{-2}$  for the 675 Å ATQW. Using these oscillator strengths and well widths in the equation gives a zero-field absorption coefficient at the  $E_{1hh}$  peak for the 75 Å RQW which is a factor of 9.3 greater than that of the 675 Å ATQW. This suggests that the absorption spectra of the ATQW is scaled down by a factor which will not be fully compensated by the larger fraction of MQW occupied by the ATQW. Electroabsorption modulator performance depends upon the magnitude and absolute change of the absorption coefficient, not the fractional change, so such a reduction in absorption would make the ATQW a poor choice as a replacement for the RQW.

Samples for measurement of absorption spectra of RQW and ATQW at zero electric field were grown by molecular beam epitaxy (MBE) on semi-insulating GaAs (100) substrates at a temperature of  $600^\circ\text{C}$  and a growth rate of  $0.85 \mu\text{m/hr}$  for GaAs. For both samples, a 2500 Å GaAs buffer was grown, followed by 200 Å AlAs, 10,000 Å  $\text{Al}_{0.3}\text{Ga}_{0.7}\text{As}$ , the MQW, 5000 Å  $\text{Al}_{0.3}\text{Ga}_{0.7}\text{As}$  and a 20 Å GaAs cap layer. The MQW consisted of 80 Å  $\text{Al}_{0.3}\text{Ga}_{0.7}\text{As}$  barriers in both samples, with 50 wells in the RQW sample and 11 wells in the ATQW sample. All layers were nominally undoped to avoid any built-in field which would occur had the MQW been placed in a p-i-n diode configuration. The linearly-graded alloy composition in the wells of the ATQW sample was obtained by the pulsed MBE (PMBE) technique [32], in which the grading is achieved by growing a series of discrete layers of GaAs and  $\text{Al}_{0.3}\text{Ga}_{0.7}\text{As}$  to approximate the profile. The pulse period length was 25 Å, giving 27 periods for the 675 Å ATQW. Photoluminescence measurements on the ATQW sample at 2 K showed a peak for the  $E_{1hh}$  transition at

1572 meV, in agreement with calculations [30]. Photoluminescence measurements on the RQW sample showed a peak for the  $E_{1hh}$  transition at 1567 meV, indicating that the quantum well was slightly wider than the target value of 75 Å. From the calculated curve of figure 9, the width of the RQW is estimated to be 80 Å. This difference is not large enough to significantly affect the comparison made here, however.

Samples were prepared for absorption measurements by removal of the substrate with a selective etch [33, 34] which was stopped at the bottom  $\text{Al}_{0.3}\text{Ga}_{0.7}\text{As}$  layer. The reflectance and transmittance of the  $\text{Al}_{0.3}\text{Ga}_{0.7}\text{As}/\text{MQW}/\text{Al}_{0.3}\text{Ga}_{0.7}\text{As}$  epitaxial layer were measured as a function of wavelength at 293 K using a Ti:Sapphire tunable laser as the light source. Pronounced Fabry-Perot oscillations were observed in the data due to the mirrors formed by the  $\text{Al}_{0.3}\text{Ga}_{0.7}\text{As}/\text{air}$  interfaces on either side of the epitaxial membrane, but the absorption coefficient of the MQW region,  $a(l)$ , can be extracted from these measurements by simultaneous solution of the equations for the reflectance and transmittance of the structure. The measurements were made over a range of optical intensities to check for possible excitonic saturation effects and sample heating. The intensity used in the measurements,  $1.0 \text{ W/cm}^2$ , was well below the point at which changes were observed in the absorption spectra. Figure 10 shows a plot of  $a(l)$  for the RQW and ATQW in which the absorption is calculated for the quantum wells alone, excluding the barriers between them.

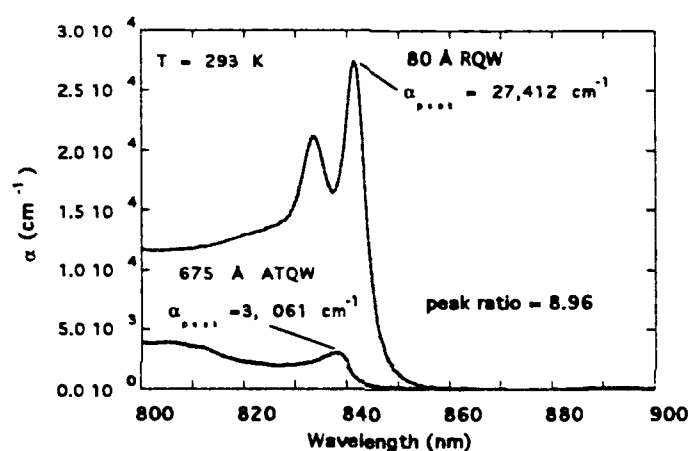


Figure 10. A comparison of measured absorption spectra at zero electric field and  $T = 293^\circ\text{K}$  for 80 Å rectangular (RQW) and 675 Å asymmetric triangular (ATQW) quantum wells. The ratio of RQW to ATQW absorption coefficient at the longest wavelength peak is 8.96.

The ratio of absorption coefficients of RQW to ATQW at the longest wavelength peak is 8.96, in good agreement with the value of 9.3 calculated above.

To check electroabsorption behavior, an 1100 Å ATQW sample was grown in a similar test structure except that the top and bottom  $\text{Al}_{0.3}\text{Ga}_{0.7}\text{As}$  layers were doped p- and n-type, respectively, and an n+ GaAs substrate was used to form a p-i-n diode. The width of the ATQW was chosen to set the absorption edge at the same wavelength as a 100 Å RQW whose electroabsorption behavior is well characterized [35]. Figure 11 shows absorption spectra at three values of applied voltage with the corresponding estimated electric field values.

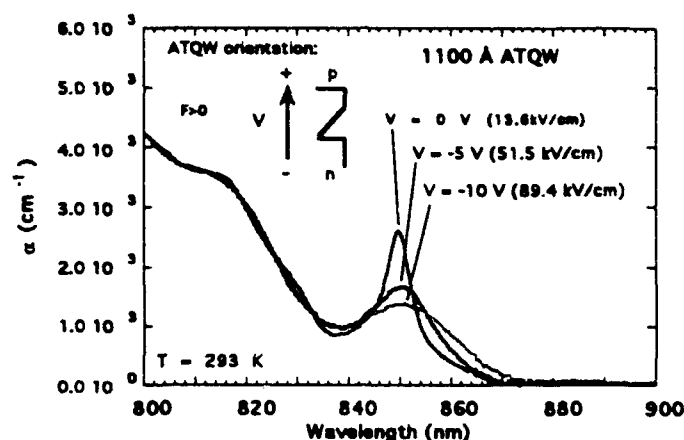


Figure 11. Measurements of electroabsorption on an 1100 Å asymmetric triangular quantum well (ATQW) at  $T = 293$  K. The well orientation with respect to the applied field is indicated on the plot as are the estimated values of electric field corresponding to the applied voltages.

The orientation of the graded-well profile with respect to the applied field,  $F$ , is indicated and corresponds to positive values as defined in [30]. Again, the entire absorption spectrum is scaled down compared to that of the equivalent RQW. In [30], the absorption coefficient at the lowest energy peak was normalized to its zero field value which eliminates magnitude information in the comparison of the two well types. When compared to absorption data for a 100 Å RQW, the ATQW does have a larger fractional change in absorption for a given applied field, but the absolute change is much smaller. The change in absorption between 0 volts (13.6 kV/cm) and -10 volts (89.4 kV/cm) bias at the longest wavelength peak (849.8 nm) is  $1373 \text{ cm}^{-1}$  (52.1%) in the 1100 Å ATQW and  $9511 \text{ cm}^{-1}$  (45.7%) in the 100 Å RQW. At longer wavelengths, there is also a much smaller change of absorption in the ATQW. We conclude, therefore, that ATQWs will not improve electroabsorption modulator performance, contrary to earlier predictions.

#### 1.1.4. Coupled Double Quantum Wells (CDQW)

An alternate approach for an optical modulator is to use coupled double quantum wells (CDQW). Two type of CDQWs have been explored, the asymmetric and the symmetric. Initially, a one micron buffer layer of AlGaAs was grown. Followed by 33 coupled wells separated by 80 Å of AlGaAs. The profiles for the active regions are shown in the insets of Figure 12. Finally a 0.5 μm AlGaAs cap layer was grown.

The double peak in the symmetric CDQW is due to a monolayer change in the well width of the top layers of the multiple quantum well structure. The arrows denote the calculated transition energies. The 2 K photoluminescence line width is a respectable 2. meV. These calibration runs have allowed for the design of CDQW optical modulators described in a later section.

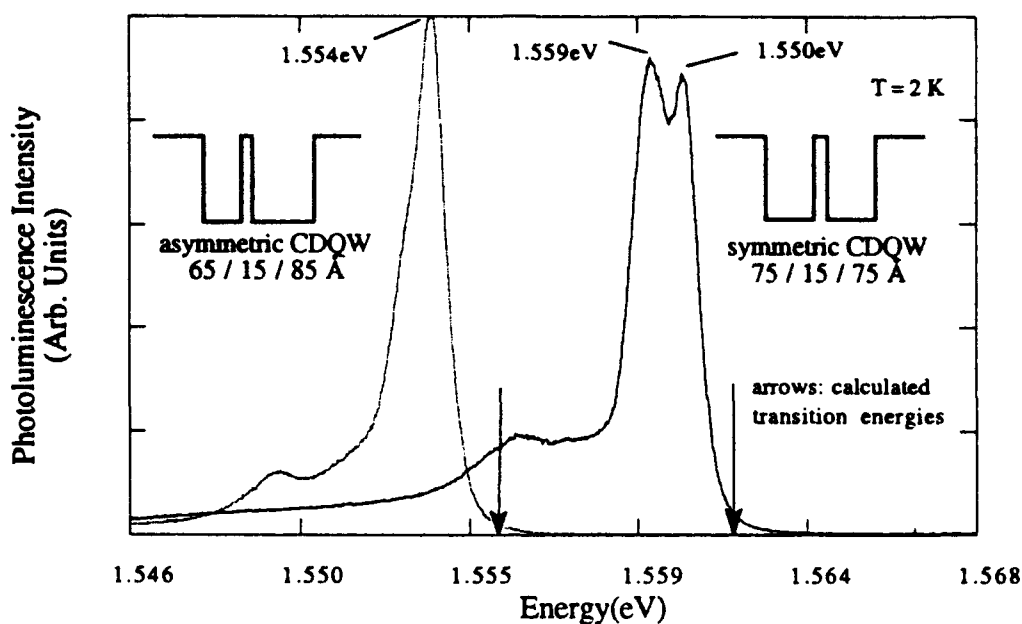


Figure 12 Photoluminescence from symmetric CDQWs and asymmetric CDQWs.

### 1.1.5. InGaAs/GaAs and InGaAs/AlGaAs ATQW

Although there is a difference in lattice constant between  $\text{In}_x\text{Ga}_{1-x}\text{As}$  ( $0 < x \leq 1$ ) and GaAs, epilayers can be grown coherently provided the InGaAs layer is made thin enough so as not to exceed the critical thickness. In this case the lattice mismatch is wholly accommodated by elastic strain; the lattice constant of the epilayer will be the same as that of the substrate resulting in the InGaAs layer being in compression. Also, because of tetragonal distortion the lattice constant in the growth direction will be larger than its bulk value. The effect of the biaxial compressive strain in pseudomorphic InGaAs/GaAs structures is to increase the energy gap. In addition, the increase in the lattice constant perpendicular to the growing surface lifts the degeneracy at the bulk Brillouin zone center by raising the heavy hole energy level with respect to the light hole level [36]. The degeneracy of the light and heavy hole states can further be lifted by confinement as in a quantum well. Various quantum well devices demonstrated using the InGaAs/GaAs system have utilized rectangular wells in which there is an abrupt change in the In composition at the heterointerfaces. These structures, for example, have been used to attain light modulation by electroabsorption and the quantum-confined Stark Effect [37]. However, recent theoretical and some experimental studies on the GaAs/AlGaAs system have shown that by changing the well profile to asymmetric triangular the performance of a spatial light modulator is greatly enhanced [38, 39, 40-42]. Described here are results on rectangular and asymmetric triangular InGaAs/GaAs single quantum wells [43,44] which exhibit sub-meV photoluminescence linewidths.

During growth of the ATQWs reflection high energy electron diffraction (RHEED) intensity oscillations were clearly observed indicative of layer by layer growth. For the InGaAs/GaAs ATQW the RHEED pattern during and at the end of the growth remained two dimensional (2D) with no evidence of lattice relaxation [45]. The total thickness of the individual InGaAs layers in the structures were well below the critical thickness.

Prior to the growth of a strained InGaAs/GaAs ATQW, a series of rectangular quantum wells were grown. The substrate temperature during growth was  $500^\circ\text{C}$  and a GaAs growth rate of  $0.8\text{ }\mu\text{m/hr}$  and a  $\text{As}_4/\text{Ga}$  flux ratio of 1.7 was used. Figure 13 shows the 2K PL spectra for a  $100\text{ }\text{\AA}$  rectangular InGaAs/GaAs well.

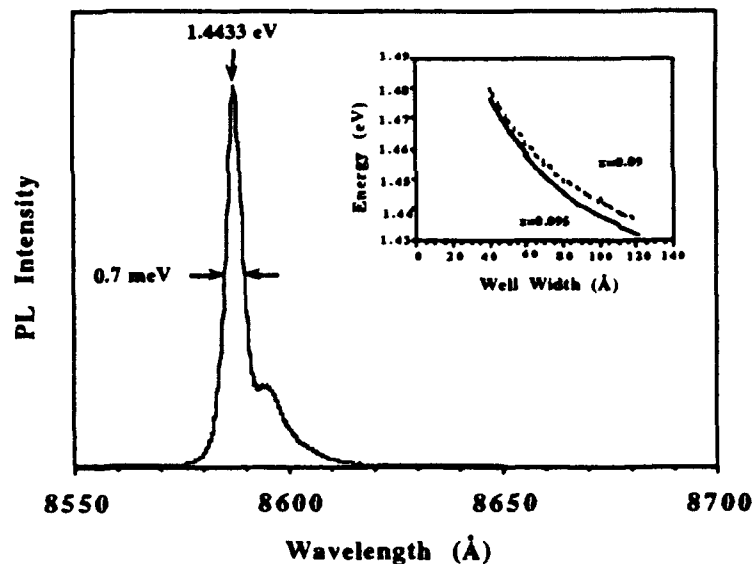


Figure 13. 2K photoluminescence spectrum of a single 100Å  $\text{In}_{0.095}\text{Ga}_{0.905}\text{As}/\text{GaAs}$  rectangular quantum well. Also shown (inset) are the calculated energy transitions for an In composition of 9.5% (solid line) and 9% (dashed line) together with experimentally measured data points.

The In mole fraction in the well as determined by RHEED intensity oscillations was 9.5%. The spectrum shows a strong excitonic feature which is due to the recombination between the  $n=1$  electron and the heavy holes. The FWHM of the excitonic feature is 0.7 meV indicating extremely high quality InGaAs as well as smooth heterointerfaces. In this structure there was a 10 secs growth interruption only at the bottom InGaAs on GaAs interface. The narrow linewidth observed for this well suggests very little alloy clustering and strain inhomogeneities. The peak energy position is a result of the combination of the quantum confinement and the elastic strain. The inset in figure 13 shows a plot of the  $n = 1$  electron to heavy hole transition as a function of well width for an alloy composition of 9.5%. The solid line is the calculated energies obtained from a solution of the time independent Schrödinger equation applied to a finite potential assuming a 60% conduction band offset. The points in the figure represents the measured energy positions from PL. Also shown, as the dashed line, are the calculated energies for an In composition of 9.0% which results in a closer fit to the experimental values. The apparent deviation from the target In mole fraction may be due to MBE shutter flux transients. Figure 14 shows the PL spectrum for a 400Å  $\text{In}_{0.095}\text{Ga}_{0.905}\text{As}/\text{GaAs}$  ATQW taken at 2K exhibiting a FWHM of 0.6 meV.

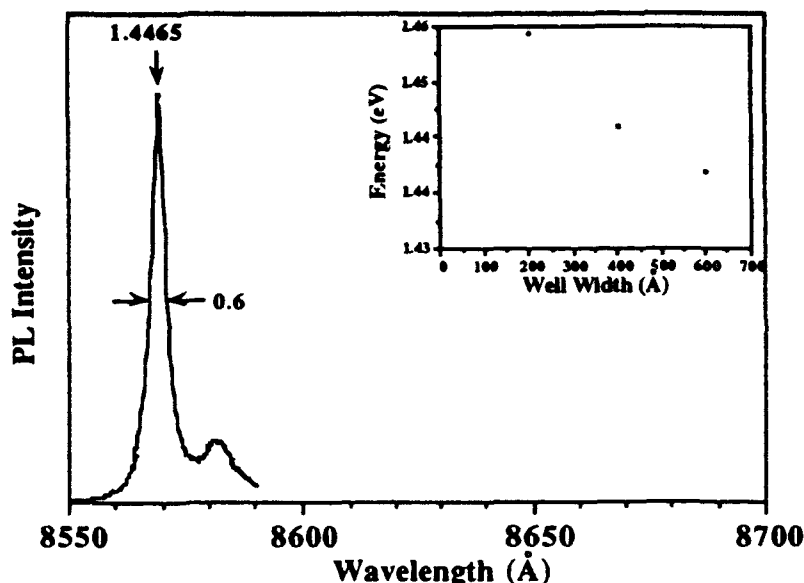


Figure 14. 2K photoluminescence spectra of a 400Å  $\text{In}_{0.095}\text{Ga}_{0.905}\text{As}/\text{GaAs}$  asymmetric triangular quantum well. The inset shows the measured energy of the heavy hole transitions as a function of well width.

This represents the first sub-meV linewidth for an ATQW. In this structure there is one abrupt heterojunction which reduces any interface roughness that may be present although the linewidth broadening due to alloy disorder would be the same for both type of wells. The inset in figure 14 plots the measured energies of the heavy hole peaks as a function of the well width. As with the  $\text{GaAs}/\text{AlGaAs}$  system for an optical device operating at a particular wavelength, the well thickness would be larger if a ATQW is used. This would reduce any effect of interface roughness on the excitonic linewidths and would also increase the total absorption since there would be more well material. From these results the linewidth for the  $\text{InGaAs}/\text{GaAs}$  ATQW is smaller than the rectangular QW. This is important for the operation of an optical absorption modulator since as the linewidth decreases, the absorption edge becomes more abrupt resulting in an increase in the contrast ratio for a given voltage swing [41, 42].

## 1.2. Distributed Bragg Reflectors (DBR)

### 1.2.1. In situ Measurements of AlGaAs/GaAs Bragg Reflectors by Spectroscopic Ellipsometry

To realize asymmetric Fabry Perot devices that have high ON/OFF ratios, it is necessary to control the quality of the dielectric mirror stack which form the Distributed Bragg Reflector (DBR) resonant cavity. We have developed spectroscopic ellipsometry (SE) as an in-situ MBE growth diagnostic [46] to grow structures more reliably and have also achieved record high reflectance DBRs.

Dielectric mirrors require layer thickness uniformity among successive periods to produce high reflectance in a given wavelength range. This uniformity is a result of interface flatness and a random or systematic variation thickness in successive layers. Interface roughness degrades the peak reflectance [48] while systematic and random thickness variations skew and increase the side lobe reflectance respectively. Our calculations show that the thickness deviation required to maintain near peak reflectance in a DBR stack is less than 8% for a 20 period DBR. The design of a mirror presented here with stop band centered at 867nm consists of  $\text{AlAs}/\text{Al}_{0.2}\text{GaAs}$  quarter wavelength layers of thicknesses 728Å and 628Å respectively. Thus a maximum 8% variation imposes the requirement that the optical thickness (= layer thickness/index of refraction) variation among the layers be less than 58Å and 50Å respectively. This tolerance must be maintained over a relatively thick (2.7μm) 20 period mirror with control over both epitaxial layer thickness and alloy composition. The problem is increased in a vertical cavity structure

where two Bragg reflectors must be stacked with an intermediate quantum well gain region. An in situ monitoring and control technique such as SE is thus desirable for such complicated structures.

A growth temperature of 623°C measured by optical pyrometer or 616°C by SE (750°C as measured by the MBE thermocouple) was used to grow the 20 period DBR with thicknesses mentioned previously centered at 867nm. To reduce interface roughness, the  $\text{Al}_{0.2}\text{Ga}_{0.8}\text{As}$  quarter wave layers were approximated by a GaAs and  $\text{Al}_{0.3}\text{Ga}_{0.7}\text{As}$  superlattice. The mirror was grown on a 3300Å  $n^+$  GaAs buffer on an  $n^+$  substrate.

The AlAs optical constants [46] for the growth temperature were used to fit the ellipsometric data for thickness and alloy composition. Before growth, a full spectroscopic scan (200 - 770nm) was performed on the GaAs substrate to measure the temperature.  $\Psi$  and  $\Delta$  were then measured at three wavelengths; 3500Å, 5500Å and 6500Å at a rate of one point (three wavelengths) every three seconds. Full spectroscopic scans were performed after the growth of periods 1, 2-5, 6-10, 11-15 and 16-20 to illustrate the thickness variation among successive layers and to monitor the evolution of the mirror reflectance. The growth rate was calibrated by SE after the growth of period 1. Figure 15 is a plot of the  $\Psi(t, 3500\text{Å})$  data with the aforementioned intervals superimposed.

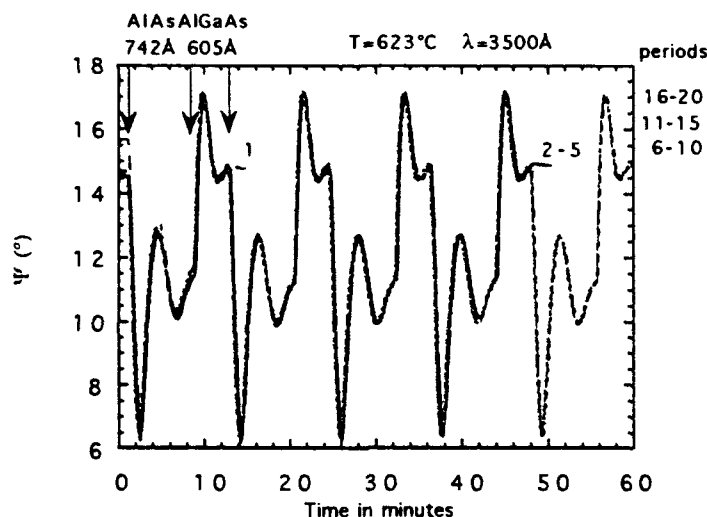


Figure 15. Dynamic growth monitoring of a 20 period AlAs/AlGaAs distributed Bragg reflector in the MBE at the growth temperature of 623°C. The periodicity of the mirror is evident in  $\Psi$  as a function of time. Superimposed are the curves of periods 1, 2-5, 6-10, 11-15 and 16-20 identified when the periods end. The time axis has been shifted such that successive period scans begin at  $t=0$ . A high degree of thickness and alloy composition reproducibility is evident from the superimposed curves.

While  $\Psi$  and  $\Delta$  for all three wavelengths were used in the structural calculations, only  $\Psi$  is plotted for illustrative purposes. The time axes on the successive mirror portions were shifted such that each portion began at  $t=0$ . The numbers in figure 2 indicate the times where the data for each portion ended and the arrows denote the AlAs and  $\text{Al}_{0.2}\text{Ga}_{0.8}\text{As}$  superlattice (SL) layers. The reproducibility of  $\Psi$  in subsequently grown layers shows that there is a high degree of optical thickness uniformity among all the periods of the DBR indicating a high effusion cell flux stability. The thickness and growth rate were calculated dynamically during the growth and compared well with the RHEED oscillations. RHEED measured growth rates of 97.6Å/min and 154.4Å/min for AlAs and the  $\text{Al}_{0.2}\text{Ga}_{0.8}\text{As}$  SL layers respectively while SE measured 95.3Å/min and 156.8Å/min for AlAs and the  $\text{Al}_{0.2}\text{Ga}_{0.8}\text{As}$  SL layers respectively. An effective medium approximation was used for analyzing the superlattice regions. This assumption of a uniform average alloy composition for the superlattice proved to be sufficiently accurate for this application.

Figure 16 shows SE scans after the growth of the various mirror portions with the substrate scan included for reference.  $\Psi$  is plotted since it is the ratio of the amplitude change upon reflection (eq. 1) and



thus is more closely related to the normal incidence reflectance than is  $\Delta$ . It is interesting to note that the maximum value of  $\Psi$  saturates with increasing number of periods at approximately 15 as does the normal incidence reflectance. Evolution of the side lobes is also evident in the  $\Psi(\lambda)$  curves for periods greater than 5.

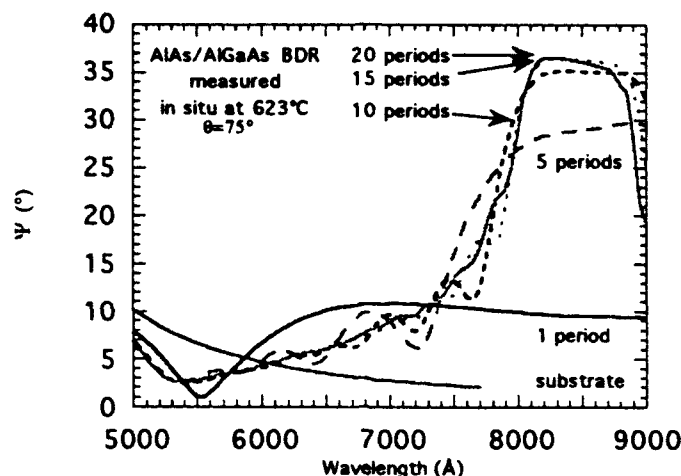


Figure 16. Measurement of  $\Psi$  versus wavelength of a distributed Bragg reflector at the growth temperature of 623°C in the MBE. The spectra were taken before the epitaxial structure was grown and after the growth of 1, 5, 10, 15 and 20 periods of the mirror. The angle of incidence of the incident light was 75°.

It should be noted that  $\Psi$  and  $\Delta$  are measured at oblique incidence (75°) and cannot be converted to an absolute, normal incidence reflectance using just a two layer model. The normal incidence reflectance can, however, be obtained from  $\Psi$  and  $\Delta$  if the structural information (thicknesses and optical constants) is used and an analysis similar to the scattering matrix approach [49] performed.

Normal incidence reflectance was measured against a standard reflector using a measurement system of our own design which alternates the reference and reflected beams onto one detector. Plotted in figure 17 is the calculation for the nominal design structure centered at 8670Å, the calculation for a mirror using the ellipsometrically determined thicknesses and compositions (at the growth temperature of 623°C) and the measured reflectance of the DBR discussed in this section.

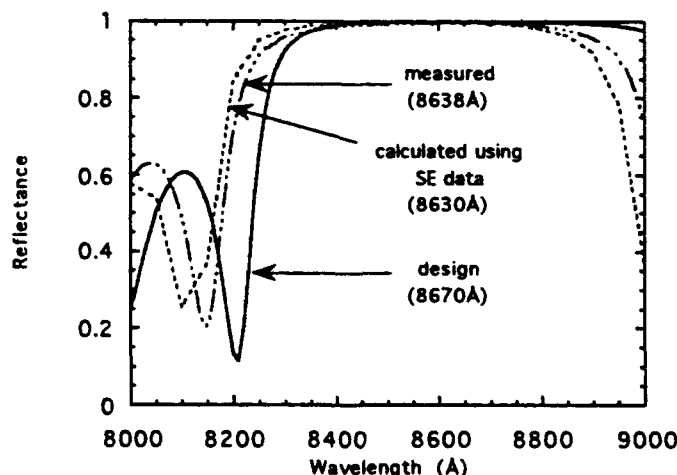


Figure 17. Normal incidence reflectance of a 20 period AlAs/AlGaAs distributed Bragg reflector. The mirror was designed for  $\lambda=867\text{nm}$ . The as-grown structure parameters were measured by SE at  $623^\circ\text{C}$ . Measured and calculated reflectance curves for the mirror are shown.

Thicknesses of the AlGaAs (superlattice) and AlAs were  $606.2\text{\AA}$  and  $742.5\text{\AA}$  respectively and  $x=0.19$  and  $1.0$  respectively as measured by SE at the growth temperature. The peak reflectance was measured to be  $0.995\pm 0.004$  at  $\lambda=8638\text{\AA}$  ( $32\text{\AA}$  from the design value) as compared to the calculated  $0.997$  at  $8630\text{\AA}$ . This reflectivity is higher than any previously reported for a 20 period DBR.

In summary, we showed that SE is a viable in situ monitoring technique for growth of III-V photonic devices. SE can be used to measure substrate temperature, growth rate, alloy composition, thickness and heterojunction interface properties. It can also be used to monitor the evolution of reflectivity and the stop band in distributed Bragg reflectors. Combination of all these aspects of SE with MBE can thus provide the material grower with information for control of complicated structures required to realize reproducible photonic device operating characteristics.

### 1.3. Spatial Light Modulators

#### 1.3.1. Fabrication of Spatial Light Modulators

Processing of optical modulators has taken place in three areas: AlGaAs/GaAs transmission modulators, InGaAs/GaAs transmission modulators, and AlGaAs/GaAs reflection modulators. Each type of modulator requires special processing steps because of the transmission properties of the substrate. In the case of AlGaAs/GaAs modulators, the optical transmission wavelength takes place above the band gap of GaAs. Therefore, the GaAs substrate must be removed or thinned to reduce absorption in the substrate. The InGaAs/GaAs transmission modulator benefits from the fact that the transmission energy can be tuned to less than the band gap of GaAs and therefore, the substrate does not require removal. Lastly, neither InGaAs/GaAs or AlGaAs/GaAs reflection modulators require the removal of the substrate.

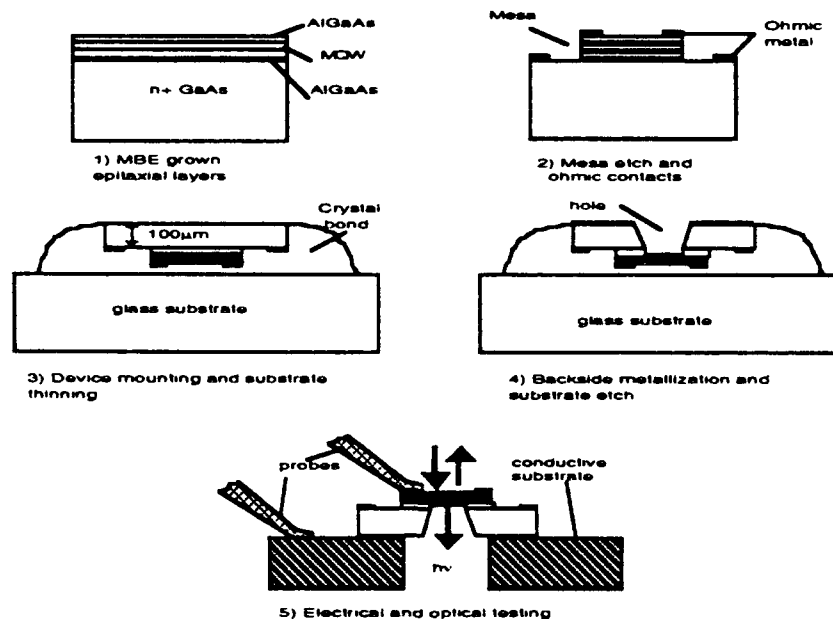


Figure 18 AlGaAs/GaAs optical modulator fabrication steps.

AlGaAs/GaAs pin-transmission modulators are composed of a multiple quantum well inserted between a p-type and n-type AlGaAs layer. The structures are grown on GaAs substrates. A schematic of the fabrication process is shown in figure 18. The first processing step is to define mesa diodes using a wet

etch. Ohmic contacts are then made to the p-type AlGaAs top surface through standard metal lift-off techniques. Next, the GaAs substrate is then lapped to approximately 100  $\mu\text{m}$ . A metal pattern is then defined on the backside of the substrate which acts as both an ohmic contact and an etch mask. A hole is etched through the backside of the substrate, stopping within the n-type AlGaAs epitaxial layer. The backside etch is accomplished with a modified jet etching instrument from South Bay Technology. The jet etcher provides a stream of  $\text{NH}_4\text{OH}:\text{H}_2\text{O}_2$  directed at the backside of the wafer while monitoring the transmission through the wafer. Once the instrument detects that the substrate has been removed, the etch is terminated. The etch rate of GaAs in  $\text{H}_4\text{OH}:\text{H}_2\text{O}$  is increased from 6  $\mu\text{m/hr}$  in magnetically stirred beaker to 80  $\mu\text{m/hr}$  with the jet etcher which results in a significant reduction of processing time. The selectivity between AlGaAs and GaAs etch rates is increased from 10:1 to 16:1 which allows for better control in stopping the etch at the beginning of the AlGaAs layer.

The transmission mode InGaAs/GaAs modulator fabrication proceeds in much the same way as the AlGaAs/GaAs modulator except the substrate thinning and etching is not required because the operating wavelength of the InGaAs/GaAs is not absorbed by the GaAs substrate. Likewise, the reflection mode devices only require simple processing since they are only optically addressed from the surface. For both the InGaAs/GaAs transmission modulators and the reflection modulators, the processing simply consists of defining mesa diodes through a wet chemical etch and then contacting the diodes through standard metallization techniques.

### 1.3.2. Spatial Light Modulator Performance

#### 1.3.2.1. Coupled Quantum Well Fabry-Perot Modulator

The electroabsorptive asymmetric Fabry-Perot (ASFP) optical modulator has recently received attention for its use in electrically-addressable spatial light intensity modulator arrays due to its potentially high contrast ratio, large reflectance difference and low drive voltage [51]. Most published results have been for modulators in which isolated rectangular quantum wells are used in the electrically-tunable absorbing region [52]. In an effort to improve performance, the electroabsorptive properties of new bandgap engineered materials are being explored. It has been suggested that symmetric coupled quantum wells (SCQW) would allow reduced drive voltage due to an absorption edge which is more sensitive to an applied electric field than that of the commonly used rectangular quantum well (RQW) [53]. However, rapid shifting of the absorption edge with field does not ensure better performance if this is combined with a significant weakening of the transitions causing the absorption. We report here the first systematic comparison of ASFP modulators based on SCQWs and RQWs.

To determine if the SCQW offers an improvement over the RQW, the two types of wells must be designed to allow modulation at the same wavelength. We have chosen to compare a 100 $\text{\AA}$  GaAs RQW with a 90 $\text{\AA}$  GaAs/15 $\text{\AA}$   $\text{Al}_{0.3}\text{Ga}_{0.7}\text{As}$ /90 $\text{\AA}$  GaAs SCQW, for which the longest wavelength peak in the absorption spectrum is at approximately 849 nm. First, the absorption coefficient,  $\alpha(F, \lambda)$ , of multiple quantum wells with 100 $\text{\AA}$   $\text{Al}_{0.3}\text{Ga}_{0.7}\text{As}$  barriers was measured as a function of wavelength and applied transverse electric field for both well types. Figures 19 and 20 show plots of this data for the RQW and SCQW respectively.

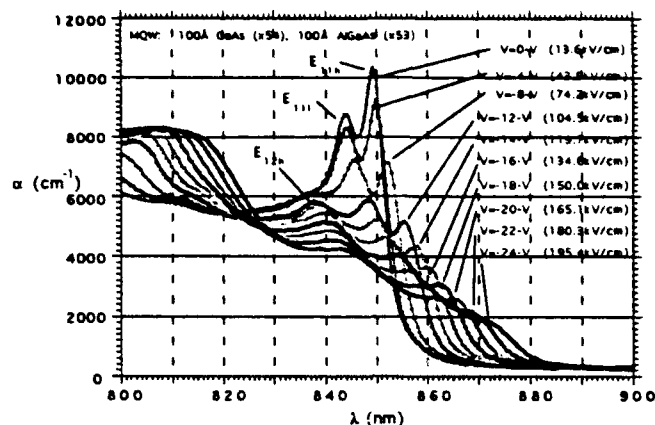


Figure 19. Absorption versus wavelength in the single rectangular quantum well.

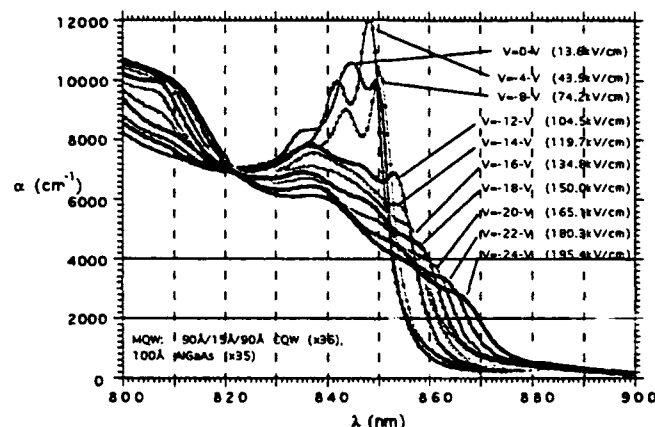


Figure 20. Absorption versus wavelength in the symmetric coupled quantum well.

The calculations made for similar coupled well systems [54, 55] are used to identify and qualitatively explain the behavior of the excitonic transitions with electric field for the SCQW data. At zero field, the lowest energy transition in the SCQW is the  $n=1$  electron to  $n=1$  heavy hole transition,  $E_{1hh}$ , as in the RQW case. When an electric field is applied, it shifts rapidly to longer wavelengths, but also loses strength rapidly as the transition becomes spatially indirect due to separation of electron and hole into different wells in the coupled well system [56]. On the other hand, transitions which were spatially indirect without field become direct with field and can increase in strength. The longest wavelength transition of this type is the  $n=1$  electron to  $n=2$  heavy hole,  $E_{12h}$ , which first increases in strength and blue shifts before exhibiting a shift to longer wavelength with loss of strength [55]. The  $n=2$  electron to  $n=1$  heavy hole,  $E_{21h}$ , also has this behavior, and it is these two transitions which dominate the change in absorption at wavelengths below the absorption edge. The net effect in comparison with the RQW is that the absorption edge of the SCQW moves less rapidly to longer wavelengths with increasing electric field, but retains greater absorption strength due to the spatially direct nature of the transitions. This can be seen by comparing the absorption as a function of electric field at a series of wavelengths below the absorption edge for the RQW, figure 21, and the SCQW, figure 22.

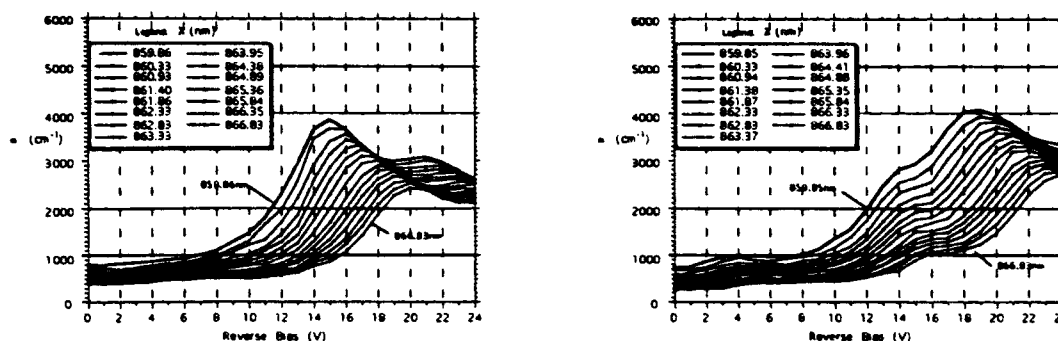
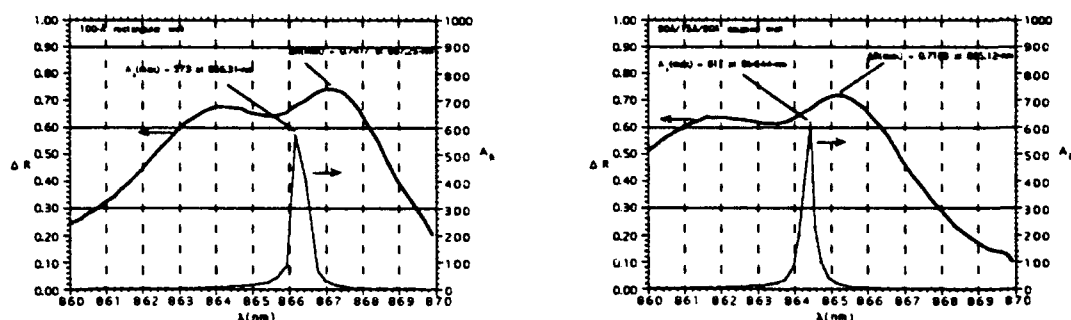


Figure 21 & 22. Absorption versus electric field for single rectangular quantum well (left) and symmetric coupled quantum well (right).

Modulation at wavelengths below the zero field absorption edge would require larger electric fields for the SCQW than the equivalent RQW, and this translates into greater drive voltage. This disadvantage could be offset, however, by the fact that the cavity of the SCQW modulator can be made shorter since there is a greater change in absorption coefficient. This reduces the drive voltage for a given electric field.

To assess the effect of this difference in electroabsorption behavior on performance, ASFP modulators employing the two well types were grown by molecular beam epitaxy. The devices were designed to be normally on for modulation at  $\lambda = 867\text{nm}$ . Distributed Bragg reflectors were grown for the top and bottom mirrors with design reflectances of 0.7 and 0.99 respectively. Of critical importance to performance is the wavelength separation,  $\Delta\lambda$ , between the zero field absorption edge and Fabry-Perot resonance [52]. The wavelength position of the Fabry-Perot resonance varies radially on the wafer due to radial variations in layer thickness, while there is little variation in the position of the absorption edge, so devices with a range of  $\Delta\lambda$ , are present on each sample. For the comparison, we present the performance of RQW and SCQW devices both having  $\Delta\lambda$ ,  $\sim 17\text{-}18\text{ nm}$ . The cavity lengths were chosen to be the minimum which still allows sufficient absorption to balance the mirrors and cause zero reflectance in the off state. Using the absorption data, the RQW modulator must have a cavity length of  $7420\text{ \AA}$ , while in the SCQW device it need be only  $6134\text{ \AA}$  due to the greater absorption change possible in the coupled well system. In both types of devices, there is a small mode pushing effect from electrorefraction [57] which causes the Fabry-Perot minimum to move to a longer wavelength in the off state. The turn off voltage of the RQW device is  $V_{\text{off}} = -14.9\text{ volts}$  compared to  $V_{\text{off}} = -15.6\text{ volts}$  for the SCQW. The shorter cavity of the SCQW modulator was thus insufficient to offset the smaller shift of the absorption edge. We conclude from the absorption data that this is due to the dominance of the  $E_{12h}$  and  $E_{21h}$  transitions which becomes so weak as to give a negligible contribution to any absorption change. Figures 23 and 24 show the reflectance difference,  $\Delta R = R_{\text{on}} - R_{\text{off}}$ , and contrast ratio,  $AR = R_{\text{on}}/R_{\text{off}}$ , as a function have a very high maximum  $AR \sim 600$  and large peak  $\Delta R \sim 0.72 - 0.74$ , indicating the high quality of the epitaxial growth. The high on state reflectance is a result of low residual absorption in the cavity at zero applied voltage. The very low off state reflectance of approximately 0.001 in both devices indicates that sufficient absorption is available in the cavity to balance the mirrors and that there is very little light scattering in the mirrors due to layer roughness. The insertion loss at peak  $\Delta R$  of 1 dB and 1.25 dB for the RQW and SCQW devices, respectively, is quite low. Thus, the two devices have approximately the same performance aside from the drive voltage.



Figures 23 & 24. Reflectance change and contrast ratio in the single rectangular quantum well(left) and symmetric coupled quantum well (right).

The SCQW does not appear to offer any advantage over the RQW for use in electroabsorptive modulators. The lowest energy transition, which shifts rapidly, becomes too weak in an applied field to play a role in modulation of the absorption coefficient below the zero field absorption edge. In general, the shift in wavelength, change in absorption strength and broadening in linewidth of several transitions all contribute to the change in absorption coefficient with field at a given wavelength. This work emphasizes the importance of (1) making measurements of the absorption coefficient as a function of wavelength and electric field and (2) comparing quantum wells with the same zero field wavelength in the search for materials with improved electroabsorptive properties.

### 1.3.2.2. High Contrast Ratio, Asymmetric FP Modulator

The surface-normal asymmetric Fabry-Perot structure has received much attention recently due to its high performance potential for two-dimensional arrays of electro-optic modulators [58] and self-electro-optic effect devices (SEEDs) [59]. The electroabsorptive asymmetric Fabry-Perot structure (ASFP) employs a cavity of electrically-controllable absorbing material situated between two dielectric quarter-wave mirrors having unequal reflectances. When the mirrors are balanced by effectively changing the bottom mirror reflectance through an increase or decrease in cavity absorption, it is possible in theory to obtain a zero off-state reflectance. The ratio of on-state reflectance to off-state reflectance, the contrast ratio, is one important measure of performance in these devices and, theoretically, this should be infinity due to the zero off-state reflectance. In practice, however, values of zero for the off-state reflectance have not been obtained. This can be caused by the method used to measure the reflectance [60], insufficient cavity absorption to balance the mirrors [61], or imperfections in the epitaxial layers which scatter light in the off state. In this letter, we report performance results on an ASFP modulator in which a sensitive measurement set up is used to measure reflectance, sufficient absorption is designed into the cavity to allow complete turn-off, and a superlattice alloy is used to reduce microroughness in the mirrors.

The device structure, grown by molecular beam epitaxy (MBE), consists of a 19.5 period quarter-wave mirror on the bottom, a multiple rectangular quantum well (MQW) of  $37 \times 100$  Å GaAs and  $36 \times 100$  Å  $\text{Al}_{0.3}\text{Ga}_{0.7}\text{As}$ , and a 4 period top mirror. The cavity length,  $L = 7420$  Å, is designed to place the Fabry-Perot mode at 867 nm. Each mirror period is composed of 728 Å AlAs and a superlattice alloy of  $13.1$  Å GaAs/  $26.2$  Å  $\text{Al}_{0.3}\text{Ga}_{0.7}\text{As}$ , used to approximate an average aluminum mole fraction in the high-index quarter-wave layer of 0.2. Sixteen periods of the superlattice are required to comprise the 628 Å-thick equivalent  $\text{Al}_{0.2}\text{Ga}_{0.8}\text{As}$  layer. The calculated reflectances at 867 nm, as viewed from within the cavity, are  $R_B = 0.99$  for the bottom mirror and  $R_T = 0.70$  for the top mirror. The use of a superlattice in the mirrors is expected to have many beneficial effects. A superlattice buffer has been shown to reduce interface roughness and impurities in layers grown above it [62]. GaAs smoothing monolayers have also been incorporated at intervals in mirror AlAs layers to reduce interface roughness [63]. Other advantages are an improvement in quantum well properties and the fact that only one aluminum effusion cell is needed for different mole fractions in the mirror and multiple quantum well barriers. A 20-period test mirror, similar to the bottom mirror used in the devices, was grown on an n-GaAs substrate and the measured

peak reflectance,  $0.996 \pm 0.01$ , compared to the calculated value of 0.997, indicated that near-ideal mirrors can be grown by this technique.

To properly design the device, the absorption coefficient of the MQW was first measured as a function of electric field and wavelength on a test structure. The zero-field heavy hole exciton peak is at 850 nm with an absorption coefficient of  $\alpha = 10,150 \text{ cm}^{-1}$ . A normally on device was desired, so the Fabry-Perot mode is placed at a longer wavelength with a wavelength separation from the heavy hole peak of  $\Delta\lambda$ . The reduction in absorption coefficient becomes very gradual above 867 nm where the value measured is  $200 \text{ cm}^{-1}$ . Little increase in on state reflectance but a substantial increase in turn off voltage occurs beyond this point, so 867 nm is chosen as the longest desirable operating wavelength and Fabry-Perot mode position, making  $\Delta\lambda = 17 \text{ nm}$ . Careful cavity design will ensure that the device can be turned off completely. Its length was chosen to be the minimum possible to place the Fabry-Perot mode at the operating wavelength and still allow sufficient absorption to cause zero reflectance to be obtained in the off state. Possible cavity lengths,  $L$ , are given by

$$L = p\lambda_0/2n_c \quad (1)$$

where  $p = 1, 2, 3, \dots$  is the mode index,  $\lambda_0$  is the wavelength of the Fabry-Perot mode, and  $n_c$  is the refractive index of the cavity. The cavity length-absorption product required to cause the reflectance at the Fabry-Perot mode to go to zero,  $(\alpha L)_0$ , is given by [66]

$$(\alpha L)_0 = -1/2 \ln (R_T/R_B) \quad (2)$$

where  $\alpha$  is the absorption coefficient in the cavity,  $R_T$  is the top mirror reflectance and  $R_B$  is the bottom mirror reflectance. For the designed mirror reflectances,  $(\alpha L)_0 = 0.1733$ . The absorption coefficient was found to have a maximum of  $\alpha_{\max} = 2423 \text{ cm}^{-1}$  at 867 nm, occurring at an applied field of 139 kV/cm. The minimum possible cavity length for this value of absorption is then 7153 Å, but from (1) with  $n_c = 3.5054$ , the closest allowed value larger than this is 7420 Å. An appropriate average of the refractive indices of bulk GaAs and  $\text{Al}_{0.3}\text{Ga}_{0.7}\text{As}$  which make up the cavity was used to estimate the value of  $n_c$ . The sample was rotated during growth and, due to nonuniformities in the arrival rates of Ga and Al, there was a radial variation of layer thicknesses and, consequently, a radial variation in the Fabry-Perot mode wavelength position. Several devices at different radial positions were tested and the Fabry-Perot mode wavelength with zero applied voltage ranged from 866.83 nm at the center to 851.38 nm at the edge of the 2" wafer. The corresponding range of cavity thickness is from 7420 Å to 7286 Å, a variation of 1.8 %, indicating the sensitivity of mode placement to nonuniformities in the growth. The absorption edge of the MQW, determined primarily by the quantum well width, is not shifted very much by this variation in thickness, however. The result is that  $\Delta\lambda$  decreases from the center toward the edge of the wafer. All devices with Fabry-Perot mode wavelengths greater than 858 nm had contrast ratios greater than 400. Below this wavelength, the on state reflectance decreases quickly due to the rapidly increasing residual absorption at zero bias, which degrades the contrast ratio. Shown here is the performance of the device with the highest contrast ratio, 1090, which has its Fabry-Perot mode at 858.40 nm in the on state (zero volts applied). Although devices with Fabry-Perot modes at even longer wavelengths had higher on state reflectances due to the slowly decreasing residual absorption with wavelength, their contrast ratios were not as large (between 400 and 800) because their off state reflectance values were not as low even though there is sufficient cavity absorption to theoretically bring the reflectance to zero. The off state reflectance of these devices was in the range of 0.00075 to 0.001 compared to approximately 0.0005 for the best device. We believe that, due to the variation of beam fluxes as well as substrate temperature radially on the wafer, there may be some optimum occurring at this position for which microroughness causing scattered light is minimized.

The reflectance spectra of the device at several applied reverse biases is shown in figure 25.

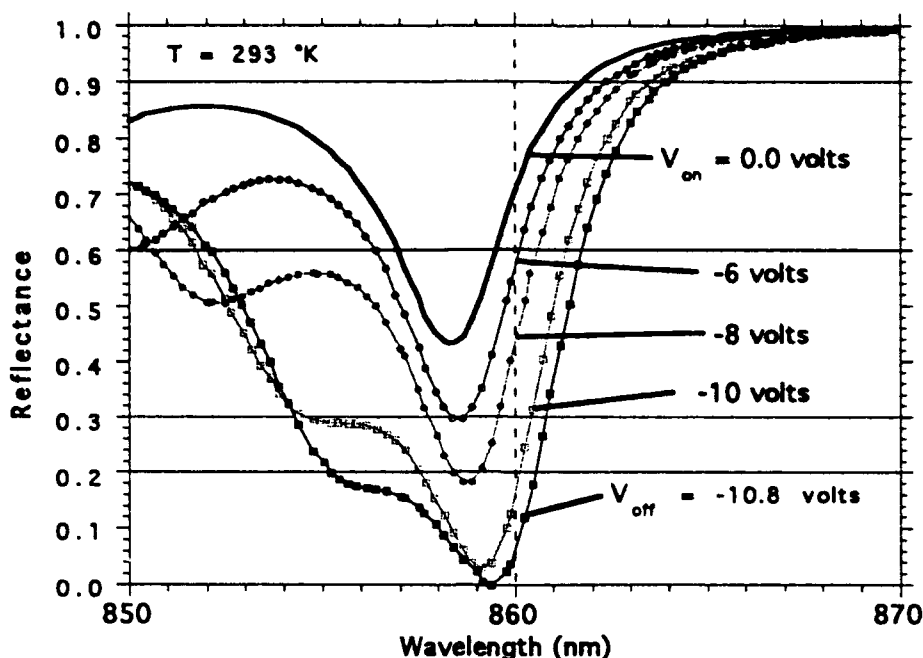


Figure 25. Modulator reflectance spectra at applied reverse bias voltages of 0, -6, -8, -10, and -10.8 volts. The shift of the Fabry-Perot minimum to longer wavelengths with increasing bias and the very low off state reflectance can be seen.

The Fabry-Perot minimum at 0.0 volts is at 858.40 nm with a reflectance of 0.4307 and moves to 859.40 nm at -10.8 volts due to electrorefraction. This effectively increases the on state reflectance since the operating wavelength at the off state minimum is now displaced from the on state reflectance minimum. At 859.40 nm, the 0.0 volt reflectance is 0.57 and the off state reflectance is 0.000523, giving a contrast ratio of 1090. There is, however, a large uncertainty in this value due to uncertainty in the low value of reflectance. The measurement set up is similar to that described in [64], and in a previous section. In the scheme used here, the uncertainty in the low value of reflectance is calculated to be  $\pm 0.0005$ , giving a range for the low reflectance value of 0.0000 to 0.0010 and a corresponding range of 570 to near infinity for the contrast ratio.

To further test the high value of contrast ratio, an independent measure of the ratio of optical powers reflected from the device in the on and off states at 859.40 nm was made. The measured values of optical power reflected from the device in the on and off states were 1.098  $\mu\text{W}$  and 3.340 nW, respectively, with a background level of 2.045 nW when the device was blocked. Each of these were averaged from 4000 measured data points to reduce noise to  $\pm 5\%$ . Subtracting the background from the on and off state reflected powers and taking the ratio results in a contrast ratio of 846. The noise in the measurement of optical powers leads to a worst case range of contrast ratio of 667 to 1124. This is taken as a confirmation that the contrast ratio as measured by reflectance is not in error by a large amount. The highest contrast ratio in a similar device, to our knowledge, was reported to be "greater than 100:1" [65]. A plot of contrast ratio versus wavelength in [65] peaked at a value of approximately 26 dB (400), although the uncertainty in the measured values was not given.

The contrast ratio was measured as a function of wavelength and voltage. Figure 26 shows a plot of the device reflectance and contrast ratio as a function of applied voltage at an operating wavelength of 859.40 nm.



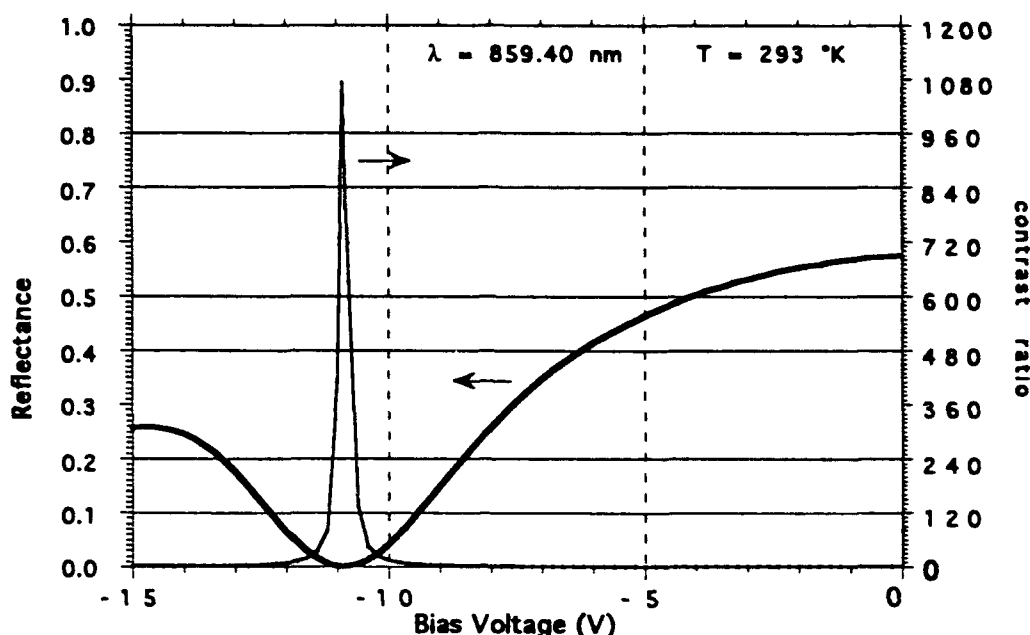


Figure 26 Modulator reflectance and contrast ratio as a function of applied reverse bias at an operating wavelength of 859.40 nm.

The peak in contrast ratio occurs at  $V_{\text{off}} = -10.8$  volts and remains above 10 (10 dB) over a range of 2.2 volts and above 100 (20 dB) over a range of 0.6 volts. The contrast ratio remains above 10 over a range of 1.5 nm and above 100 over a range of 0.5 nm. Due to the complex shape of the on and off state reflectance-wavelength curves, the peak reflectance difference occurs at a slightly longer wavelength than that of the peak contrast ratio, suggesting two different optimum operating points dependent upon the optical system employing the device. The reflectance difference has a maximum of 0.643 and remains above half of this value over a range of 9 nm, giving a much wider optical bandwidth than that of the contrast ratio. The insertion loss at the maximum in contrast ratio is 2.4 dB, while at the maximum in reflectance difference it is 1.7 dB.

In conclusion, a very high-quality normally-on asymmetric Fabry-Perot reflection modulator with a contrast ratio of  $> 1000:1$ , as measured by reflectance, has been demonstrated. The contrast ratio is, to our knowledge, the largest reported to date. An independent determination of contrast ratio by optical power measurement gave a value of 846 with a range of uncertainty which includes the value measured by reflectance. The device uses superlattice regions for the high-index layers of the quarter-wave mirrors, which may reduce microroughness in the MBE-grown material. The cavity was carefully designed, using measured absorption data, to allow sufficient absorption to turn the device off, while minimizing cavity length. A sensitive measurement set up for reflectance allowed reduced noise and background light effects which can limit the measurement of low values of reflectance.

### 1.3.2.3. Novel Bistable MQW Electro-optic Phase Modulator

In this section, we discuss the novel integration of a SEED and a waveguide modulator [67]. This is an extension of the modulator concepts presented earlier in this report. The inherent electrical bistability of the SEED [68] with input optical power is used to control the electric field across an electro-optic waveguide modulator to produce optical bistability. This concept is used to demonstrate the control of a light beam of one wavelength ( $1.152\mu\text{m}$ ) with a light signal at another wavelength ( $0.848\mu\text{m}$ ). Additionally, light incident in a direction perpendicular to the plane of the substrate at one wavelength is

used to switch light propagating in the plane of the substrate. This scheme is compatible with optical interconnects and optical computing [70].

A GaAs/AlGaAs MQW (45 periods of 100Å GaAs wells and 100Å Al<sub>0.3</sub>Ga<sub>0.7</sub>As barriers) "detector" (SEED) was designed for room temperature operation at 0.848μm. The bias voltage  $V$  and the feedback load resistance required for the detector to exhibit electrical bistability were calculated from photocurrent measurements made on the detector. A ridge waveguide modulator in parallel with the SEED was designed to operate at 1.152μm (helium neon laser line). The waveguide was designed for single mode operation by using an effective index approximation [71]. At  $\lambda=1.152\mu\text{m}$ , waveguide modulation is predominantly due to the linear electro-optic effect, so a field-induced change in the real part of the refractive index results in a sinusoidal change in output light intensity versus applied voltage. The input ( $I_0$ ) and output ( $I$ ) light intensities are related by,

$$I = I_0 \sin^2(\phi/2).$$

where the phase change  $\phi$  is a function of the electro-optic coefficient of the material, interaction length and an applied voltage across the device. The half wave voltage  $V_\pi$ , is defined as the bias voltage required to perform one complete on/off cycle in the waveguide modulator. The length of the waveguide modulator is chosen to obtain a magnitude of  $V_\pi = V_b$ , where  $V_b$  is the electrical bistability voltage produced from the SEED. Thus, the electrically bistable region of the SEED is matched to the voltage required for the waveguide modulator to traverse one complete on/off cycle. Optical power incident on the SEED controls the output light intensity (and bistability) of the waveguide modulator. The geometry of the integrated SEED and waveguide is shown in figure 27.

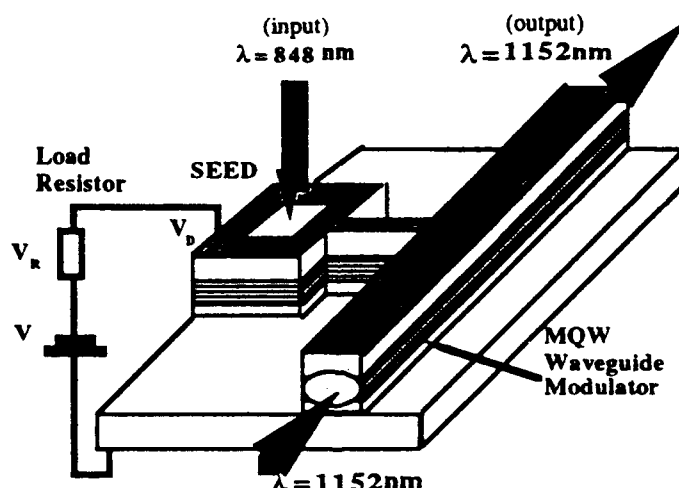


Figure 27. Schematic of the combination of a SEED and a waveguide electro-optic modulator used to demonstrate optical bistability.

The shift in the peak absorption energy of the SEED versus electric field is due to the quantum confined Stark effect as discussed previously. The maximum change in responsivity was measured at the operating wavelength of 0.848μm. From the responsivity curves, load lines were chosen for different resistance values to determine regions of electrical bistability. Electrical bistability was the greatest with -35V across the series combination of the device and a 500 K Ω load resistance. Bistability was observed at an incident power of 325μW with switching voltages across the detector at  $V_l = -8.5\text{V}$  and  $V_h = -16\text{V}$  for the up and down transitions respectively. These switching voltages were used to design the length of the waveguide modulator.

Amplitude modulation for the MQW waveguide modulator was produced by the phase difference method, using a polarizer rotated 45 degrees to the surface normal and an analyzer cross polarized to the direction of the polarizer. Light from a He-Ne laser at 1.152μm was focused onto the cleaved edge of the waveguide by means of a 40x micro-objective lens. The transfer function of the modulated light for various waveguide lengths was calculated and the waveguide modulator length chosen to demonstrate on/off switching in the bistability region determined earlier from the SEED.

Figure 28 shows the measured optical bistability from the 2.8mm long waveguide modulator for a load resistance of 500K  $\Omega$  and a bias voltage of -35V.

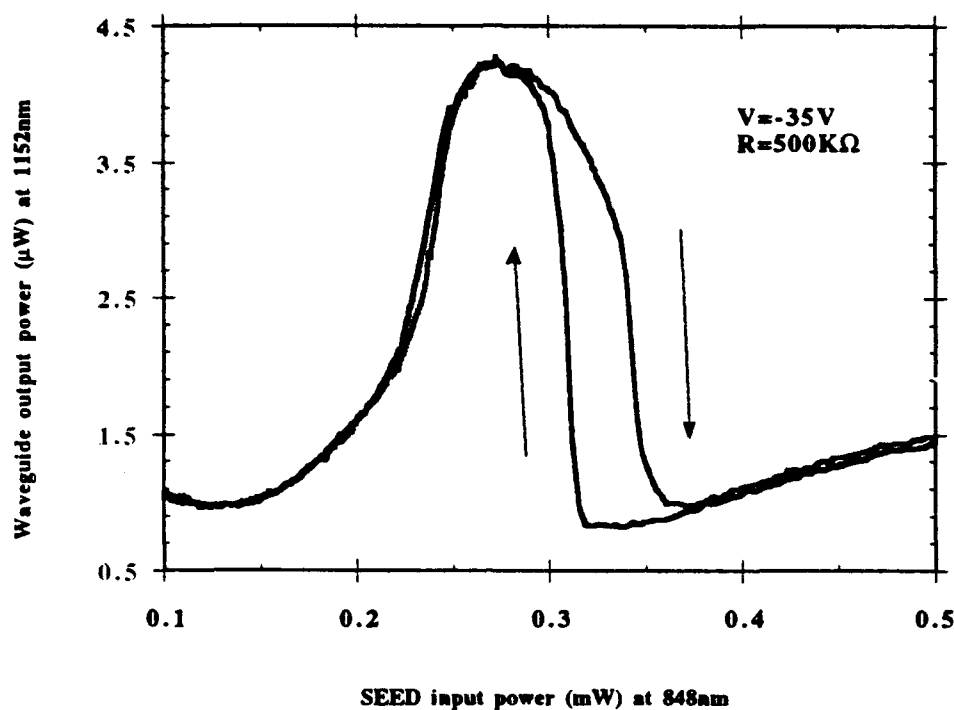


Figure 28. The measured optical bistability for a waveguide modulator of length 2.75 mm operating at 1.152 $\mu$ m. The SEED is operating at 0.848 $\mu$ m, with -35V bias voltage and a 500 K  $\Omega$  series resistance. The arrows indicate the increasing and decreasing directions of incident power.

Sinusoidal behavior of the phase modulator is clearly seen with the optical bistability superimposed. The product of  $V_{\pi}$  and the modulation length for the waveguide modulator was determined to be 31 V-mm. This required a voltage change from -7V to -18V for one complete on/off cycle. As the power of the 0.848 $\mu$ m light increased, the bias voltage across the modulator ( $V_D$ ) increased. At approximately 325 $\mu$ W of incident power, corresponding to SEED bistability voltages of -8.5V and -16V, optical bistability results. The arrows indicate increasing and decreasing directions of the control light power. Thus, the change in 0.848 $\mu$ m light power, incident normal to the surface produces a phase change in the 1.152 $\mu$ m wave propagating through the waveguide and appears as an optically bistable intensity signal normal to the control beam direction.

This is the first demonstration of optical phase bistability from a MQW waveguide structure using the feedback property of a SEED. This demonstrates switching light of one wavelength by another wavelength propagating in an orthogonal direction. An extension of this configuration is to incorporate the structure into a Mach Zehnder interferometer for larger intensity modulation. This device can also be used as an intermediate device to transfer signals between planar type of optical integrated circuit (OEIC) and vertical optical processing type devices such as vertical cavity surface emitting lasers and spatial light modulators.

## 1.4. Lasers

### 1.4.1. ATOW Vertical Cavity Surface Emitting Laser (VCSEL)

A variety of optical architectures and signal processing applications could be realized with a two-dimensional array of vertical cavity surface emitting lasers (VCSELs) coupled to a two-dimensional array of spatial light modulators. One area of interest is in the growth of InGaAs VCSELs which are of particular interest because of their emission at energies below the band gap of GaAs. This allows the coupling of AlGaAs/GaAs transmission modulators without removal of the modulators' substrate which simplifies the modulator fabrication.

The design of an InGaAs/GaAs VCSEL has been studied using the Schrödinger-Poisson solver. Current injection has also been included to simulate laser devices. The computer simulation allows optimization of the device design prior to material growth and fabrication. The Schrödinger-Poisson solver was used to calculate gain profiles as a function of wavelength and doping concentrations. The laser threshold current density was also computed for a variety of structures.

Development of a fabrication process for VCSELs has resulted in the master's thesis of J. P. D. Suryanata as well as collaborations with Motorola in Tempe, Arizona. The results of this work have achieved a record (at the time of fabrication) low threshold current density for a VCSEL of  $487 \text{ A/cm}^2$  in continuous wave, room temperature operation. The low threshold current is attributed to the optimization of the compositional grading and the high optical efficiency of the InGaAs grown at ASU.

#### 1.4.2. InGaAs/GaAs/AlGaAs ATQW Lasers

An extension of the triangular well concept was the realization of ATQW edge-emitting lasers [72]. Broad area MBE grown lasers using strained  $\text{In}_{0.25}\text{Ga}_{0.75}\text{As}$  asymmetric triangular quantum well (ATQW) active regions were realized for the first time. Recently, it has been demonstrated theoretically that non-rectangular quantum well profiles may offer an increase in diode laser gain [73]. Furthermore Yoo et. al. has shown that low threshold current densities are achievable using a  $70 \text{ \AA}$  symmetric triangular quantum well using the alternative analog grading technique [74]. Motivated by the possibility of enhanced gain and the ability to increase QW design abilities, we show preliminary device performances of strained Asymmetric Triangular Quantum Wells (ATQWs) using AlGaAs/ GaAs/ InGaAs.

Laser material was grown using  $\text{In}_{0.095}\text{Ga}_{0.905}\text{As}$  ATQWs as active regions. Photoluminescence (PL) spectra taken on  $200 \text{ \AA}$ ,  $400 \text{ \AA}$  and  $600 \text{ \AA}$  wells with GaAs barriers exhibited a  $1.8 \text{ K}$  PL line width of  $0.6 \text{ meV}$  for the  $400 \text{ \AA}$  well and  $0.8 \text{ meV}$  and  $1.2 \text{ meV}$  line widths for the  $600 \text{ \AA}$  and  $200 \text{ \AA}$  respectively. confirmed this [75]. A comparison with an  $80 \text{ \AA}$  rectangular quantum well of similar composition was made.

Each MBE grown laser employed a graded index separate confinement heterostructure (GRINSCH). The composition profile is shown in figure 29. To minimize possible growth environment variations, all devices were grown consecutively. The ATQWs were grown using the digital composition grading technique using a cell width of  $25 \text{ \AA}$ . Within each cell, the composition consists of one layer each of  $\text{In}_{0.25}\text{Ga}_{0.75}\text{As}$  and GaAs. The varying proportions of thickness within each cell across the well yields a linear grade from  $x = 0.25 \text{ In}$  to  $x = 0.0\% \text{ In}$ . The bottom of the well defines the well composition, in this case,  $x = 0.25$ . Each QW was surrounded by  $75 \text{ \AA}$  thick GaAs barrier layers and  $2000 \text{ \AA}$  AlGaAs GRIN layers where the AlAs mole fraction was graded linearly between 5 and 60%. The  $\text{Al}_{0.6}\text{Ga}_{0.4}\text{As}$  upper and lower cladding layers were  $0.75 \text{ \mu m}$  and  $1.0 \text{ \mu m}$  thick respectively. Correspondingly, the measured electrolytic C-V doping levels in the cladding layers were  $p = 3.0 \times 10^{17} \text{ cm}^{-3}$  and  $n = 1.5 \times 10^{17} \text{ cm}^{-3}$ . A top GaAs contact layer ( $p = 2.0 \times 10^{19} \text{ cm}^{-3}$ )  $0.15 \text{ \mu m}$  thick was grown for electrical contact. The entire structure was grown on an  $n^+$  GaAs (100) substrate with a  $0.5 \text{ \mu m}$   $n^+$  GaAs buffer and a five period ( $100 \text{ \AA}$  GaAs/  $100 \text{ \AA}$   $\text{Al}_{0.6}\text{Ga}_{0.4}\text{As}$ ) superlattice buffer. A pyrometer growth temperature of  $\sim 710^\circ\text{C}$  was used for the cladding layers while the active region was grown at  $\sim 510^\circ\text{C}$ . A 30 second growth interrupt was used during each GaAs bounding layer to allow for substrate temperature adjustment.

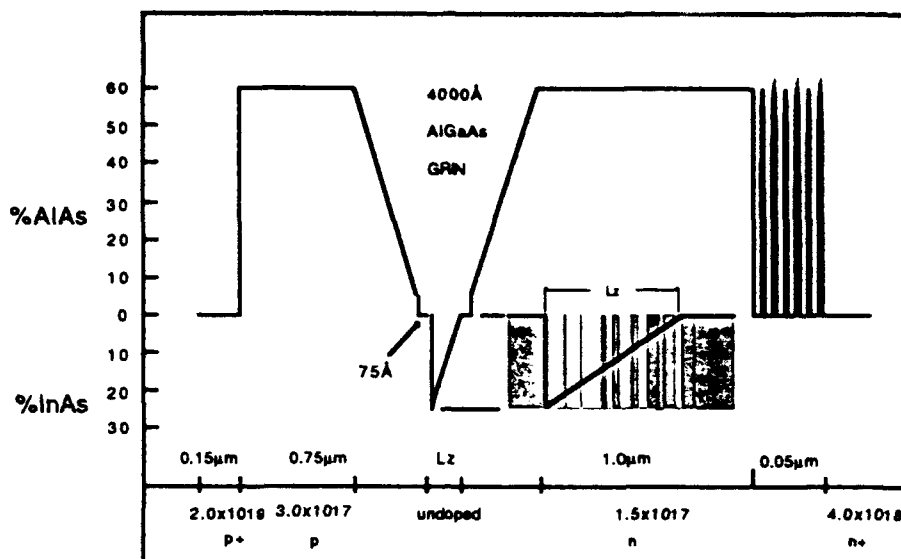


Figure 29. The composition profile and orientation of the ATQW GRINSCH laser. The material surrounding the active region is identical for the 80 Å rectangular well.

Gain-guided, 100 μm, broad area lasers were fabricated using standard procedures and tested under pulsed (200 ns pulse width at 1.0 kHz) conditions to eliminate thermal effects. The uncoated facet mirror reflectivity was taken to be 0.30. A value for the optical confinement factor,  $\Gamma$ , was calculated using index of refraction data for each laser at its specific wavelength and an *effective* well width ( $L_{eff} < L_z$ ) where  $L_z$  is the metallurgical width. The effective well width is defined by the spatial extent of the optical gain region within the well. The physical asymmetry of the well creates a compositionally induced electric field where electrons and holes are forced to assume a non uniform asymmetric distribution; to use the full metallurgical well width would yield a significant over estimation of the optical confinement factor. For simplicity the value for  $L_{eff}$  was defined as the full width at 10% of the product  $\Psi_{C1} \cdot \Psi_{HH1}^*$  where  $\Psi_{C1}$  is the  $n = 1$  conduction band envelope function and  $\Psi_{HH1}^*$  is the  $n = 1$  heavy hole envelope function conjugate. The 10% of full width value of the product  $\Psi_{C1} \cdot \Psi_{HH1}^*$  was chosen for  $L_{eff}$  by comparing this product to  $L_z$  for several different RQW widths. The calculated effective well widths were 98 Å, 118 Å and 138 Å for the 200 Å, 300 Å and 400 Å wells respectively. A more exact treatment may be found by adopting the formalism of Aversa and Iizuka [76].

The cavity length dependence of wavelength,  $\lambda$ , differential quantum efficiency  $\eta_d$ , threshold current density  $J_{th}$  and threshold current  $i_{th}$  were measured for each structure. The results shown in figure 30 indicate the high quality of the lasers. The lowest threshold current density (112 A/cm<sup>2</sup>, 820 μm cavity length) was achieved by the narrow RQW. However, the differential quantum efficiency of 35% was low with a higher than normal internal loss of 19 cm<sup>-1</sup>. These values may in part be explained by loss due to the observed Be diffusion (electrolytic C-V) into the active region. The 300 Å well showed the lowest threshold current density of the ATQWs at 152 A/cm<sup>2</sup> and a high external differential quantum efficiency of 60.3%.

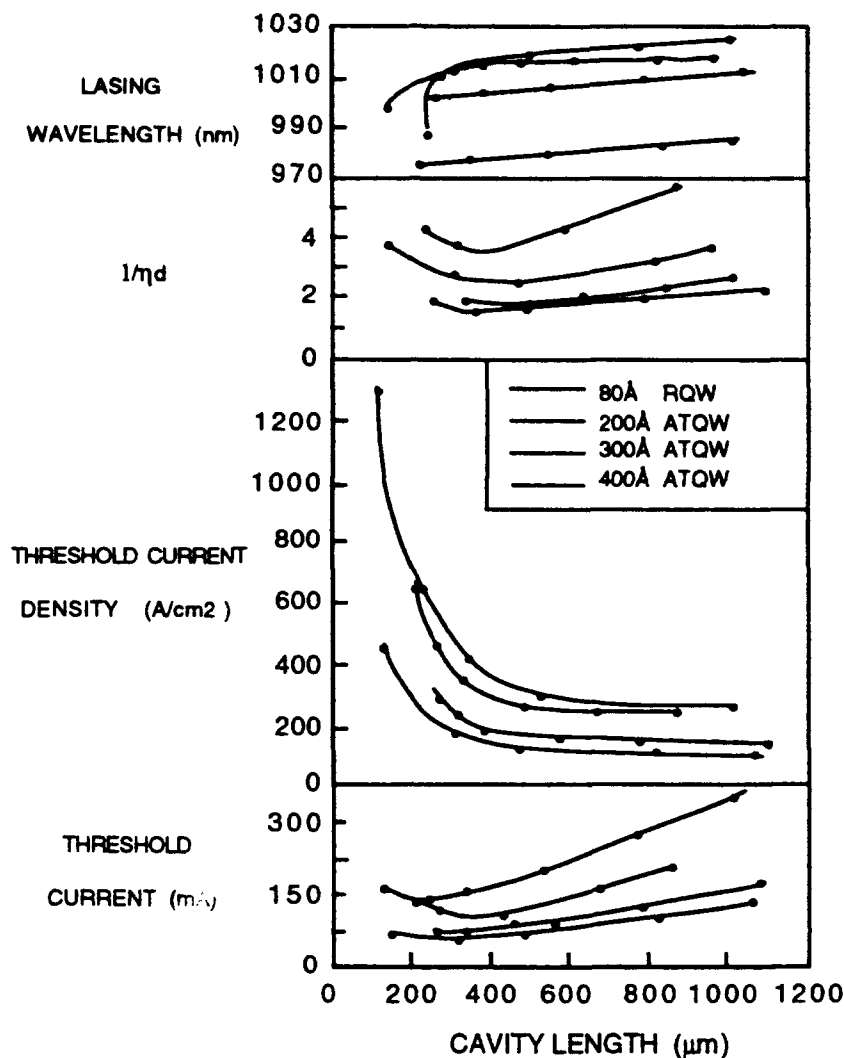


Figure 30. The average measured values of lasing wavelength, reciprocal quantum efficiency, threshold current density and threshold current as a function of cavity length for each well dimension and shape.

For short cavities, all devices measured follow the predicted increase in threshold current with decreasing length. This is due to high injection effects such as Auger recombination, carrier leakage out of the quantum well and sublinear gain [77]. As expected, the onset of this high current regime occurs at different cavity length values for each well dimension. In the long cavity length regime, the threshold current also rises. Fundamentally, this is due to an increase in cavity volume which requires an increase in carrier number to achieve the inversion density. In addition, with increasing cavity length, the interaction length with interface recombination centers increases. The interface recombination velocity,  $v_s$ , phenomenologically describes a component of the threshold current due to interface recombination and critically depends on growth conditions [78]. An increase in  $v_s$  tends to increase the slope of the  $i_{th}$  versus cavity length curve as more carriers are increasingly lost to interface recombination. Although there is a spread in the data, the similar dependence of  $i_{th}$  on  $L$  for the 300 Å well compared to the RQW indicates that the increased number of interfaces in the digitally grown well does not necessarily imply an increase in interface recombination current.

From the wavelength dependence on cavity length in figure 30, it is seen that  $\lambda$  varies more in the ATQW towards long cavities over its RQW counterpart. However, in the short cavity length regime, dependence of the threshold lasing wavelength for strained ATQW is decreased over what is observed in the RQW laser. It is well known that a continuous decrease in wavelength with increasing carrier density (shorter cavity lengths) is a result of band filling. Typically, the dependence of wavelength on cavity

length is enhanced in  $\text{In}_x\text{Ga}_{1-x}\text{As}$  over GaAs lasers due to the reduced valence band density of states. The ATQW is attributed by a reduced dependence on band filling as carriers under high injection conditions are given freedom to disperse laterally, albeit against the electric field for one carrier type, in the wider wells.

A lasing transition switch from  $n = 1$  to  $n = 2$  states in the 400 Å well was observed. The difference in energy between the  $n = 1$  and  $n = 2$  transition energies were calculated using a Fourier Transform method on the components in the BenDaniel-Duke Hamiltonian (no compensation was made for bandgap renormalization) [79]. As was expected, the wavelength switch took place with decreasing cavity length in the structure with the smallest energy difference between the  $n = 1$  and  $n = 2$  states. The calculated difference in wavelength for the 400 Å well was 38.9 nm while the measured wavelength difference was 33.5 nm. The 38.9 nm is approximately one third the difference for the 80 Å RQW where  $C_1\text{-HH}_1 - C_2\text{-HH}_2$  is 103.6 nm for the calculated values. The wider the well, the smaller the difference in energy between the quantized state levels. The ATQW more readily provides second quantized state lasing in  $\text{In}_x\text{Ga}_{1-x}\text{As}$  lasers by allowing the growth of wider quantum wells. Lasing in the second quantized state results in a recovery of the differential gain. This has implications in lasers that are designed to operate at high modulation rates [80]. The actual lasing wavelength increase with increased well width nearly corresponds to our predicted transition energies.

The operating characteristics of  $\text{In}_{0.25}\text{Ga}_{0.75}\text{As}$  ATQWs with three different quantum well widths (200Å, 300Å and 400Å) were discussed for the first time and compared against an 80 Å RQW. Of the three ATQW, the intermediate 300Å well displayed the lowest threshold of 152 A/cm<sup>2</sup> current with a differential quantum efficiency of 61%. Second quantized state lasing in  $\text{In}_x\text{Ga}_{1-x}\text{As}$  was also reported.

## 1.5. References

- [1] D.L. Mathine, G.N. Maracas, D.S. Gerber, R. Droopad, R.J. Graham, M.R. McCartney and D.J. Smith, "Characterization of an AlGaAs/GaAs Asymmetric Triangular Quantum Well Grown By a Digital Alloy Approximation," submitted to J. Appl. Phys.
- [2] D.L. Mathine, S. Krishnan and G.N. Maracas, "A Computational Fourier Series Solution of the BenDaniel-Duke Hamiltonian for Arbitrary Shaped Quantum Wells," submitted to Phys. Rev. B
- [3] D. J. BenDaniel and C. B. Duke, *Phys. Rev.* **152** 683 (1966).
- [4] R. Droopad, R. A. Puechner, K. Y. Choi, K. T. Shiralagi, and G. N. Maracas, *J. Crystal Growth* **114** 327 (1991).
- [5] D. Gerber, R. Droopad, and G. N. Maracas, to appear in *Appl. Phys. Lett.*, Feb 1993.
- [6] G. Livescu, G. D. Boyd, R. A. Morgan, L. M. F. Chirovsky, A. M. Fox, R. E. Leibenguth, M. T. Asom, and M. W. Focht, "Role of Electrorefraction in Quantum Well Fabry-Perot Modulators," *Appl. Phys. Lett.*, vol. 60, pp. 1418-1420, 1992.
- [7] D.S. Gerber and G.N. Maracas, "A Simple Method for Extraction of Multiple Quantum Well Absorption Coefficient from Reflectance and Transmittance Measurements," to appear in *J. Quantum Electronics* 1993
- [8] D. E. Aspnes and A. A. Studna, "Dielectric Functions and Optical Parameters of Si, Ge, GaP, GaAs, GaSb, InP, InAs, and InSb from 1.5 to 6.0 eV," *Phys. Rev. B*, vol. 27, pp. 985-1009, 1983.
- [9] A. M. Fox, D. A. B. Miller, G. Livescu, J. E. Cunningham, and W. Y. Jan, "Quantum Well Carrier Sweep Out: Relatino to Electroabsorption and Exciton Saturation," *JEEE J.. Qunatum Electron.*, vol. 27, pp. 2281-2295, 1991.
- [10] M. D. Sturge, "Optical Absorption of Gallium Arsenide Between 0.6 and 2.75 eV," *Phys. Rev.*, vol. 127, pp. 768-773, 1962.
- [11] H. C. Casey, D. D. Sell, and K. W. Wecht, "Concentration Dependence of the Absorption Coefficient for n- and p-type GaAs Between 1.3 and 1.6 eV," *J. Appl. Phys.*, vol. 46, pp. 250-257, 1975.
- [12] W. T. Masselink, P. J. Pearah, J. Klem, C. K. Peng, H. Morkoc, G. D. Sanders, and Y. C. Chang, "Absorption Coefficients and Exciton Oscillator Strengths in AlGaAs-GaAs Superlattices," *Phys. Rev. B*, vol. 32, pp. 8027-8034, 1985.
- [13] J. Filipowicz, C. Ghezzi, and L. Tarricone, "Temperature Dependence of Optical Absorption Induced by Exciton Resonances in GaAs/GaAlAs Multi-quantum-well Structures," *Solid State Commun.*, vol. 74, pp. 533-538, 1990.

- [14] C. Ghezzi, D. Martin, A. Parisini, J. L. Staehli, and L. Tarricone, "Investigation of (AlGa)As/GaAs Quantum Wells by Optical and Phototransport Measurements," *Phys. Stat. Solidi (b)*, vol. 152, pp. 101-109, 1989.
- [15] H. Iwamura, T. Saku, and H. Okamoto, "Optical Absorption Coefficient of GaAs-AlGaAs Superlattice under Electric Field," *Japan J. Appl. Phys.*, vol. 24, pp. 104-105, 1985.
- [16] R. A. Logan and F. K. Reinhart, "Optical Waveguides in GaAs-AlGaAs Epitaxial Layers," *J. Appl. Phys.*, vol. 44, pp. 4172-4176, 1973.
- [17] C. Juang, J. Kuhn, and R. B. Darling, "Selective Etching of GaAs and  $\text{Al}_{0.3}\text{Ga}_{0.7}\text{As}$  with Citric Acid/Hydrogen Peroxide Solutions," *J. Vac. Sci. Tech B*, vol. 8, pp. 1122-1124, 1990.
- [18] D. D. Sell, H. C. Casey, and K. W. Wecht, "Concentration Dependence of the Refractive Index for n- and p-type GaAs Between 1.2 and 1.8 eV," *J. Appl. Phys.*, vol. 45, pp. 2650-2657, 1974.
- [19] H. C. Casey, D. D. Sell, and M. B. Panish, "Refractive Index of  $\text{Al}_x\text{Ga}_{1-x}\text{As}$  Between 1.2 and 1.8 eV," *Appl. Phys. Lett.*, vol. 24, pp. 63-65, 1974.
- [20] D. E. Aspnes, S. M. Kelso, R. A. Logan, and R. Bhat, "Optical Properties of  $\text{Al}_x\text{Ga}_{1-x}\text{As}$ ," *J. Appl. Phys.*, vol. 60, pp. 754-767, 1986.
- [21] J. J. LePore, "An Improved Technique for Selective Etching of GaAs and  $\text{Al}_x\text{Ga}_{1-x}\text{As}$ ," *J. Appl. Phys.*, vol. 51, pp. 6441-6442, 1980.
- [22] J. L. Jewel, H. M. Gibbs, A. C. Gossard, A. Passner, and W. Wiegmann, "Fabrication of GaAs Bistable Optical Devices," *Materials Lett.*, vol. 1, pp. 148-151, 1983.
- [23] J. M. Dell, M. J. Joyce, B. F. Usher, G. W. Yoffe, and P. C. Kemeny, "Unusually Strong Excitonic Absorption in Molecular-Beam-Epitaxy-Grown, Chemically Lifted GaAs Thin Films," *Phys. Rev. B*, vol. 42, pp. 9496-9500, 1990.
- [24] D. D. Sell and H. C. Casey, "Optical Absorption and Photoluminescence Studies of Thin GaAs Layers in GaAs- $\text{Al}_x\text{Ga}_{1-x}\text{As}$  Double Heterostructures," *J. Appl. Phys.*, vol. 45, pp. 800-807, 1974.
- [25] M. Whitehead, G. Parry, K. Woodbridge, P. J. Dobson, and G. Duggan, "Experimental Confirmation of a Sum Rule for Room-temperature Electroabsorption in GaAs-AlGaAs Multiple Quantum Well Structures," *Appl. Phys. Lett.*, vol. 52, pp. 345-347, 1988.
- [26] P. J. Stevens, M. Whitehead, G. Parry, and K. Woodbridge, "Computer Modeling of the Electric Field Dependent Absorption Spectrum of Multiple Quantum Well Material," *IEEE J. Quantum Electron.*, vol. 24, pp. 2007-2016, 1988.
- [27] K. W. Jelley, K. Alavi, and R. W. H. Engelmann, "Experimental Determination of Electroabsorption in GaAs- $\text{Al}_{0.32}\text{Ga}_{0.68}\text{As}$  Multiple Quantum Well Structures as a Function of Well Width," *Electron. Lett.*, vol. 24, pp. 1555-1557, 1988.
- [28] G. Lengyel, K. W. Jelley, and R. W. H. Engelmann, "A Semi-Empirical Model for Electroabsorption in GaAs-AlGaAs Multiple Quantum Well Modulator Structures," *IEEE J. Quantum Electron.*, vol. 26, pp. 296-304, 1990.
- [29] D.S. Gerber, R. Droopad and G.N. Maracas, "Comparison of Electroabsorption in Asymmetric Triangular and Rectangular GaAs/AlGaAs Multiple Quantum Wells," *Appl. Phys. Lett.* 62(5) p. 525-527 (1993)
- [30] G. D. Sanders and K. K. Bajaj, *J Appl. Phys.* **68**, 5348 (1990).
- [31] G. D. Sanders, private communication.
- [32] A. C. Gossard, R. C. Miller and W. Wiegmann, *Surf. Sci.* **174**, 131 (1986).
- [33] R. A. Logan and F. K. Reinhart, *J. Appl. Phys.* **44**, 4172 (1973).
- [34] J. J. LePore, *J. Appl. Phys.*, **51**, 6441 (1980).
- [35] See for example, D. A. B. Miller, D. S. Chemla, T. C. Damen, A. C. Gossard, W. Wiegmann, T. H. Wood and C. A. Burrus, *Phys. Rev. B* **32**, 1043 (1985).
- [36] C. Mailhot, D. L. Smith, *CRC Critical Rev. Solid State Mater. Sci.* **16** (1990) 131.
- [37] M. K. Chin, S. Niki, S. C. Lin, P. K. L. Yu, W. S. C. Chang, *Proc. LEOS Annual Meeting Conference, Florida* (1989) p64.
- [38] G. D. Sanders, K. K. Bajaj, *J. Vac. Sci. Technol. B* **5** (1987) 1295.
- [39] R. A. Puechner, D. S. Gerber, R. Droopad, G. N. Maracas, to be published in *Appl. Phys. Comm.*
- [40] G. D. Sanders, K. K. Bajaj, *Phys. Rev. B* **36** (1997) 4849.
- [41] G. D. Sanders, K. K. Bajaj, *J. Appl. Phys.* **68** (1990) 5348.
- [42] K. T. Shiralagi, PhD Thesis, Arizona State University (1992).



- [43] R Droopad, R A Puechner, K Y Choi, K T Shiralagi and G N Maracas, "Molecular Beam Epitaxial Growth and Optical Properties of Strained Rectangular and Asymmetric Triangular InGaAs Quantum Well Structures," *J. Crystal Growth*, **114** (1991) 327.
- [44] R. Droopad, D.S. Gerber, C. Choi and G.N. Maracas, "Pseudomorphic InGaAs/GaAs and GaAs/AlGaAs Asymmetric Triangular Quantum Wells Grown by MBE for Optoelectronic Device Applications," *J. Crystal Growth*, **127**, p. 606-610 (1993)
- [45] R. Droopad, R. A. Puechner, K. Y. Choi, K. T. Shiralagi, G. N. Maracas, *J. Crystal Growth* **114** (1991) 327.
- [46] G. N. Maracas, J. L. Edwards, D. S. Gerber and R. Droopad, *Applied Surface Science* **63**, 1, 1993
- [47] G.N. Maracas, J.L. Edwards, K. Shiralagi, K.Y. Choi, R. Droopad, B. Johs and J.A. Woolam, *J. Vac. Sci. Tech. A* **10**(4) (1992)
- [48] J.D. Walker, K. Malloy, S. Wang and J.G. Smith, *Appl. Phys. Lett.* **56**(25), 2943-2495 (1990)
- [49] R.M.A. Azzam and N.M. Bashara, Ellipsometry and Polarized Light, 288-315, North Holland/Elsevier, New York (1987).
- [51] R. H. Yan, R. J. Simes, and L. A. Coldren, *IEEE J. Quant. Electron.*, **27**, 1922 (1991).
- [52] G. D. Boyd and G. Livescu, *Opt. and Quant. Electron.*, **24**, S147 (1992).
- [53] N. Debbar, S. Hong, J. Singh, and P. Bhattacharya, *J. Appl. Phys.*, **65**, 383 (1989).
- [54] J. Lee, M. O. Vassel, E. S. Koteles, and B. Elman, *Phys. Rev. B*, **39**, 10133 (1989).
- [55] S. R. Andrews, C. M. Murray, R. A. Davies, and T. M. Kerr, *Phys. Rev. B*, **37**, 8198, (1988).
- [56] Y. J. Chen, E. S. Koteles, B. S. Elman, and C. A. Armiento, *Phys. Rev. B.*, **36**, 4562 (1987).
- [57] G. Livescu, G. D. Boyd, R. A. Morgan, L. M. F. Chirovsky, A. M. Fox, R. E. Leibenguth, M. T. Asom, and M. W. Focht, *Appl. Phys. Lett.*, **60**, 1418 (1992).
- [58] R. H. Yan, R. J. Simes, and L. A. Coldren, "Electroabsorptive Fabry-Perot Reflection Modulators with Asymmetric Mirrors," *IEEE Photon. Technol. Lett.*, vol. 1, pp. 273-275, 1989.
- [59] K. K. Law, R. H. Yan, L. A. Coldren, and J. L. Merz, "Self-electro-optic Device Based on a Superlattice Asymmetric Fabry-Perot Modulator with an On/Off Ratio > 100:1," *Appl. Phys. Lett.*, vol. 57, pp. 1345-1347, 1990.
- [60] G. Livescu, G. D. Boyd, R. A. Morgan, L. M. F. Chirovsky, A. M. Fox, R. E. Leibenguth, M. T. Asom, and M. W. Focht, "Role of Electrorefraction in Quantum-well Fabry-Perot Modulators," *Appl. Phys. Lett.*, vol. 60, pp. 1418-1420, 1992.
- [61] R. H. Yan, R. J. Simes, and L. A. Coldren, "Extremely Low-voltage Fabry-Perot Reflection Modulators," *IEEE Photon. Technol. Lett.*, vol. 2, pp. 118-120, 1990.
- [62] P. M. Petroff, R. C. Miller, A. C. Gossard, and W. Wiegmann, "Impurity Trapping, Interface Structure, and Luminescence of GaAs Quantum Wells Grown by Molecular Beam Epitaxy," *Appl. Phys. Lett.*, vol. 44, pp. 217-219, 1984.
- [63] J. Faist, J. D. Ganiere, P. Buffat, S. Sampson and F. K. Reinhart, "Characterization of GaAs/(GaAs)<sub>n</sub>(AlAs)<sub>n</sub> Surface-emitting Laser Structures Through Reflectivity and High-resolution Electron Microscopy Measurements," *J. Appl. Phys.*, vol. 66, pp. 1023-1032, 1989.
- [64] R. H. Yan, R. J. Simes, L. A. Coldren, and A. C. Gossard, "Transverse Modulators with a Record Reflection Change of >20%/V Using Asymmetric Fabry-Perot Structures," *Appl. Phys. Lett.*, vol. 56, pp. 1626-1628, 1990.
- [65] M. Whitehead, A. Rivers, G. Parry, J. S. Roberts, and C. Button, "Low-voltage Multiple Quantum Well Reflection Modulator with On:Off Ratio > 100," *Electr. Lett.*, vol. 25, pp. 984-985, 1989.
- [66] R. H. Yan, R. J. Simes, and L. A. Coldren, "Surface-normal Electroabsorption Reflection Modulators using Asymmetric Fabry-Perot Structures," *IEEE J. of Quantum Electronics*, vol. 27, pp. 1922-1931, 1991.
- [67] C. Park, K.T. Shiralagi, R. Droopad and G. N. Maracas, "A Novel Bistable MQW Electro-optic Phase Modulator," *Photonics Technology Letters*, **4** (11), p. 1225-1227 (1992)
- [68] Okada M., Takizawa K., "Dynamic response of electro optic bistable devices", *Optical computing in japan*, p.327, 1990.
- Journal of Quantum Electronics*, vol. 20, pp. 265-75, 1984.
- [69] D. A. B. Miller, D. S. Chelma, T. C. Damen, T. H. Hood, C. A. Burrus, A. C. Gossard, and W. Wiegmann, "The quantum well self electro optic effect devices : Optoelectronics bistability and oscillation, and self linearized modulation", *IEEE J. Quantum electron.*, vol. QE-21, pp. 1462-1472, 1985.
- [70] Hsu, T. Y., Efron, Uzi, Wu W. Y., "Multiple quantum well spatial light modulators for optical processing applications", *Optical Engineering*, vol. 27, pp. 372-84, 1988.

- [71] H. Kogelnik and V. Ramaswamy, "Scaling Rules for Thin Film Optical Waveguides", Appl. Opt. vol. 13, p. 1857, 1974.
- [72] J.G. Cody, D. L. Mathine, R. Droopad and G.N. Maracas, "Characteristics of Strained InGaAs/GaAs/AlGaAs Diode Lasers with Asymmetric Triangular Quantum Well Active Regions," submitted to Photonics Technology Letters
- [73] D. Ahn, T. K. Yoo, E. Mendez, S. L. Chuang, "Optical gain control model of the quantum-well laser", J. Appl. Phys. 70 (10), p. 5246, (1991).
- [74] T. Yoo, R. Spencer, W. Schaff, L. Eastman, K. Chung and D. Ahn, "Graded InGaAs/GaAs strained-layer single quantum well laser", Appl. Phys. Lett. 62 (18), p. 2239, (1993).
- [75] R. Droopad, D. S. Gerber K. Y. Choi, K. T. Shiralagi, and G.N. Maracas, "Pseudomorphic InGaAs/GaAs and GaAs/ AlGaAs asymmetric triangular quantum wells grown by MBE for optoelectronic device applications", J. Crystal. Growth, 127, p. 606, (1993).
- [76] C. Aversa and Keigo Iizuka, "Gain of TE - TM modes in quantum well lasers", IEEE J. Quant. Elect., QE-28 (9), p. 1864, (1992).
- [77] A. R. Reisinger, P. S. Zory and R. G. Waters, "Cavity length dependence of the threshold behavior in thin quantum well semiconductor lasers", IEEE J. Quant. Elect., QE-23 (6), p. 993, (1987).
- [78] P. S. Zory, ed. Quantum Well Lasers, Academic Press, San Diego (1993)
- [79] D. L. Mathine, S. Krishnan and G. N. Maracas, "A computational Fourier series solution of the BenDaniel-Duke Hamiltonian for arbitrary shaped quantum wells", submitted to Phys. Rev. B.
- [80] A. Larsson and C. Lindström, "Modulation bandwidth of GaAs/ AlGaAs single quantum well lasers operating at the second quantized state", Appl. Phys. Lett., 54 (10), p. 884, (1989).

## **2. Theoretical treatment of confined excitons in applied fields**

### **Abstract**

We have developed a new highly efficient, accurate and versatile method to calculate the exciton binding energies, transition energies, oscillator strengths and absorption co-efficients in quantum wells with arbitrary potential profiles in the presence of electric and magnetic fields applied along the growth direction. We have studied the excitonic properties in square parabolic and asymmetrical triangular quantum well structures in the presence of electric and magnetic fields. We describe the results of the calculations of the energy levels of confined donor states in coupled double quantum well structures in the presence of applied electric and magnetic fields. We study the effects of electric and magnetic fields on confined donor and exciton states in a dielectric quantum well. We describe the results of our calculations of the binding energy of the ground state of a hydrogenic impurity and excitons in quantum wires in the presence of a magnetic field. Results of the calculations of the energy levels of hydrogenic donors in quantum dots in the presence of a magnetic field are presented. We have developed a new quantum statistical theory of excitonic linewidth due to compositional disordering in semiconductor alloys and quantum well structures in the presence of applied electric and magnetic fields and have applied it to several different alloy systems and quantum confined structures.

### **2.1. A New Method For Calculating Excitonic Properties In Quantum-Confined Semiconductor Structures With Arbitrary Potential Profiles In The Presence Of Applied Fields**

We have developed a simple but highly efficient, accurate and versatile method to calculate the exciton binding energies, transition energies, oscillator strengths and absorption coefficients in quantum wells with arbitrary potential profiles in the presence of electric and magnetic fields applied along the growth direction<sup>1,2</sup>. We have studied the excitonic properties in square, parabolic, and asymmetrical triangular quantum-well structures in the presence of electric and magnetic fields.

This method can also be applied to describe the properties of a donor in a quantum well with an arbitrary potential profile in the presence of both the electric and magnetic fields applied along the growth direction. As an illustration we have calculated the values of the binding energy of the ground state of a donor located in a coupled double quantum well structure as a function of its position, the well width, and electric and magnetic fields.

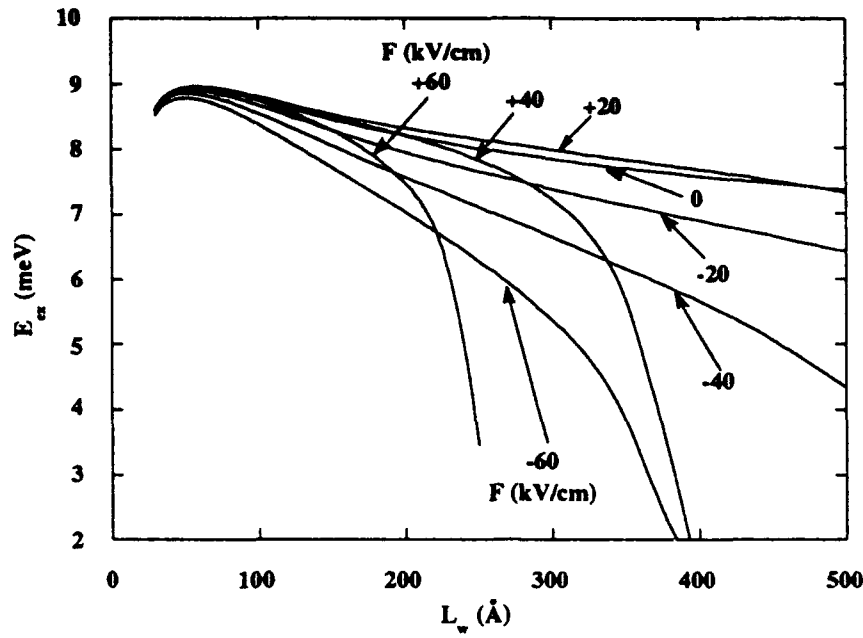
We have developed a powerful variational formalism in which the analytical form of the trial wavefunction is approximated using a variational function for the electron and hole correlated motion along the growth direction in a highly confined quantum well structure. This variational function is then determined approximately through evaluating a double integral. Such a simple procedure saves much valuable computation time in obtaining many important properties of excitons in quantum well structures. We have calculated the values of the binding energies, transition energies and oscillator strengths of both the heavy-hole and the light-hole excitons in square and asymmetrical triangular quantum-well structures in the presence of an electric field applied parallel to the direction of growth. The results thus obtained are in good agreement with those of other calculations. We have also applied this formalism to study the excitonic properties in quantum confined structures with arbitrary potential profiles in the presence of a magnetic field applied parallel to the growth direction using an appropriate form of the trial wavefunction. And finally, we have extended our formalism to the case where both the electric field and the magnetic field are applied simultaneously. The main advantage of our formalism lies in the fact that we need to determine only one variational parameter for the case where both the electric and the magnetic fields are present simultaneously. Therefore, exciton wavefunctions, binding energies and oscillator strengths are much easier to obtain than optimizing a multidimensional integral equation of several variational parameters in the conventional variational approaches.

We have also adapted our formalism to calculate the energy levels of a hydrogenic impurity in a coupled double quantum well structure in the presence of electric and magnetic fields by letting the hole mass go to infinity and the hole subband wavefunction to a delta function.

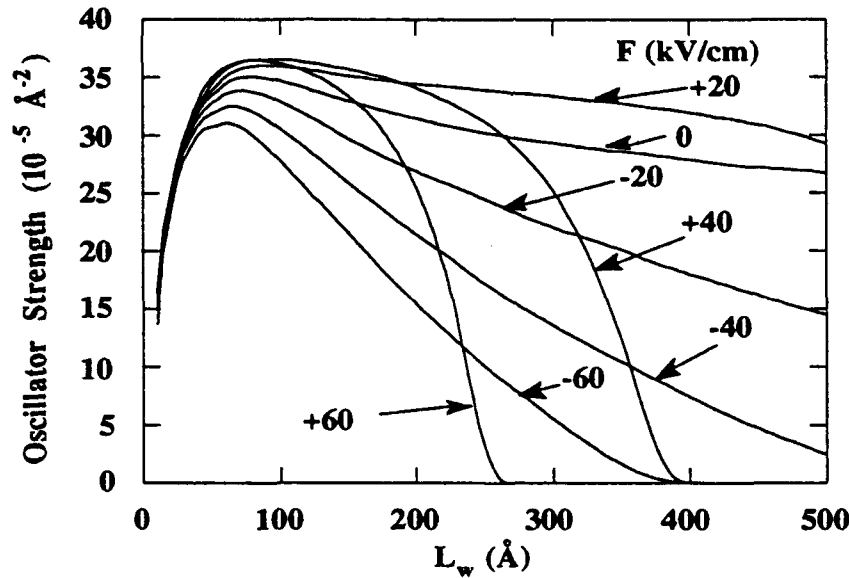
(a) Excitonic Properties in an Electric Field

We have calculated the binding energies and oscillator strengths of both the heavy-hole and the light-hole excitons in a GaAs/Al<sub>0.3</sub>Ga<sub>0.7</sub>As square quantum well as a function of well width and applied field strengths. The exciton binding energy decreases as field strength increases. Although our calculated exciton binding energies are almost the same as those of Sanders and Bajaj<sup>3</sup> over a wide range of well widths and electric fields, our oscillator strengths are about 40 % higher than theirs. However, our values of the oscillator strength are closer to those of Bauer and Ando<sup>4</sup> for small well widths where the valence band mixing effects are not important. In our calculations we have neglected the effects of valence subband mixing. Also our oscillator strengths follows a correct trend as a function of well width and applied electric field strength.

The asymmetrical triangular quantum well structures are expected to have higher contrast ratios than those of square well and parabolic well structures<sup>3</sup>. The exciton binding energy and oscillator strength versus well width for heavy-hole excitons in the asymmetrical triangular quantum wells at a few applied electric field strengths are shown in Fig. 1. When the applied field is large enough, the confining potential for either the electron or the hole disappears in the asymmetrical triangular quantum well, thus, the bound state in the quantum well ceases to exist. As shown in Fig. 1(a), the exciton binding energy drops rapidly near  $L_w = 400 \text{ \AA}$  at  $F = 40 \text{ kV/cm}$ . This indicates a drop in the hole potential of  $0.16 \text{ eV}$  that is larger than the confining potential barrier  $E_v = 0.151 \text{ eV}$ . The two-dimensional enhancement of the optical absorption can be switched on and off by a small change in the applied electric field under a specific bias condition. The largest field-induced change in the oscillator strength can be obtained under the bias condition where the heavy-hole confining potential vanishes due to the applied electric field, as one can observe from Fig. 1(b) at  $F = 40 \text{ kV/cm}$  and  $F = 60 \text{ kV/cm}$  for the well widths of  $400$  and  $250 \text{ \AA}$ , respectively. Thus, in these operating regions one can expect an excellent performance of the modulators.



(a)



(b)

Fig. 1 Variation of the (a) the heavy-hole exciton binding energy ( $E_{ex}$ ), (b) oscillator strength as a function of well width ( $L_w$ ) in a GaAs- $A_{0.3}Ga_{0.7}As$  asymmetric triangular well for several values of the electric field ( $F$ ).

#### (b) Excitonic Properties in a Magnetic Field

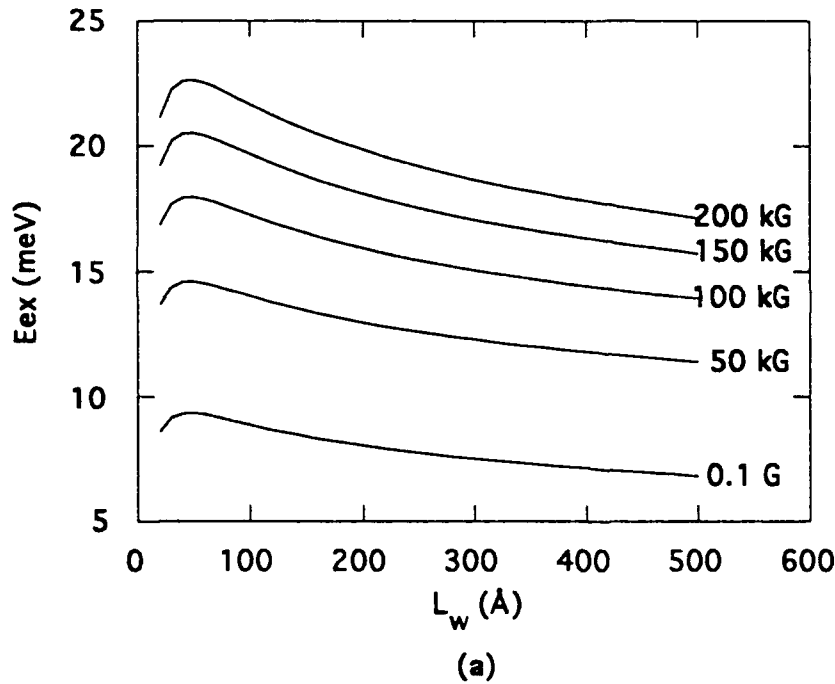
We have used our formalism to calculate the binding energies and the oscillator strengths of both the heavy-hole and the light-hole excitons in square, parabolic and asymmetrical triangular quantum well structures in the presence of a magnetic field. The exciton binding energies obtained using our

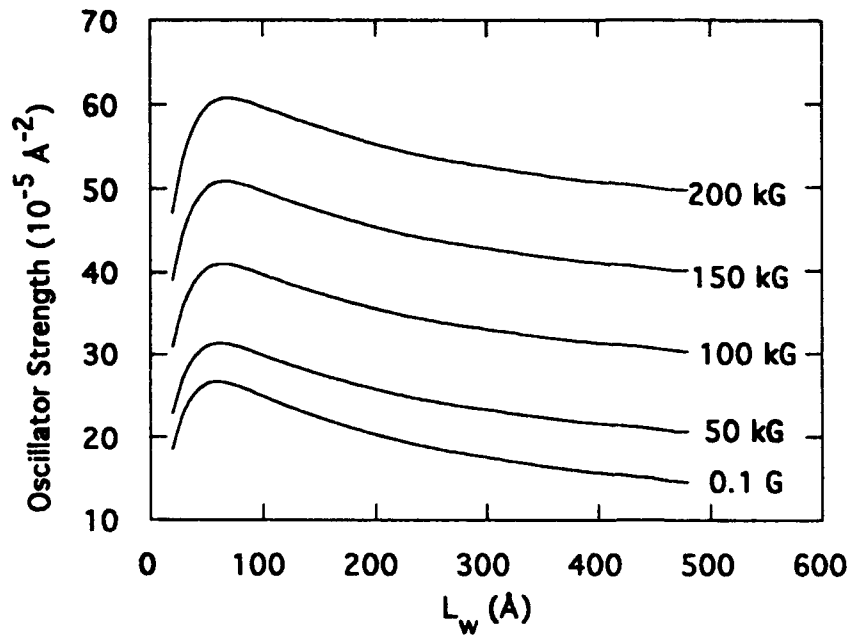
approach in the case of square wells agree very well with previous calculations<sup>5,6</sup>. For a given well size our calculated binding energies and oscillator strengths increase as the magnetic field increases, due to larger in-plane confinement of the electrons and holes. At high magnetic fields, we have a quasi-zero-dimensional exciton and the oscillator strength becomes very large.

In Fig. 2, we show the variations of the heavy-hole exciton binding energies and oscillator strengths in an asymmetrical triangular quantum well as a function of well width for several values of the magnetic field. The exciton binding energies and the oscillator strengths follow the same trends as those in the square quantum wells. However, they are less sensitive to the well width variations compared to those in the square wells.

(c) Excitonic Properties in both an Electric and a Magnetic Field

In Fig. 3, we show the variations of the heavy-hole exciton binding energies and oscillator strengths as a function of well width in a square-quantum well in the presence of a few typical applied electric and magnetic field strengths<sup>7</sup>. The binding energies and oscillator strengths are grouped by the magnetic field strengths. For the sake of clarity of display we shift the horizontal axes (the quantum well widths) for the curves with  $B_z=50$  kG, 100 kG, 150 kG, and 200 kG by 100 Å, 200 Å, 300 Å, and 400 Å, respectively.





(b)

Fig. 2 Variations of the (a) the heavy-hole exciton binding energy ( $E_{ex}$ ), and (b) oscillator strength as a function of well width ( $L_w$ ) in a GaAs- $A_{0.3}Ga_{0.7}As$  asymmetric triangular well for several values of the magnetic field strength.

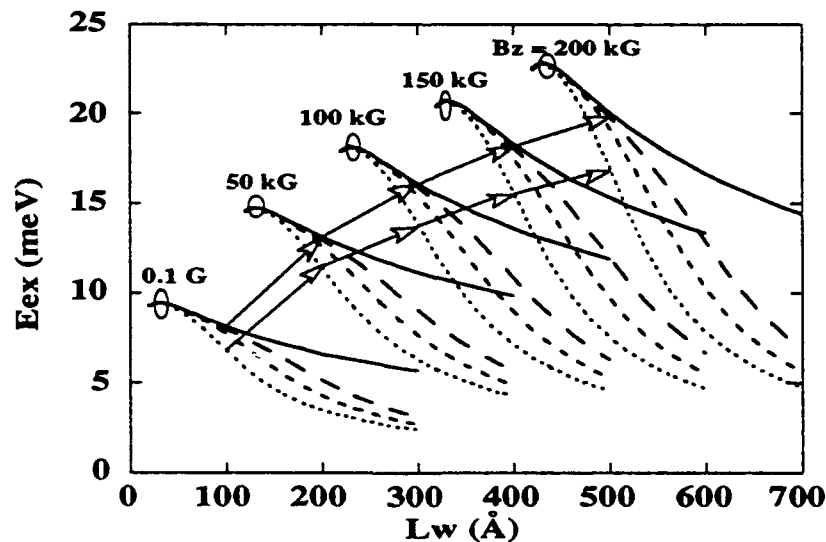


Fig. 3 Variation of the heavy-hole exciton binding energy ( $E_{ex}$ ) as a function of well width ( $L_w$ ) in a GaAs- $A_{0.3}Ga_{0.7}As$  square well for several values of the magnetic and electric field strengths. The quantum well width axis are shifted by 0 Å, 100 Å, 200 Å, 300 Å, and 400 Å for the magnetic field strengths of 0.1 G, 50 kG, 100 kG, 150 kG, and 200 kG, respectively. The solid lines are for the electric field strength  $F = 0$ ; the long dashed lines are for  $F = 20$  kV/cm; the dashed lines are for  $F = 40$  kV/cm; the dotted lines are for  $F = 100$  kV/cm.

The exciton binding energies and the oscillator strengths increase with the increase in magnetic field, but decrease with the increase in the electric field as expected. In a given magnetic field and for narrow wells, the exciton binding energies and oscillator strengths are relatively insensitive to the applied electric field because the electron and the hole cannot be pulled far apart from each other due to the strong confining potentials. However, we can obtain significant electric field induced changes in these quantities for relatively large well widths ( $L_w \geq 100 \text{ \AA}$ ) due to large electric field induced electron and hole separations in wide quantum wells. The electric field induced changes in the exciton binding energies and oscillator strengths at any given well width increase as the applied magnetic field strength increases. For example, the electric field induced changes in oscillator strength from  $F=0$  to  $100 \text{ kV/cm}$  in the  $100 \text{ \AA}$  quantum well are  $14 (10^{-5} \text{ A}^{-2})$  and  $27 (10^{-5} \text{ A}^{-2})$  for  $B_z=0$  and  $B_z=200 \text{ kG}$ , respectively. In a narrow well, in the presence of a strong magnetic field, the excitonic behavior in quantum wells resembles to that in quantum dots.

## 2.2. Effects Of Parallel Electric And Magnetic Fields On Confined Donor States In A Coupled Double Quantum Well

Coupled double quantum wells have attracted much attention due to the enhanced quantum confined Stark effect in the excitonic transition, leading to their application in more sensitive electro-optic devices.<sup>8</sup> The enhanced tunneling of electron and hole across the center barrier in opposite directions under an applied electric field can drastically increase the change in excitonic transition energy and oscillator strength as compared to that in a single quantum well.<sup>9</sup> A similar problem concerning confined donor states in a coupled double quantum well in response to applied electric and magnetic fields is also of interest.

An electric field applied along the growth direction tilts the bottom of the potential well and alters the electronic charge distribution inside the well. The overall shape of the electron wave function is rather stable in a single quantum well if the applied electric field is not too strong as to eject the electron out of the quantum well. The situation is different, however, in an asymmetric coupled double quantum well (ACDQW) structure consisting of a wide well and a narrow well separated by a thin barrier across which electron tunneling can occur. Since the ground state electron wave function is not evenly distributed in such a structure, but rather is predominantly in the wide well, a moderate electric field could tilt the potential profile in such a way that the wave function shifts across the thin barrier into the narrow well, at the same time without making the electron escape from a confined state in the structure. For a donor in the wide well or in the narrow well, the change in the binding energy can therefore be much more significant as compared to that in a single quantum well under the same electric field.

We have calculated the binding energies of the  $1s$  and  $2p_z$  donor states in a  $\text{GaAs-Al}_x\text{Ga}_{1-x}\text{As}$  ACDQW structure, using a variational approach. In Fig. 4, we show the variation of the  $1s$  donor binding energy  $E_b$  and the  $1s \rightarrow 2p_z$  transition energy  $E_T$  as functions of the electric field, at zero magnetic field, in a ACDQW with  $L_1=50 \text{ \AA}$ ,  $L_b=20 \text{ \AA}$ ,  $L_2=25 \text{ \AA}$ . Two cases are considered: (1) a donor at the center of the narrow well and, (2) a donor at the center of the wide well. Since the electron is mainly confined in  $L_1$ , the binding energy of the donor in the wide well is higher than that in the narrow well at  $E=0$ . As the electric field is increased, the electron is pulled towards the narrow well, and can tunnel across the thin barrier, away from the donor in the wide well. The binding energy of donor in the wide well therefore decreases while that in the narrow well increases. Although such different behavior in an electric field were also found for donors distributed in a single quantum well, the rate of change in the binding energy is significantly higher in an ACDQW, due to the easy redistribution of the electron wave function across a thin barrier in an electric field.

In Fig. 5, we also show the variations of the  $1s \rightarrow 2p_z$  transition energies as function of the magnetic field  $B$  at  $E=0$  and  $|E|=100 \text{ kV/cm}$ , for (1) a donor at the center of the narrow well and, (2) a donor at the center of the wide well. It is clear that the magnetic field along the growth axis always increases the transverse confinement of the electron in the quantum well structure, regardless of donor location or the strength of the lateral electric field, so the  $1s$  binding energy and the  $1s \rightarrow 2p_z$  transition energy monotonically increase.



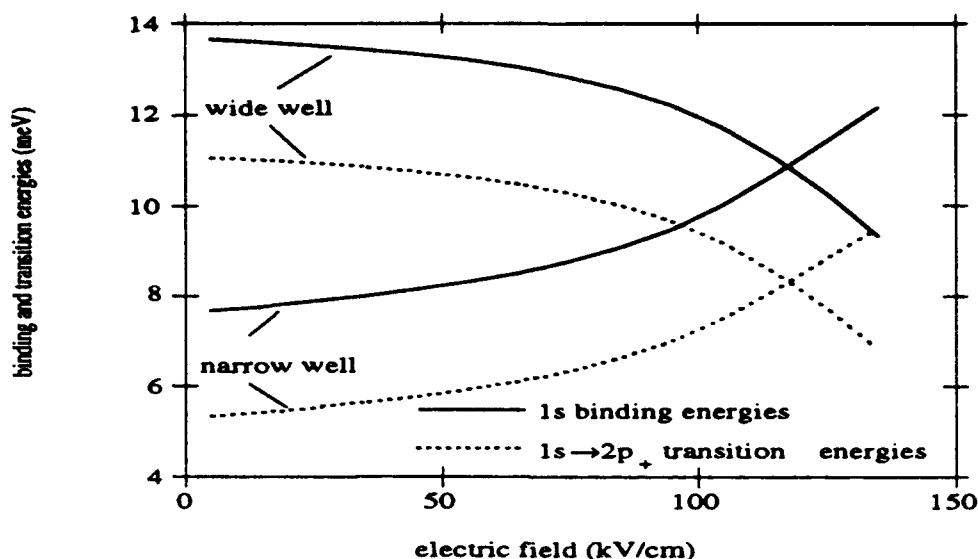


Fig. 4 Variation of the binding energy of the  $1s$  donor state and the  $1s \rightarrow 2p_+$  transition energy as a function of  $|E|$  in the absence of the magnetic field, for donors located at the center of the narrow well and at the center of the wide well.  $L_1=50 \text{ \AA}$ ,  $L_b=20 \text{ \AA}$ ,  $L_2=25 \text{ \AA}$ . Bohr radius  $a_B=100 \text{ \AA}$ , relative Rydberg  $R=5.8 \text{ meV}$ .

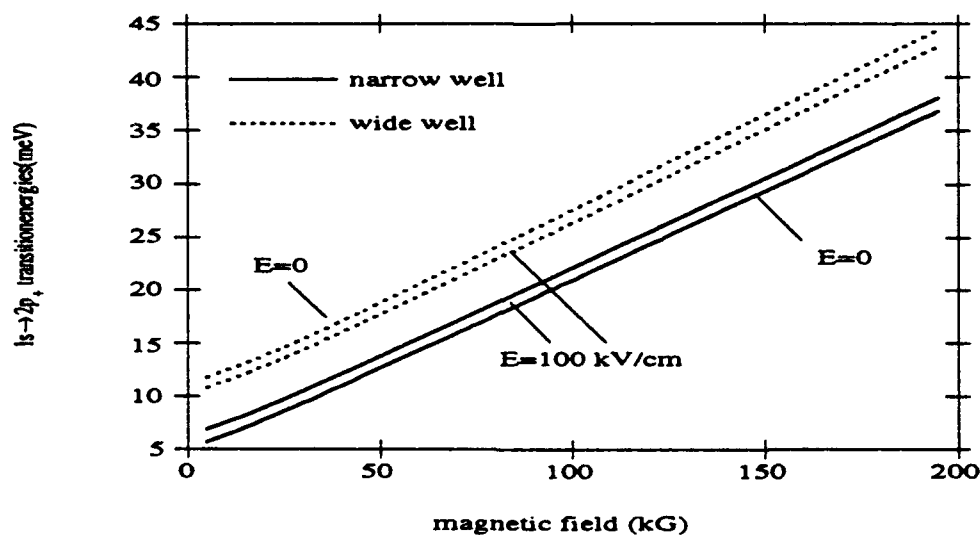


Fig. 5 Variations of the  $1s \rightarrow 2p_+$  transition energies as a function of the magnetic field, for donors located at the center of the narrow well and at the center of the wide well.  $L_1=50 \text{ \AA}$ ,  $L_b=20 \text{ \AA}$ ,  $L_2=25 \text{ \AA}$ . Bohr radius  $a_B=100 \text{ \AA}$ , relative Rydberg  $R=5.8 \text{ meV}$ .

### 2.3. Confined Donor States In Cross Electric And Magnetic Fields In A Coupled Double Quantum Well

In the last section, we considered the effects of parallel electric and magnetic fields on confined donor states in a coupled double quantum well. A similar problem concerning confined donor states in a coupled double quantum well in response to perpendicular electric and magnetic fields is also of interest. In a perpendicular configuration ( $\mathbf{B} \perp \mathbf{E}$ ), the magnetic field provides a confinement in both the growth direction and in the quantum well planes, directly competing with the electric field in affecting how wave functions will adjust in the external fields. In addition, components of the angular momentum are no longer conserved, which leads to mixing of the eigenstates of the angular momentum.

In a single quantum well, the degeneracy between the  $2p_z$  and  $2p_{x,y}$  bulk states is lifted. Of the  $2p$  states associated with the first subband  $E_1$ ,  $2p_x$  and  $2p_y$  have a lower energy level. The  $2p_z$  state has a higher energy level than the first subband  $E_1$ , though it is a perfectly bound state with an energy level above the first subband but maybe below the second subband. In a coupled double quantum well, proper choices of well and barrier sizes and the application of the electric field can bring the first and second subbands close to each other. Both subbands should contribute to the  $2p_z$  level in case the energy separation between the first and second subbands is small. In such cases,  $2p_y$  and  $2p_z$  are rearranged into two new states (we call them  $2p_1$  and  $2p_2$ ) in a magnetic field, one more tightly and one less tightly bound.

We calculate energy levels of the  $1s$  and the  $2p$  donor states associated with the lowest two electronic subbands and the transition energies between them, with varying electric and magnetic fields, for a number of donor positions within a GaAs- $\text{Al}_x\text{Ga}_{1-x}\text{As}$  ACDQW structure depicted in Fig. 6 ( $x=0.3$  is used here). We use an effective mass approximation and follow a variational approach. In Fig. 7, we show the transition energies between the  $1s$  and  $2p$  donor states in an asymmetric coupled double quantum well as function of the electric field. In the absence of the magnetic field, the  $1s \rightarrow 2p_x$  and  $1s \rightarrow 2p_y$  transitions are degenerate and the  $1s \rightarrow 2p_z$  is essentially an intersubband transition, because there is no coupling between the  $2p_y$  and the  $2p_z$  states. We present here transition energies in a 100 kG magnetic field, and take the coupling between the  $2p_y$  and  $2p_z$  states into account. Two cases are considered: a donor at the center of the narrow well, and a donor at the center of the wide well. Since the electron is mainly confined in the wide well, the binding energies (and hence the transition energies) of the donor in the wide well are higher than those in the narrow well in the absence of the electric field. As the electric field is increased, the electron is pulled towards the narrow well. Also the separation between the first two subbands is reduced in the applied electric field. For the donor in the wide well, all three  $1s \rightarrow 2p$  transition energies decrease in the applied electric field, because of the reduced electron binding. For the donor in the narrow well, the  $1s \rightarrow 2p_x$  and  $1s \rightarrow 2p_1$  transition energies increase in the applied electric field because of the enhanced electron binding. On the other hand, the  $1s \rightarrow 2p_2$  transition, which is intersubband in nature, initially decreases in the applied electric field, mainly because of the reduced separation between the first and second subbands. As the electric field increases further, the coupling between the  $2p_y$  and  $2p_z$  states becomes stronger and  $1s \rightarrow 2p_2$  starts to increase.

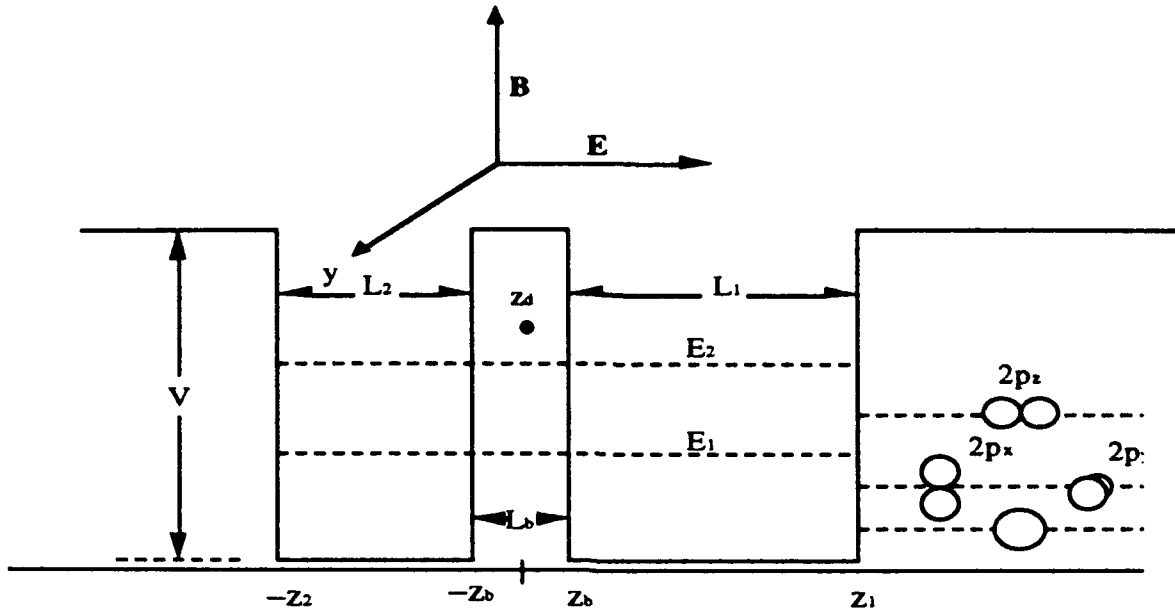


Fig. 6 Schematic conduction band diagram for an asymmetric coupled double quantum well. The electric field  $E$  is applied parallel to and the magnetic field  $B$  perpendicular to the growth direction of the structure.

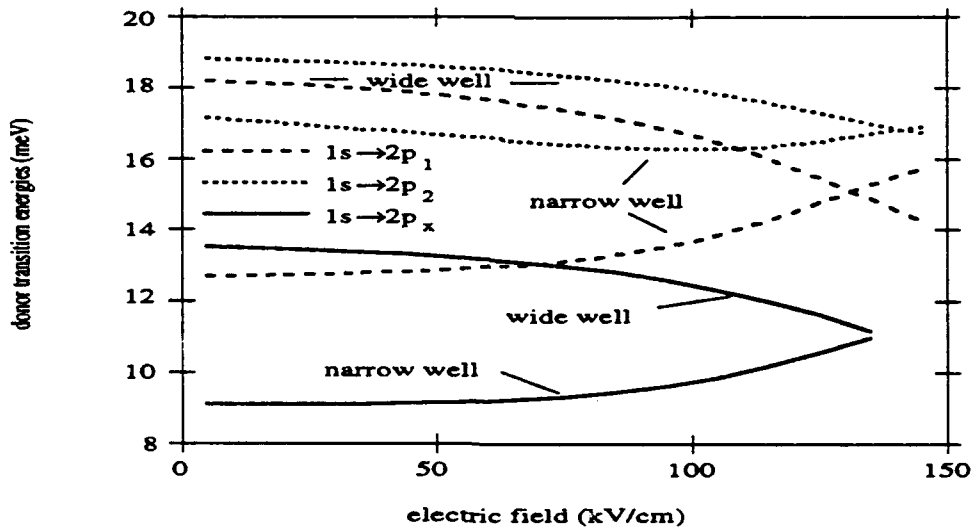


Fig. 7 Variations of the  $1s \rightarrow 2p$  transition energies as a function of the electric field in a coupled double quantum well, for donors located at the center of the narrow well and at the center of the wide well, in the presence of a 100 kG magnetic field applied parallel to the quantum well planes (in the  $x$ -direction).  $L_1=50$  Å,  $L_b=20$  Å,  $L_2=25$  Å. Bohr radius  $a_b=100$  Å, relative Rydberg  $R=5.8$  meV.

## 2.4. Effects Of Electric And Magnetic Fields On Confined Donor And Exciton States In A Dielectric Quantum Well

Dielectric quantum wells have recently received increasing attention because of the progress in the fabrication processes and their potential to sustain electro-optic operations with greater range of applicable electric fields.<sup>10,11</sup> A quantum well can be called "dielectric" when the dielectric constant of the barrier material is significantly smaller than that of the well material, as in the case of a GaAs-ZnSe quantum well and others constructed according to the same principle. Image charges arise due to the mismatch of dielectric constants at the interfaces. Binding energies of donors and excitons can be significantly enhanced because of the additional confinement effect produced by the image charge distribution. Dielectric quantum wells provide an interesting possibility of constructing optoelectronic devices at desired wavelengths using transitions among states associated with different electronic subbands with appropriate choices of material parameters such as dielectric constants and conduction band mismatch.

In this Section, we describe the results of our calculation of the donor and exciton binding energies in the dielectric quantum wells, in the presence of parallel electric and magnetic fields applied along the growth direction. We calculate the variations of the binding energy of the  $1s$  state, and the  $1s \rightarrow 2p_z$  transition energy, as a function of the applied electric and magnetic fields, with various choices of dielectric constants, and discuss how the electric field effects the behavior of the donor states.

In Fig. 8, we display the variation of the  $1s$  donor binding energies and the  $1s \rightarrow 2p_z$  transition energies as a function of the applied magnetic field for a donor in a 100 Å dielectric quantum well. Two cases are considered: (1) the donor is at the center of the well and (2) the donor is at the edges of the well. It is clear that the magnetic field along the growth axis always increases the transverse confinement of the electron in the quantum well structure, so the  $1s$  binding energy and the  $1s \rightarrow 2p_z$  transition energy monotonically increase, regardless of donor location or the strength of the applied electric field.

In Fig. 9, we show the variation of the binding energies of a hydrogenic donor at the center of the dielectric quantum wells as a function of the applied electric field, in the absence of magnetic field. Three cases are considered (represented by curves 1—3) to study the effect of the image charge distribution. For curve 1, the dielectric constant of the well layer is used in the calculation for both the well and barrier materials; for curve 2, the average of the two dielectric constants is used for both the well and barrier materials; for curve 3, the actual dielectric constants are used. Since the electron is mostly confined inside the quantum well, it is clear that the very significant increase in the donor binding energies when different dielectric constants are used can be mainly attributed to the additional confinement by the image charge distribution, rather than to the reduction of the dielectric constant in the well region when the average dielectric constant is used. As the electric field is increased, the electron is pulled away from the donor. As a result, the binding energies decrease as a function of the electric field for the well-center donor. On the other hand, a magnetic field applied along the growth axis always increases the transverse confinement of the electron in the quantum well structure, regardless of donor location or the strength of the lateral electric field, so the binding energies monotonically increase.

We have also calculated the binding energies of the heavy-hole and the light-hole excitons in a GaAs-ZnSe dielectric quantum well in a magnetic field. Aside from the expected increase in the values of the binding energies due to smaller average electron-hole distance when the quantum well gets smaller, we observe that at zero field the binding energies in these structures can exceed the conventional two-dimensional limit, i.e. four times the bulk Rydberg. This unique property is attributed to the strong dielectric mismatch in these structures. Also, for a given value of the well size, the values of the binding energy increase as a function of the magnetic field. We are now in the process of calculating the binding energies, oscillator strengths and absorption coefficients of excitons in dielectric quantum wells in the presence of an electric field and explore their potential for use spatial light modulators.

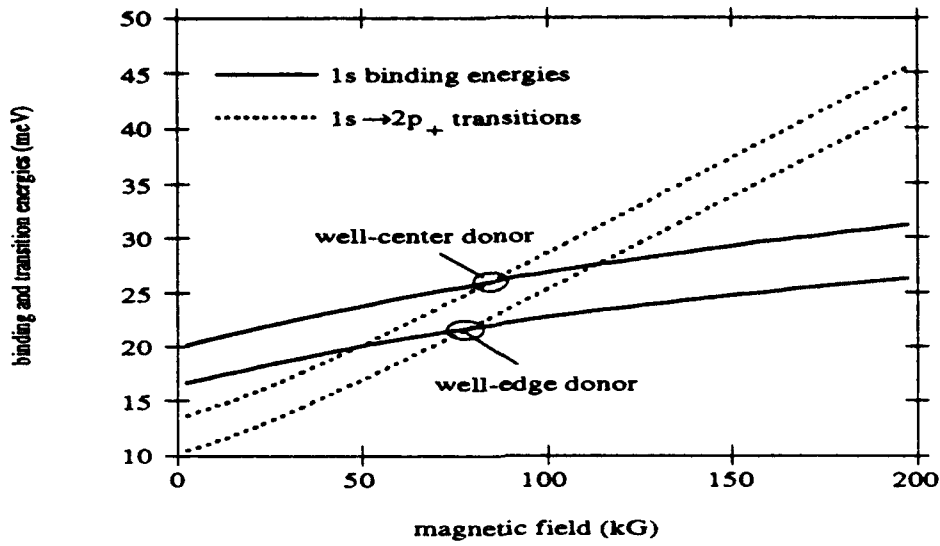


Fig. 8 Variations of the 1s donor binding energies and the  $1s \rightarrow 2p_+$  transition energies as a function of the applied magnetic field in a  $100 \text{ \AA}$  GaAs-ZnSe dielectric quantum well, for donors located at the center and at the edges of the quantum well. Bohr radius  $a_B = 100 \text{ \AA}$ , relative Rydberg  $R = 5.8 \text{ meV}$ . Height of the confining potential barrier  $V = 340 \text{ meV}$ .

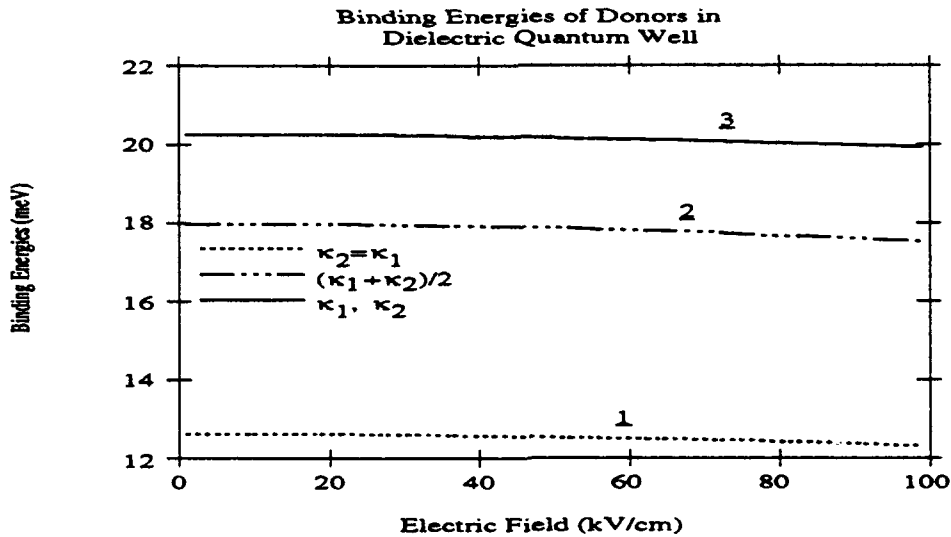


Fig. 9 Variations of binding energies of a well-center donor as functions of the applied electric field. Quantum well size  $L = 100 \text{ \AA}$ . The dielectric constant of the well layer is  $\kappa_1$ , that of barrier material  $\kappa_2$ .  $\kappa_1 = \kappa_2 = 12.5$  for curve 1 ( $R = 5.8 \text{ meV}$ );  $\kappa_1 = \kappa_2 = 10.1$  for curve 2; ( $R = 8.9 \text{ meV}$ ) and  $\kappa_1 = 12.5$ ,  $\kappa_2 = 7.6$  for curve 3 ( $R = 5.8 \text{ meV}$ ).

## 2.5. Hydrogenic Impurities In Quantum Wires In The Presence Of A Magnetic Field.

An understanding of the physics of impurity states in semiconductor quantum wire (QW) structures is an important problem. The reduction of dimensionality in QWs, can be controlled by changing the radius of the wire. An electron bound to an impurity at the center of a QW never "sees" the surface of the wire in a very wide wire, and behaves as a 3-D electron bound to an impurity ion in GaAs. For intermediate wire sizes (of the order of Bohr radius), the electron confinement due to the potential well on the boundary is greater than the confinement due to the Coulomb interaction of the impurity ion, and the electron thus behaves as a quasi-one dimensional system. For very narrow wires, the finite potential barrier well cannot effectively confine the bound electrons, which leak out as 3-D electrons in  $\text{Ga}_{1-x}\text{Al}_x\text{As}$  bound to the impurities and weakly perturbed by the potential wall; furthermore, it is well known, that the reduction of dimensionality, increases the effective strength of the Coulomb interaction.

We have calculated the binding energies of a hydrogenic donor in a quantum wire for infinite and finite potential wells, in the presence of a uniform magnetic field, as a function of the width of the quantum wire, for the case of an impurity located on and off the axis of the wire. We assume that the magnetic field is applied parallel to the axis of the wire. The calculations have been performed by using a suitable variational wave function, which takes into account the confinement (either infinite or finite) of the carriers in the wire, and the influence of the Coulomb interaction between the impurity ion and the electron. For an impurity ion located on the axis of the QW binding energy continues to increase as the radius of the wire decreases for the infinite potential case, while in the presence of a magnetic field, additional increases for the binding energy are reported, especially for larger wire radii. For finite potential, the binding energy in general, has a maximum at a specific wire radius value; for smaller radii, the electron leaks out into the surrounding medium, and the binding energy tends to approach its 3D value in AlGaAs, while for large wire radii, binding energy goes to the similar limit in GaAs (see Fig. 10).

## 2.6. Exciton Binding Energies In A Quantum Wire In The Presence Of A Magnetic Field

We have calculated the binding energies of both the heavy-hole and the light-hole excitons in a quantum wire (QW) with an infinite potential barrier, in the presence of a uniform magnetic field, as a function of the width of the quantum wire. We assume that the magnetic field is applied parallel to the axis of the wire. The calculations have been performed by using a suitable variational wave function, which takes into account the confinement of the carriers in the wire, the influence of the Coulomb interaction, and the magnetic field strength. The binding energy continues to increase as the radius of the wire decreases, while in the presence of magnetic field, additional increases for the binding energy are reported, especially for larger wire radii (see Fig. 11). The average electron-hole separation, increases to the bulk value, for larger well radii, while in the presence of magnetic field, the separation is reduced. It is also shown that the optical absorption coefficient diverges for an arbitrary magnetic field, with decreasing wire size (see Fig. 12). Similar results are also obtained for the light-hole exciton.

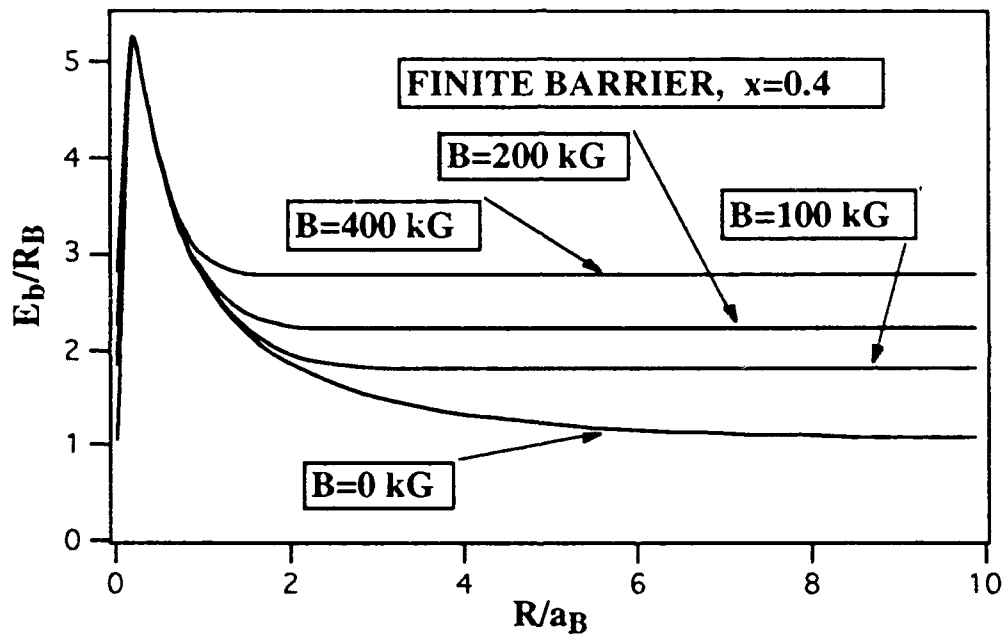


Fig. 10 Variation of the binding energy of a donor ( $E_b$ ), expressed in terms of a hydrogenic Rydberg ( $R_B$ ) in GaAs (5.8 meV) as a function of the radius of the wire ( $R$ ) expressed in terms of the Bohr radius ( $a_B$ ) in GaAs ( $\sim 98 \text{ \AA}$ ) for several values of the magnetic field.

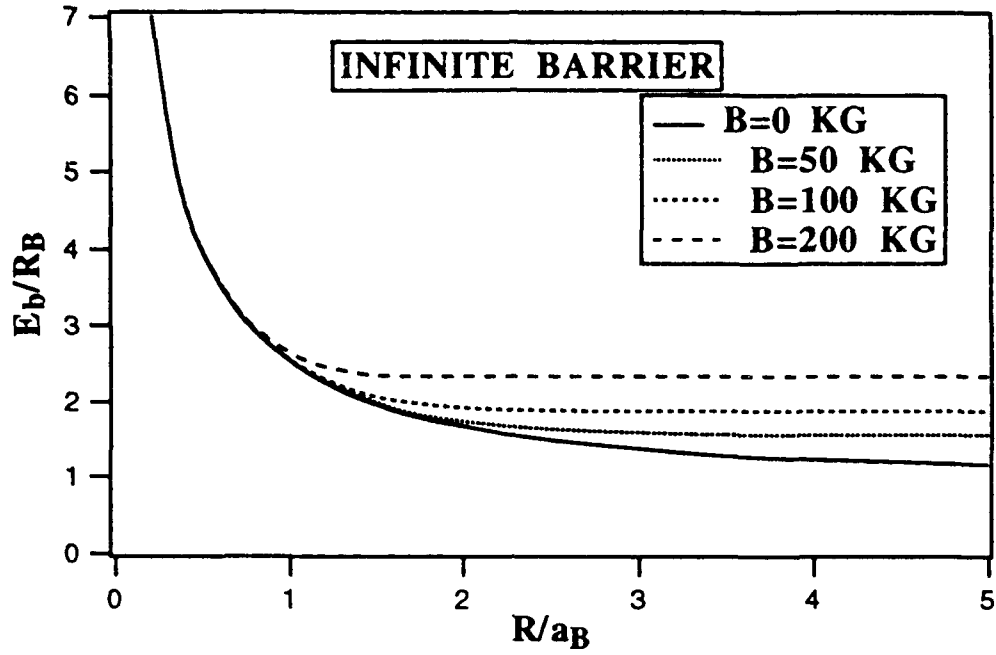


Fig. 11 Variation of the binding energy of a heavy-hole exciton ( $E_b$ ), expressed in terms of an exciton Rydberg ( $R_B$ ) in GaAs ( $\sim 3.9$  meV) as a function of the radius of the wire ( $R$ ) expressed in terms of Bohr radius ( $a_B$ ) in GaAs ( $\sim 148$  Å) for several values of the magnetic field.

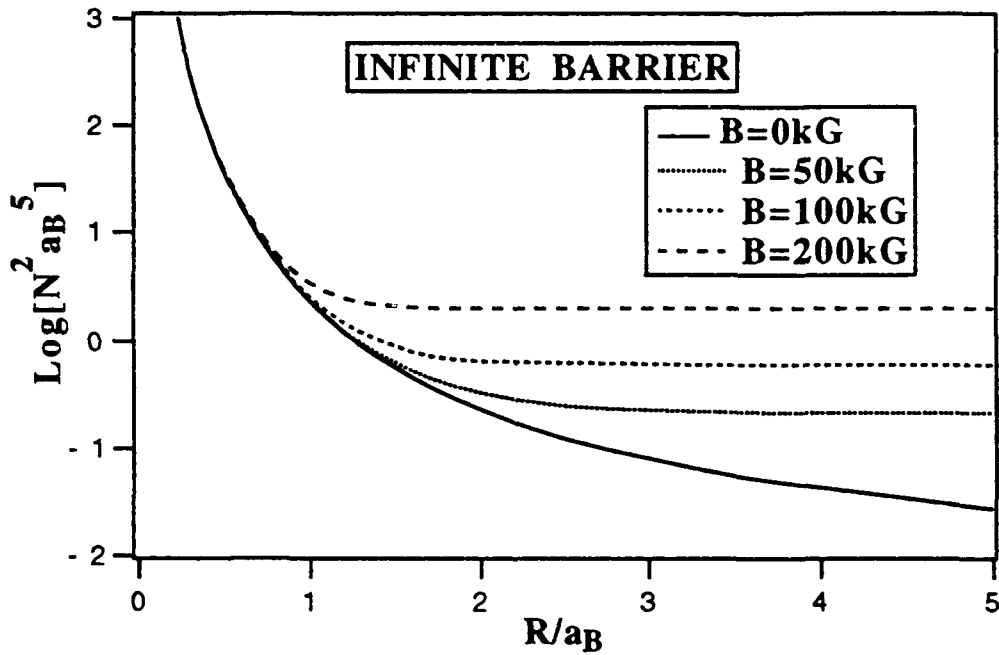


Fig. 12 Variation of the natural logarithm of the normalized optical absorption coefficient of the heavy exciton as a function of wire radius ( $R$ ), expressed in terms of Bohr radius ( $a_B$ ) in GaAs ( $\sim 148$  Å) for several values of the magnetic field.



## 2.7. Hydrogenic Donor States In Quantum Dots In The Presence Of A Magnetic Field

The physics of impurity states in semiconductor quantum dot [QD] structures is an interesting subject. In the case of a spherical dot the reduction of dimensionality can be controlled by changing the radius of the dot. An electron bound to an impurity at the center of a QD never "sees" the surface of the dot for a very large dot radius, and behaves as a 3-D electron bound to an impurity in GaAs, in a GaAs- $\text{Al}_x\text{Ga}_{1-x}\text{As}$  structures. For very small radii, and for an infinite barrier model, the electron kinetic energy increases drastically and supersedes the attractive potential due to the impurity ion. Furthermore, it is well known that the reduction of dimensionality increases the effective strength of the Coulomb interaction, and in effect the binding energy.

Extensive theoretical work on hydrogenic impurity states in QDs has been reported.<sup>12</sup> The binding energy has been calculated as a function of dot size, for infinite and finite confining potentials. The calculated results show stronger confinement and larger binding energies for hydrogenic impurities in QDs than in quantum wires and quantum wells. All these calculations have been done in the absence of a magnetic field.

We have calculated the binding energy of a hydrogenic impurity in a quantum dot (assumed to be in the form of disc of radius  $R$  and length  $L$ ) with infinite potential barriers at all surfaces in the presence of a uniform magnetic field applied parallel to the disk axis, for the case of an impurity ion located on the axis of the disk. The calculations have been performed by using a suitable variational wave function, which takes into account the confinement of the carriers in the disk (axial and radial), and the influence of the Coulomb interaction between the impurity ion and the electron. The binding energy for a hydrogenic ion located at the center of the disk strongly depends on the disk radius and length. The 3-dimensional confinement of the quantum disk results in larger binding energies for the hydrogenic donor than in the corresponding quantum well and quantum wire structures for an arbitrary magnetic field. The binding energy continues to increase as the radius and length of the wire decrease for the infinite potential barrier case (Fig. 13), while in the presence of magnetic field, additional increases for the binding energy are reported, especially for larger wire radii (Fig. 14). We recover 2-dimensional and 3-dimensional limits for the binding energy for various combinations of disk radius and length (Fig. 15).

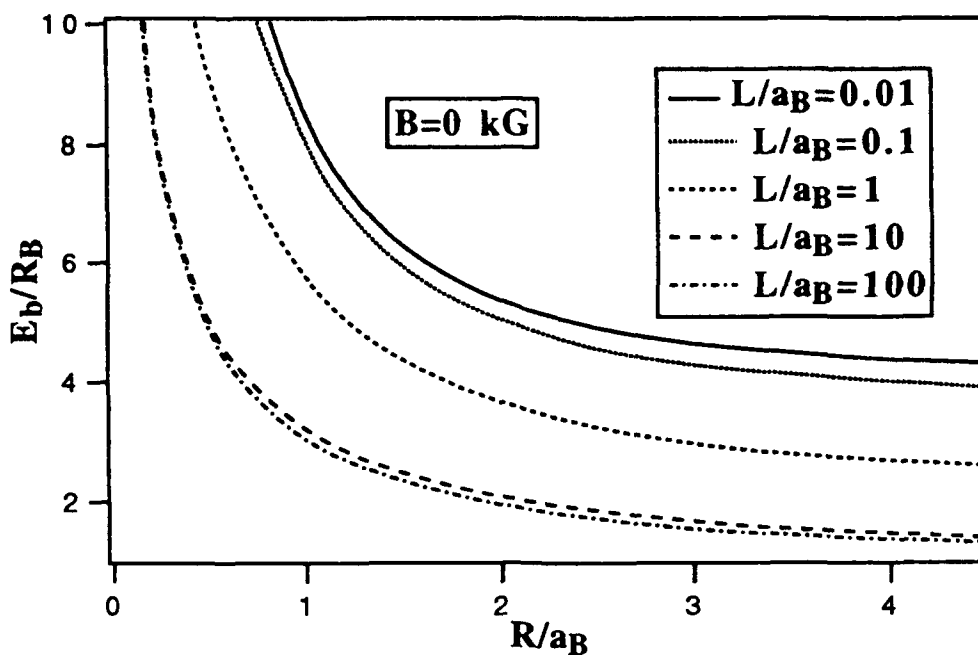


Fig. 13 Variation of the binding energy of a donor ( $E_b$ ), expressed in terms of a hydrogenic Rydberg ( $R_B$ ) in GaAs (5.8 meV) as a function of the radius of the wire ( $R$ ) expressed in terms of the Bohr radius ( $a_B$ ) in GaAs ( $\sim 98 \text{ \AA}$ ) for several values of the disk length ( $L$ ) for  $B=0$ .

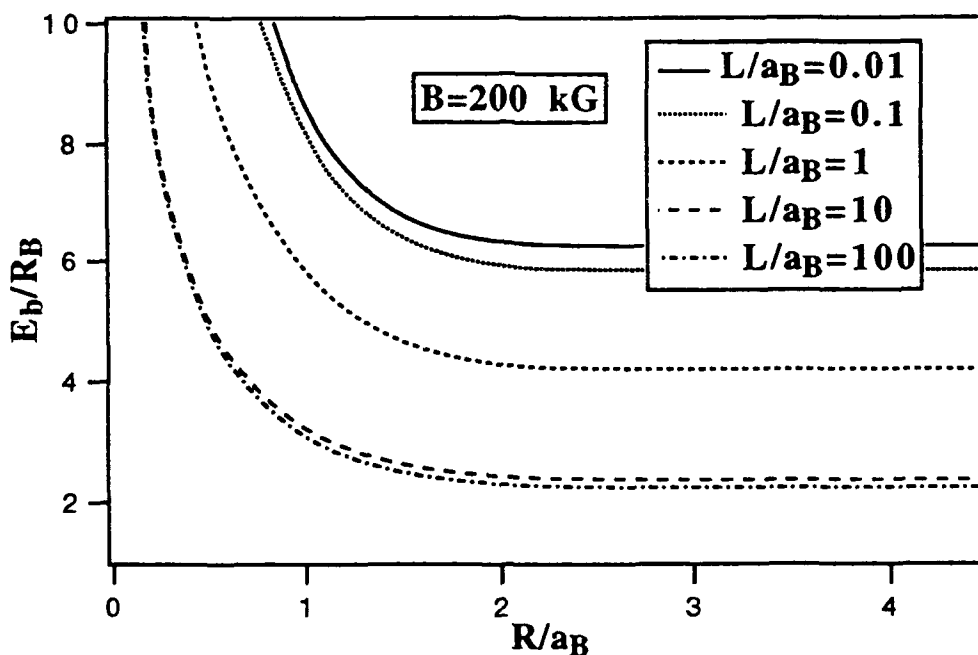


Fig. 14 Variation of the binding energy of a donor ( $E_b$ ), expressed in terms of a hydrogenic Rydberg ( $R_B$ ) in GaAs (5.8 meV) as a function of the radius of the wire ( $R$ ) expressed in terms of the Bohr radius ( $a_B$ ) in GaAs ( $\sim 98 \text{ \AA}$ ) for several values of the disk length ( $L$ ) for  $B=200 \text{ kG}$ .

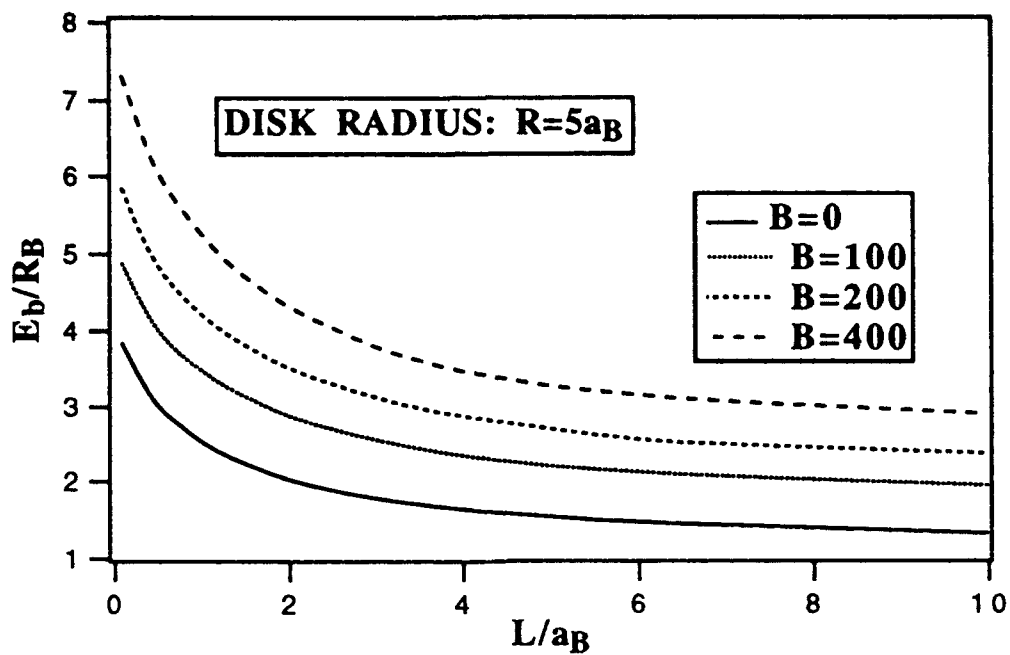


Fig. 15 Variation of the binding energy of a donor ( $E_b$ ), expressed in terms of a hydrogenic Rydberg ( $R_B$ ) in GaAs (5.8 meV) as a function of the disk length ( $L$ ) expressed in terms of the Bohr radius ( $a_B$ ) in GaAs ( $\sim 98 \text{ \AA}$ ) for several values of magnetic field for  $R=5 a_B$ .

## 2.8. A Quantum Statistical Theory Of Excitonic Linewidth Due To Compositional Disorder In Semiconductor Alloys And Quantum Well Structures

The excitonic transitions in unintentionally doped semiconductor alloys are generally broader than those observed in their components. This broadening has been attributed to the presence of compositional disorder in the alloys.

We have developed a very general and a powerful quantum statistical formalism for calculating the excitonic luminescence linewidths and lineshapes in semiconductor alloys due to bandgap fluctuations caused by the random distribution of the alloy components in applied electric and magnetic fields. We use virtual crystal approximation to estimate the local bandgap variations. The shifts of the excitonic transition energy due to the bandgap fluctuations are obtained using first order perturbation theory. We obtain a Gaussian lineshape for the excitonic transition using standard statistical techniques. We apply this formalism to calculate the linewidths and lineshapes associated with the ground-state excitonic transition as a function of alloy composition and magnetic field strength in  $\text{Al}_x\text{Ga}_{1-x}\text{As}$  and  $\text{In}_x\text{Ga}_{1-x}\text{P}$  alloys. The resulting linewidths and lineshapes are in good agreement with the available low-temperature photoluminescence data. A comparison of excitonic linewidths obtained from the present theory with those calculated earlier is also discussed.

We have generalized this formalism to calculate the linewidths of excitonic transitions in semiconductor quantum well structures with arbitrary potential profiles in the presence of applied electric and magnetic fields. We assume that at low temperatures the dominant mechanism responsible for line broadening is the interface roughness which is always present even in the so called "perfect" samples. For instance, in the case of GaAs-AlGaAs quantum well structures, the AlGaAs layers at the interface have a completely random distribution of Al and Ga in the ideal material and will always lead to excitonic line broadening.

In Fig. 16(a) we depict schematically the probability of finding a Wannier exciton around a certain point in a binary alloy. While the bandgap in the alloy fluctuates from one unit cell to another, the excitonic wavefunction extends over many unit cells. The exciton experiences a fluctuating potential due to the difference in bond strengths between alloy components, which is a rapidly varying function of spatial coordinates compared to the exciton wavefunction. Therefore, the excitonic properties are generally obtained using the average material parameters in this region. However, excitons generated in different places of the crystal experience different bandgaps due to the random distributions of the alloy components. A detailed description of the fluctuating potential is clearly very complicated. We therefore estimate this fluctuating potential using a simple description, i.e., the virtual crystal approximation. There is either an atom of component A or B occupying each unit cell with a probability of  $x$  or  $(1-x)$  respectively. The difference in the bond strengths of A and B is the source of the fluctuating potential in the alloy. Fig. 16(b) shows an enlarged section of the fluctuating potential where the alloy component atoms are placed randomly with  $x = 0.3$ .  $E_A$  and  $E_B$  are the bandgaps of A and B components, respectively;  $E_g$  is the average bandgap, and  $\Delta E_g$  is the fluctuating potential.

In Fig. 17, we display the variation of the excitonic linewidth  $\sigma$  in  $\text{In}_{0.48}\text{Ga}_{0.52}\text{P}$  as a function of the applied magnetic field strength. The calculated linewidth (solid line) increases as the applied magnetic field increases. The measured linewidths at 1.4 °K<sup>13</sup> are also shown in Fig 17. as circles. The dashed curve with squares is obtained using the theory of Mena et al.<sup>14</sup>. The dashed curve with triangles is obtained using the earlier theory of Lee and Bajaj<sup>15</sup>. Because this method does not take into account the effect of the closely-spaced fluctuating potentials, it underestimates the excitonic linewidths at high alloy composition, i.e.,  $x = 0.48$  in this case. The measured linewidths in  $\text{In}_{0.48}\text{Ga}_{0.52}\text{P}$  are generally about one meV higher than those obtained from the present theory for the magnetic field strength varying from zero to 136 kG, as shown in Fig. 17. This is due to the fact that our calculations consider only one mechanism of excitonic line broadening, namely, the alloy disorder. The observed linewidths have contributions from other broadening mechanisms such as those due to random electric fields of ionized impurity centers and clustering of alloy components.

The zero-field photoluminescence linewidth  $\sigma$  in  $\text{Al}_x\text{Ga}_{1-x}\text{As}$  as a function of Al concentration is shown in Fig. 18. The solid curve is obtained using the present theory. The dashed curve is obtained from Singh and Bajaj<sup>8</sup>. The solid curve with circles is obtained using the method of Lee and Bajaj<sup>15</sup>.

The squares are the experimental points taken from Singh and Bajaj<sup>8</sup>. The values of the linewidth increase as the Al concentration varies from 0 to 0.4. The linewidths based on the present theory are considerably larger and closer to the experimental values than the previous results. The method of Lee and Bajaj<sup>15</sup>, which does not have any adjustable parameters, produces a linewidth about half of that of the present theory. This indicates that the effect of the closely-spaced fluctuating potential which is taken into account in the present theory is rather important.

In Fig. 19, we show the calculated excitonic photoluminescence linewidths as a function of applied magnetic field at a few Al compositions using the present method (solid curves) and those from Mena et al.<sup>13</sup> (dashed curves). Linewidths obtained from both theories increase with the applied magnetic field as the exciton wavefunction is squeezed by the applied magnetic field. Our zero-field values are somewhat higher than those of Mena et al.<sup>13</sup> as shown in Fig. 19. Moreover, the linewidths predicted in by Mena et al increase with the applied magnetic field strength at a considerably faster rate. This is probably due to the use of spherical exciton volume for the magnetoexciton that is not spherically symmetric in a magnetic field. The present method does not suffer from this drawback, and produces a different magnetic field dependent excitonic linewidth.

We have generalized our formalism to calculate the linewidths of excitonic transitions in quantum well structures of arbitrary potential profiles. We assume that, at low temperatures, the dominant mechanism responsible for line broadening is the interface roughness which, as mentioned earlier, is always present even in the structures with so-called "perfect" interfaces. In Fig. 20, we display the variation of the linewidth of the heavy-hole exciton ( $\sigma$ ) as a function of well size in GaAs-Al<sub>0.3</sub>Ga<sub>0.7</sub>As based quantum well structures with three different potential well profiles, namely, rectangular, parabolic, and asymmetric triangular. We find that the value of  $\sigma$  increases as the well width is reduced, in all three different structures. For well sizes larger than about 100 Å, the value of  $\sigma$  is the highest in the triangular wells and lowest in the rectangular wells. However, for well width less than 100 Å, the value of  $\sigma$  falls below those in rectangular or parabolic wells. This is due to the fact that in these narrower asymmetric triangular wells more and more of the excitonic wave function spills over in the barrier regions thus reducing the effect of the interface on the line broadening. It should be pointed out that our values of the excitonic linewidths are the lowest possible in these structures.

We have used this formalism to calculate the excitonic linewidths in quantum well structures with different potential profiles in the presence of electric and magnetic fields. It is well known that the performance of a spatial light modulator depends on the excitonic linewidth and its variation with electric field. We find that for a given well size, the values of the excitonic linewidth increase as a function of both the electric and magnetic fields in a given quantum well structure [Fig. 21]. The results obtained in these calculations are being used to determine the performance parameters such as on-off ratios, extinction co-efficients etc. of spatial light modulators based on different quantum well profiles.

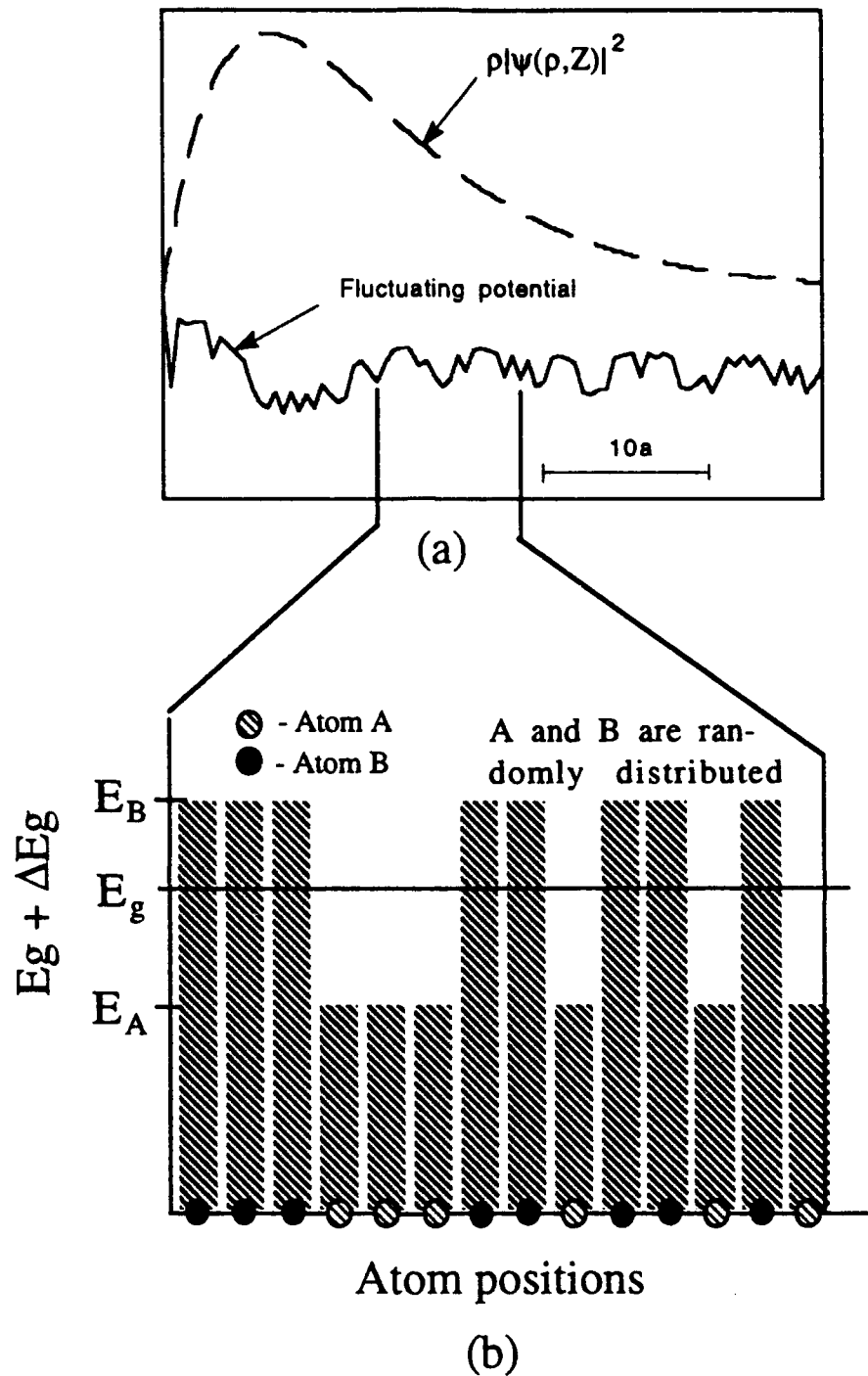


Fig. 16 (a) A sketch of an exciton in the presence of a typical fluctuating bandgap in a binary alloy. The exciton radius is much larger than the lattice constant. (b) An enlarged section of the fluctuating bandgap as a function of atomic positions. The atoms A and B at each lattice site are chosen at random. The probabilities of finding A and B are 0.3 and 0.7, respectively.

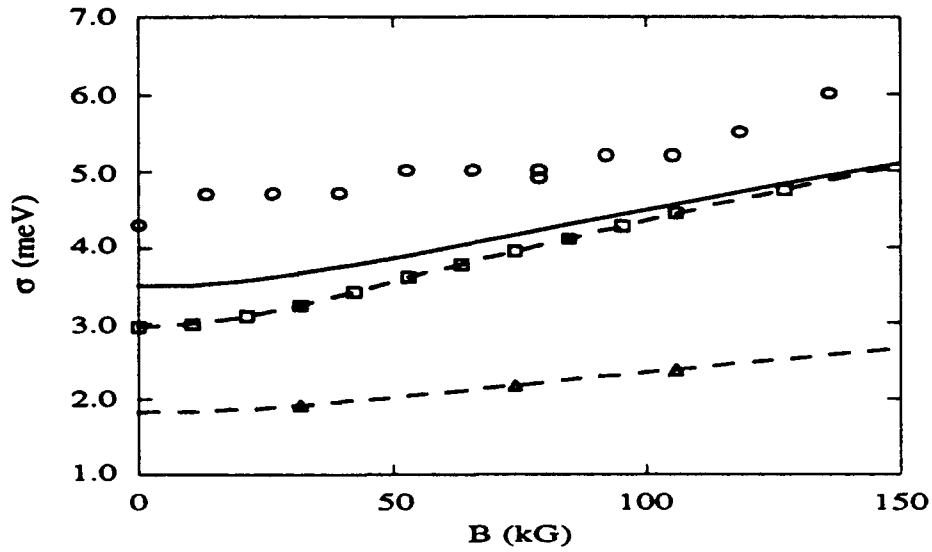


Fig. 17 Variation of the full width at half maximum for the excitonic transition ( $\sigma$ ) in  $\text{In}_{0.48}\text{Ga}_{0.52}\text{P}$  as a function of the magnetic field. Solid curve is obtained from the present theory; circles are experimental data [Jones et al, Phys. Rev. B. 7225 (1992)]; the solid line drawn through the data is a smooth curve to provide a visual aid; dashed curve with squares is obtained using the theory of Mena et al. [J. Appl Phys. 70, 1866 (1991)]; dashed curves with triangles is obtained using the theory of Lee & Bajaj [Appl. Phys. Lett. 60, 853 (1992)].

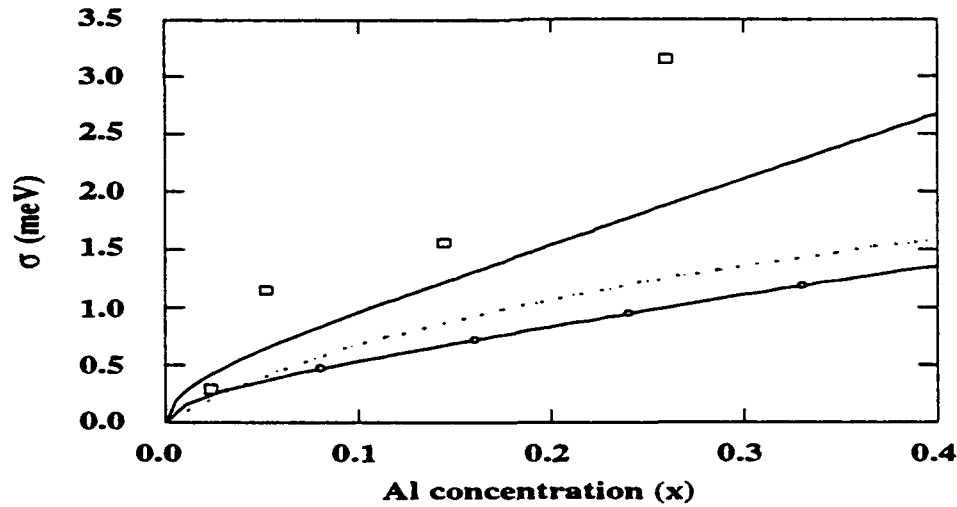


Fig. 18 Variation of the full-width at half-maximum ( $\sigma$ ) of the excitonic transition as a function of Al concentration in  $\text{Al}_x\text{Ga}_{1-x}\text{As}$ : solid line (present result), solid line with circles (Lee & Bajaj), dashed line [Singh & Bajaj]. The experimental points ( $\square$ ) are taken from (Singh & Bajaj [Appl. Phys. Lett. 48, 1077 (1986)]).

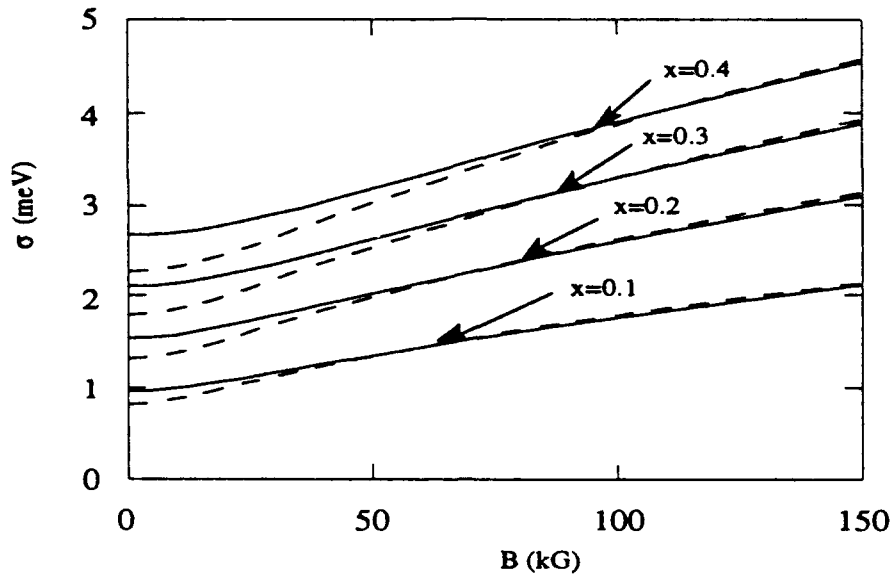


Fig. 19 Variation of the full-width at half-maximum ( $\sigma$ ) of the excitonic transition in  $\text{Al}_x\text{Ga}_{1-x}\text{As}$  as a function magnetic field at a few typical Al compositions: solid curves (present calculation); dashed curves (Mena et al.).

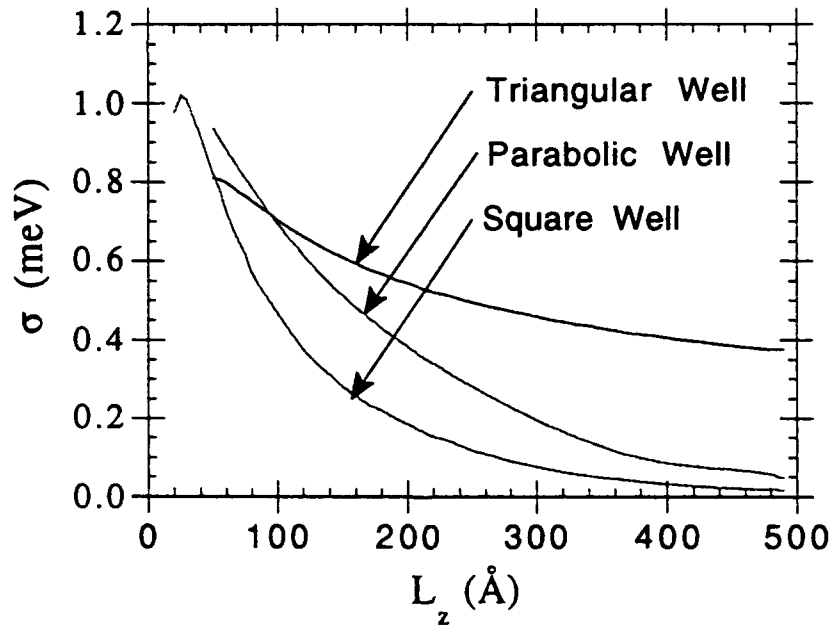


Fig. 20 Variation of the linewidth( $\sigma$ ) of a heavy-hole exciton as a function of well size in a square, parabolic and asymmetric triangular  $\text{GaAs}/\text{Al}_{0.3}\text{Ga}_{0.7}\text{As}$  quantum well structures.



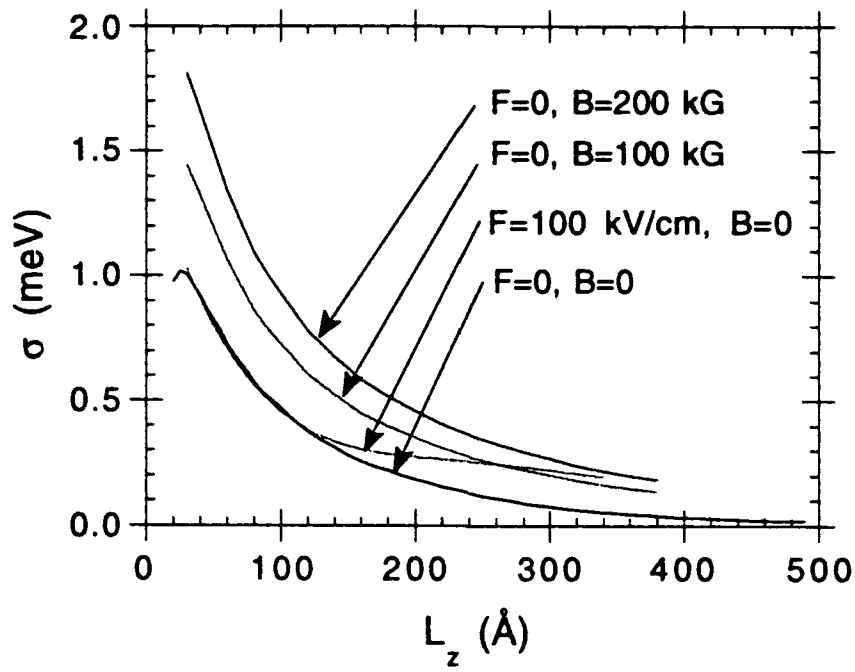


Fig. 21 Variation of the linewidth ( $\sigma$ ) of a heavy-hole exciton as a function of well size in a square, parabolic GaAs-Al<sub>0.3</sub>Ga<sub>0.7</sub>As quantum well for several values of the electric and magnetic fields.

## 2.9. Summary

We have developed a new method for calculating excitonic properties in quantum confined structures in the presence of applied fields. We have reported the results of our calculations of the energy levels of hydrogenic impurities and excitons in coupled double quantum wells, dielectric quantum wells, quantum wires and quantum dots in the presence of electric and magnetic fields. We have also described the results of a new quantum statistical theory of excitonic linewidth in semiconductor alloys and quantum confined structures in the presence of applied electric and magnetic fields.

## 2.10. References

1. S. M. Lee and K. K. Bajaj, to be published.
2. S. M. Lee and K. K. Bajaj, to be published.
3. G. D. Sanders and K. K. Bajaj, J. Appl. Phys. **68**, 5348 (1990).
4. G. E. Bauer and T. Ando, Phys. Rev. B **38**, 6015 (1988).
5. R. L. Greene and K. K. Bajaj, Phys. Rev. B **31**, 6498 (1985).
6. J. Cen and K. K. Bajaj, Phys. Rev. B **46**, 15280 (1992).
7. S. M. Lee and K. K. Bajaj, to be published.
8. D. A. B. Miller, in *Optical Switching in Low-Dimensional Systems*, edited by H. Haug and L. Bányai, pp. 1-8 (Plenum Press, New York, 1988).
9. M. M. Dignam and J. E. Sipe, Phys. Rev. **B43**, 4084 (1991).
10. X. Hong, T. Ishihara, and A. V. Nurmikko, Phys. Rev. **B45**, 6961 (1992).
11. S. Zhang and N. Kobayashi, Appl. Phys. Lett. **60**, 883 (1992).
12. See for example, N. P. Montenegro and S. T. P. Merchancano, Phys. Rev. **B46**, 9780 (1992) and references therein.
13. R. A. Mena, "Magnetic field effect on the exciton photoluminescence linewidth of semiconductor alloys", M. S. Thesis, Arizona State University, 1990, unpublished. R. A. Mena, G. D. Sanders, K. K. Bajaj and S. C. Dudley, J. Appl. Phys. **70**, 1866 (1991).
14. E. D. Jones, R. P. Schneider, S. M. Lee and K. K. Bajaj, Phys. Rev. B **46**, 7225 (1992).
15. S. M. Lee and K. K. Bajaj, Appl. Phys. Lett. **60**, 853 (1992).

### **C. Publications in technical journals.**

J. G. Cody, D. L. Mathine, R. Droopad and G. N. Maracas, "Characteristics of Strained InGaAs/GaAs/AlGaAs Diode Lasers With Asymmetric Triangular Quantum Well Active Regions," to appear in *Photonics Technology Letters*

D.L. Mathine, G.N. Maracas, D.S. Gerber, R. Droopad, R.J. Graham, M.R. McCartney and D.J. Smith, "Characterization of an AlGaAs/GaAs Asymmetric Triangular Quantum Well Grown By a Digital Alloy Approximation," submitted to *J. Appl. Phys.*

D.L. Mathine, S. Krishnan and G.N. Maracas, "Spectral Solution of Schrödinger's equation," submitted to *Phys. Rev. B*

D.S. Gerber and G.N. Maracas, "A Simple Method for Extraction of Multiple Quantum Well Absorption Coefficient from Reflectance and Transmittance Measurements," to appear in *J. Quantum Electronics* 1993

D.S. Gerber, R. Droopad and G.N. Maracas, "Comparison of Electroabsorption in Asymmetric Triangular and Rectangular GaAs/AlGaAs Multiple Quantum Wells," *Appl. Phys. Lett.* 62(5) p. 525-527 (1993)

R. Droopad, D.S. Gerber, C. Choi and G.N. Maracas, "Pseudomorphic InGaAs/GaAs and GaAs/AlGaAs Asymmetric Triangular Quantum Wells Grown by MBE for Optoelectronic Device Applications," *J. Crystal Growth*, 127, p. 606-610 (1993)

D. S. Gerber, R. Droopad and G. N. Maracas, "A GaAs/AlGaAs Asymmetric Fabry-Perot Reflection Modulator with Very High Contrast Ratio," *Photonics Technology Letters*, 5(1), p. 55-58 (1993)

G. N. Maracas, J. L. Edwards, D. S. Gerber, R. Droopad, "In Situ Spectroscopic Ellipsometry in Molecular Beam Epitaxy for Photonic Devices" *Applied Surface Science* 63, pp. 1-8 1993 (invited paper)

C. Park, K.T. Shiralagi, R. Droopad and G. N. Maracas, "A Novel Bistable MQW Electro-optic Phase Modulator," *Photonics Technology Letters*, 4 (11), p. 1225-1227 (1992)

R Droopad, R A Puechner, K Y Choi, K T Shiralagi and G N Maracas, "Molecular Beam Epitaxial Growth and Optical Properties of Strained Rectangular and Asymmetric Triangular InGaAs Quantum Well Structures," *J. Crystal Growth*. 114 (1991) 327.

R.A. Puechner, D.S. Gerber, R. Droopad, and G.N. Maracas, "Nonlinear Electroabsorption in Asymmetric Triangular Quantum Well Self Electro-Optic Effect Devices," *Internat. J. Nonlinear Optical Phys.*, Vol. 1, No. 3, July (1992) (invited paper).

K. T. Shiralagi, R. A. Puechner, K. Y. Choi, R. Droopad, and G. N. Maracas, "Narrow Photoluminescence Linewidth of Quantum Wells Grown by Gas Source Molecular Beam Epitaxy," *J. Cryst. Growth*, 114 (1991) 337.

R. Droopad, K. Y. Choi, R. A. Puechner, K. T. Shiralagi, D. S. Gerber, G. N. Maracas, "Optical Properties of Strained Asymmetric Triangular InGaAs/GaAs Multiple Quantum Wells," *Applied Physics Letters*, 59 (1991) 2308.

R. Droopad, R. A. Puechner, K. T. Shiralagi, K. Y. Choi, G. N. Maracas, "Optical Properties of a Single Strained InGaAs/GaAs Quantum Well on Vicinal GaAs Surfaces," *Appl. Phys. Lett.*, 58 (1991) 1777.

G. D. Sanders and K. K. Bajaj, "Absorptive Electro-Optic Spatial Light Modulators with Different Quantum Well Profiles," *J. Appl. Phys.* 68, 5348 (1990).

P. W. Yu, D. C. Reynolds, G. D. Sanders, K. K. Bajaj, C. E. Stutz and K. R. Evans, "Electric Field Effect of Excitons in Asymmetric Triangles AlGaAs/GaAs Quantum Wells." *Phys. Rev. B* 43, 4344 (1991).

S. M. Lee and K. K. Bajaj, "A New Theory of Linewidths of Radiative Transitions due to Disorder in Semiconductor Alloys." *Appl. Phys. Lett* 60, 853 (1992).

E. D. Jones, R. P. Schneider, S. M. Lee and K. K. Bajaj, "Magnetic Field Dependent Excitonic Photoluminescence Linewidth in Semiconductor Alloys." *Phys. Rev. B* 46, 7225 (1992).

S. V. Branis, Gang Li and K. K. Bajaj, "Hydrogenic Impurities in Quantum Wires in the Presence of Magnetic Field." *Phys. Rev. B* 47, 1316 (1993).

S. M. Lee and K. K. Bajaj, "A Quantum Statistical Theory of Linewidth of Radiative Transitions Due to Compositional Disorder in Semiconductor Alloys." J. Appl. Phys.. (in press).

J. Cen, S. M. Lee and K. K. Bajaj, "Effect of Electric and Magnetic Fields on Confined Donor States in a Coupled Double Quantum Well." J. Appl. Phys. (in press).

S. V. Branis, Gang Li and K. K. Bajaj, "Exciton Binding Energy in a Quantum Wire in the Presence of a Magnetic Field." Phys. Rev. B (in press).

S. V. Branis, Gang Li and K. K. Bajaj, "Off-center Hydrogenic Impurities in Quantum Wires in the Presence of a Magnetic Field." Submitted for publication in Phys. Rev. B.

S. V. Branis, Gang Li and K. K. Bajaj, "Hydrogenic Donor States in Quantum Disks in the Presence of a Magnetic Field." Submitted for publication in Phys. Rev. B.

J. Cen and K. K. Bajaj, "Confined Donor States in Cross Electric and Magnetic Fields in a Coupled Double Quantum Well." Submitted for publication in Phys. Rev. B.

J. Cen and K. K. Bajaj, "Effect of Electric and Magnetic Fields on Confined Donor States in a Dielectric Quantum Well." Submitted for publication in Phys. Rev. B.

J. Cen and K. K. Bajaj, "Exciton Binding Energies in a Dielectric Quantum Well in a Magnetic Field." Submitted for publication in Phys. Rev. B.

S. M. Lee and K. K. Bajaj, "Simple Method For Calculating Excitonic Properties in Quantum-Confined Semiconductor Structures with Arbitrary Potential Profiles in the Presence of Applied Fields." To be submitted for publication in the J. Appl. Phys.

S. M. Lee and K. K. Bajaj, "A Simple Method For Calculating the Excitonic Properties of Semiconductor Quantum Wells of Arbitrary Shapes in the Presence of Both Electric and Magnetic Fields." To be submitted for publication in the J. Appl. Phys.

G. D. Sanders, G. N. Maracas and K. K. Bajaj, "A Numerical Model of the Quantum Well Waveguide Spatial Light Modulator." To be submitted for publication in the J. Appl. Phys.

S. M. Lee and K. K. Bajaj, "A Quantum Statistical Theory of Excitonic Linewidth in Quantum Well Structures With Arbitrary Potential Profile in the Presence of Applied Fields." To be submitted for publication in Phys. Rev. Letters.

#### **D. Professional personnel associated with the research effort**

##### **At Arizona State University**

G. N. Maracas, principal investigator  
 K. Choi, Assistant Research Scientist  
 D. Gerber, PhD 8/92  
 S. Krishnan, MS 8/92  
 C. Wheeler, PhD 5/94 (est)  
 R. Puechner, Graduate Student

R. Droopad, Assistant Research Scientist  
 D. L. Mathine, Faculty Associate  
 K. Shiralagi, PhD 6/92  
 C.D. Park, PhD 12/92  
 J. Cody, MS 12/93 (est)  
 A. Tessmer, Graduate Student

Gary Sanders, Faculty Associate ( 1/15/90 - 8/15/90 )  
 Xi Zhang, MS 5/91 - (Bajaj)

##### **At Emory University**

K. K. Bajaj, principle investigator  
 S. M. Lee, post-doctoral fellow  
 J. Cen, post-doctoral fellow  
 G. Li, post-doctoral fellow  
 A. Antonelli, post-doctoral fellow

#### **E. Interactions:**

Telephone conversations with AFSOR staff have been on a regular basis to discuss technical and contractual issues and developments. The URI review visit was April 26, 1991 at ASU. Publications and viewgraphs of research progress were sent to AFOSR as they became available.

Collaborations on this project have been with MOTOROLA PCRL, on vertical cavity surface emitting lasers, the Center for High Resolution Microscopy (HREM) (ASU) on analysis of nanoscale

composition, Brooklyn College on electromodulation spectroscopy of ATQWs. Three visits to AFOSR to present progress were also made.

Have collaborated with scientists at Solid State Electronic Directorate, Wright Laboratory, Wright Patterson AFB and have discussed with them our technical progress both by telephone and by a personal visit. Have had regular telephone conversations with program managers at AFOSR concerning our technical progress and contractual issues. Have mailed them preprints and reprints of our work on a regular basis. Have collaborated with scientists at Sandia Laboratories, Albuquerque.

### **E.1. Papers presented at meetings, conferences, seminars, etc.**

J. G. Cody, D. L. Mathine, R. Droopad, G. N. Maracas, R. Rajesh, and R. W. Carpenter, "Applications of the Digital Alloy Composition Grading Technique to Strained InGaAs/GaAs/AlGaAs Diode Lasers Active Regions," North American MBE Conference, Stanford, CA (September 1993)

H. Qiang, Y-S Huang, F. Pollak, W.S. Chi, D.L. Mathine and G.N. Maracas, "Electromodulation Spectroscopy of a GaAs/GaAlAs Asymmetric Triangular Quantum Well Structure," Modulated Semiconductor Structures Conference, August 1993

D.S. Gerber, R. Droopad and G.N. Maracas, "Electroabsorptive asymmetric Fabry-Perot modulators with symmetric coupled QWs," Optical Society of America Topical Meeting on Spatial Light Modulators and Applications, Palm Springs, CA (March 1993)

G.N. Maracas and D.S. Gerber, "High On/Off Ratio Asymmetric Fabry Perot Reflection Modulators," WOCSEMMAD, Santa Monica, CA February 1993

G. N. Maracas, J. L. Edwards, D. S. Gerber, R. Droopad, "In Situ Spectroscopic Ellipsometry in Molecular Beam Epitaxy for Photonic Devices" E-MRS 1992 Spring Mtg, Strasbourg, France, June 1992 (invited paper)

R.A. Puechner, D.S. Gerber, D.A. Johnson, R. Droopad and G.N. Maracas, "Optical Properties of Asymmetric Triangular Quantum Wells for Self Electro-optic Effect Devices" International Conf. on Nonlinear Optics, Hawaii, 1990.

Gang Li, S. V. Branis and K. K. Bajaj, "Effect of Magnetic Field on Hydrogenic Impurities in Quantum Disks." To be Presented at the 1993 March Meeting of the American Physical Society, Seattle Washington.

Gang Li, S. V. Branis and K. K. Bajaj, "Effect of Magnetic Field on the Off-center Hydrogenic Impurities in Quantum Wires." To be Presented at the 1993 March Meeting of the American Physical Society, Seattle Washington.

J. Cen and K. K. Bajaj, "Donor Binding Energies in a Dielectric Quantum Well Structures in an Electric Field and Magnetic Fields." To be Presented at the 1993 March Meeting of the American Physical Society, Seattle Washington.

J. Cen and K. K. Bajaj, "Exciton Binding Energies in Dielectric Quantum Well Structures in an Electric Field." To be Presented at the 1993 March Meeting of the American Physical Society, Seattle Washington.

S. V. Branis, Gang Li and K. K. Bajaj, "Effect of Magnetic Field on Exciton Binding Energies in Quantum Well Wires." Presented at the 1992 March Meeting of the American Physical Society, Indianapolis, Ind. Bull. Am. Phys. Soc. 37, 708 (1992).

Gang Li, S. V. Branis and K. K. Bajaj, "Effect of Magnetic Field on Hydrogenic Impurities in Quantum Well Wires." Presented at the 1992 March Meeting of the American Physical Society, Indianapolis, Ind. Bull. Am. Phys. Soc. 37, 324 (1992).

S. M. Lee and K. K. Bajaj, "A Quantum Mechanical Theory of linewidths of Radiative Transitions due to Disorder in Semiconductor Alloys in the Presence of an Applied Magnetic Field." Presented at the 1992 March Meeting of the American Physical Society, Indianapolis, Ind. Bull. Am. Phys. Soc. 37, 293 (1992).

J. Cen, and K. K. Bajaj, "Effects of Electric and Magnetic Fields on Confined Donor States in a Coupled Double Quantum Well." Presented at the 1992 March Meeting of the American Physical Society, Indianapolis, Ind. Bull. Am. Phys. Soc. 37, 270 (1992).

K. K. Bajaj, "Quantum Well Based Spatial Light Modulators: Effects of Potential Profile On Their Performance." Presented at the Workshop on Optical Properties of Mesoscopic Semiconductor Structures, April 1991, Snowbird, Utah.

**E.2. Consultative and advisory functions to other laboratories and agencies**

**F. New discoveries, inventions, or patent disclosures and specific applications stemming from the research effort.**

**G. Other statements.**